PB85-245843

A mining research contract report
March 1984

RESPIRABLE DUST MEASUREMENT

Contract J0113042
Particle Technology Laboratory
University of Minnesota

BUREAU OF MINES
UNITED STATES DEPARTMENT
OF THE INTERIOR

REPRODUCED BY
U.S. DEPARTMENT OF COMMERCE
NATIONAL TECHNICAL
INFORMATION SERVICE
SPRINGFIELD, VA 22161

50272-101

REPORT DOCUMENTATION PAGE

1. REPORT NO. BuMines OFR 92-85

2.

3. Recipient's Accession No. PB85 245843 /AS

4. Title and Subtitle

Respirable Dust Measurement

5. Report Date Mar. 1984

6.

7. Author(s)

Virgil A. Marple and Kenneth L. Rubow

8. Performing Organization Rept. No.

9. Performing Organization Name and Address

University of Minnesota
Particle Technology Laboratory
142 Mechanical Engineering
111 Church St. SE
Minneapolis, MN 55455-0111

10. Project/Task/Work Unit No.

11. Contract(C) or Grant(G) No.

(C) J0113042

(G)

12. Sponsoring Organization Name and Address

Office of Assistant Director--Mining Research
Bureau of Mines
U.S. Department of the Interior
Washington, DC 20241

13. Type of Report & Period Covered

Contract research, 6-26-81--11-26-83

14.

15. Supplementary Notes

Approved for release June 14, 1985.

16. Abstract (Limit: 200 words)

The objective of this contract was to conduct characterization, evaluation, and/or calibration studies of instrumentation used for measuring the quantity of respirable dust in mining atmospheres. Initially, this work involved the upgrading and detailed evaluation of the aerosol test chamber and the development of impactors with respirable classification characteristics. These were used as standards in the chamber for measuring the quantity of respirable dust based on either the American Conference of Governmental Industrial Hygienist or British Medical Research Council respirable dust criteria. A program was then conducted to calibrate several photometers. In addition, the mass sensitivity of the GCA RAM-1 photometer to water droplets in the respirable size range was determined. Three additional studies were also made in this program: (1) An experimental study was performed to ascertain the effect of crosswind, cyclone orientation, and particle size on particle sampling and penetration through the 10-mm Dorr-Oliver cyclone. (2) A theoretical study was conducted to refine the theory used to predict the particle collection characteristics of impactors. (3) Filter samples with known quantities of diesel and coal particles were produced and delivered to the Bureau of Mines for testing a Raman scattering analysis technique to discriminate diesel particles in the presence of coal dust.

17. Document Analysis a. Descriptors

Mining research
  Dust
  Particle
  Instrumentation
  Coal

b. Identifiers/Open-Ended Terms

Respirable mine dust measurement

c. COSATI Field/Group 08/I

18. Availability Statement

Release unlimited by NTIS.

19. Security Class (This Report) Unclassified

20. Security Class (This Page) Unclassified

21. No. of Pages 154

22. Price

(See ANSI-Z39.18) See Instructions on Reverse

OPTIONAL FORM 272 (4-77)
(Formerly NTIS-35)
Department of Commerce

Preceding page blank

FOREWORD

This report was prepared by the University of Minnesota, Department of Mechanical Engineering, Minneapolis, Minnesota, under U. S. Bureau of Mines Contract No. J0113042. The contract was initiated under the Coal Mine Health and Safety Program. It was administered under the technical direction of Pittsburgh Research Center with Mr. Kenneth L. Williams acting as the Technical Project Officer. Ms. Sylvia Brown was the Contract Administrator for the Bureau of Mines.

This report is a summary of the work recently completed as part of this contract during the period June 26, 1981 to November 26, 1983. This report was submitted by the authors in March, 1984.

Reference to specific brands, equipment, or trade names in this report is to facilitate understanding and does not imply endorsement by the Bureau of Mines.

This report contains no patentable features.

TABLE OF CONTENTS

Page No.

LIST OF TABLES

APPENDIX A

LIST OF FIGURES

Page No.

Page No.

Appendix A

Appendix B

Page No.

CHAPTER 1
EXECUTIVE SUMMARY

1.1 Background

The mining industry has long been concerned about the quantity of respirable dust to which miners are exposed because of the potential hazard this dust poses to the miner's respiratory system. Because of this concern, many studies dealing with dust in coal mines have been conducted and samples are taken on a regular basis in the mines to monitor the quantity of dust in the respirable size range. To make such measurements, it is first necessary to have the proper instrumentation. This instrumentation has a special requirement: It must be safe to operate in the explosive atmosphere that may exist in a coal mine. Therefore, only a few specialized instruments have been developed for measuring the particle concentration within mines and much work has gone into technique development of using the instruments as well as the calibration of the instruments so that their data will be as useful as possible.

1.2 Purpose and Scope of the Contract

The purpose of this contract was to conduct instrument research and calibration so that the instruments which do exist for measuring the quantity of respirable dust in a mining atmosphere will be as useful as possible. The contract is divided into tasks which are described in the various chapters of this final report as follows:

Chapter 2 - The upgrading and evaluation of the aerosol test chamber which is used in many of our dust research programs.
Chapter 3 - The development of impactors with respirable classification characteristics to be used as reference measurement standards in the chamber for either the ACGIH or the BMRC respirable criteria.
Chapter 4 - The evaluation and calibration of photometers.
Chapter 5 - The evaluation of the 10mm Dorr-Oliver cyclone sampling in crosswind conditions.
Chapter 6 - A theoretical study of impactors and the ability of the theory to predict their collection characteristics for large particles.
Chapter 7 - The preparation of filter samples with known quantities of diesel exhaust particulate and coal dust.

1.3 Results

The type of results that were obtained under this contract are quite varied depending on the task being performed. In some cases the results were the development of test equipment such as the aerosol test chamber and respirable classifiers. In other cases the results were the evaluation of currently used instrumentation such as the photometers and the 10mm cyclone. Yet in other cases the results were a better understanding of basic instruments such as the impactors and photometers. Finally, some of the results were service in nature such as the preparation of the diesel/coal samples. The highlights of the results of the various chapters are given in the following paragraphs.

Chapter 2 describes improvements and the evaluation of the aerosol test chamber. The improvements were primarily in the form of mechanizing the rotation of the table at the base of the chamber so that no instrument has a preferred location during a sampling episode. In the rotating table mode of operation, the table rotates 360° in one direction, stops, and rotates 360° back. It continues this motion until the sampling period has finished. For some tests, however, the table cannot be rotated and the spatial uniformity of the aerosol must be as even as possible to obtain good test results. An extensive study was made of the spatial uniformity of the aerosol within the chamber; both with the table stationary and rotating. Finally, an evaluation of the temporal stability of the aerosol in the chamber was made. The temporal stability was good if the aerosol generator supplying dust to the chamber was stable.

The work described in Chapter 3 is the development of samplers to serve as standards in measuring the particle size distribution and the quantity of respirable dust in the chamber. The samplers consisted of a cascade impactor to obtain the mass size distribution of the dust particles and impactors with respirable size penetration characteristics so that the quantity of the respirable dust in the chamber could be measured. These respirable impactors were designed to perform according to both the ACGIH and the BMRC respirable criteria.

Chapter 4 describes the evaluation of a large number of commercial photometers. These photometers included those that were designed to be safe in gaseous mines as well as photometers designed for general use. Calibration curves were derived for all of the photometers which were tested. Evaluations were performed on 8 photometer models from 5 manufacturers. The test aerosols consisted of five different coal dusts with mass median diameters ranging from 2.0 to 14.0 μm and two Arizona road dust aerosols with mass median diameters of 1.6 and 3.8 μm. The respirable mass concentration of the test aerosol was varied from 0.15 to 18 mg/m^3 with the respirable fraction of the aerosols ranging from 0.93 to 0.016. Test results show that the response of photometers are linearly proportional to the respirable mass concentration, but a calibration should be performed on each photometer to obtain the proportionality constant as this constant ranged from 0.66 to 1.28. The proportionality contant was greater for Arizona road dust than for coal dust and decreased with increasing particle size. The GCA MINIRAM and ppm HAM photometers primarily respond to the respirable fraction of the test aerosol independent of the nonrespirable amount even through no inertial preseparator are used. Data were obtained to determine the effect of the GCA RAM-1 operating flow rate and active versus passive sampling with the GCA MINIRAM on the response of these instruments. Lastly, a study was performed to determine the sensitivity of the GCA RAM-1 to water droplets.

In Chapter 5, calibration curves for the 10 mm Dorr-Oliver cyclone sampling in crosswinds from 1.0 to 9.0 m/s are presented. The quantity of respirable dust sampled by the cyclone was found to be strongly dependent upon particle size and orientation of the inlet of the cyclone to the direction of the wind. The variation in the quantity of particles collected downstream of the cyclone for various inlet orientations was found to increase from about 5 to 70% with wind velocities increasing from 2 to 9 m/sec. This dependency could be reduced to less than 10% by providing a shield around the inlet region of the cyclone.

Chapter 6 describes a theoretical study of the impaction characteristics of inertial impactors. This study is unique in that special precautions were taken to include the correct drag coefficients for the particles as a function of their Reynolds number and also to include the effects of gravity. The gravity effects became important for the larger particles where the theory and experiments in the past have not agreed. A large number of impactor collection efficiency curves is presented for various conditions.

In Chapter 7, a method was devised for mixing coal dust and diesel exhaust particulate simultaneously and collecting them upon a filter in known quantities. A number of samples were prepared where the ratios of diesel particulate to coal dust was varied.

1.4 Recommendations for Future Work

Over the course of this contract, and previous contracts, we have calibrated and evaluated most of the commercial instruments which can be used for monitoring the dust in coal mines. This type of work should be performed periodically as new instruments become available and old instruments revised. This type of evaluation should be performed with the techniques that have been developed in this contract.

Another area that needs further work is the study of the cyclone sampling in crosswind. As shown in this report, the quantity of respirable dust measured is a strong function of the orientation of the cyclone when sampling in a crosswind. This phenomena should be studied further; both theoretically and experimentally. Theoretical techniques are available by which the Navier-Stokes equations which govern the flow fields, can be solved in three dimensions using finite difference techniques with iterative relaxation procedures to solve for the flow fields. The particles can then be put in a flow field and the sampling efficiency determined theoretically. In addition, it has been shown expermentally in this contract that the effects of the wind on sampling efficiency can be reduced by positioning a shield around the inlet. However, no work was performed concerning optimizing the size, shape, or position of the shield. If a shield were to be used, this optimization work should be done before selecting a shield.

CHAPTER 2

UPGRADING AND EVALUATION OF TEST CHAMBER

2.1 Introduction

Since the time the aerosol test chamber was built in our laboratory, a second aerosol test chamber was constructed for NIOSH and several improvements were included in the second chamber. Thus, before performing the photometer evaluations, the improvements were incorporated into the chamber in our laboratory. In addition, an evaluation of the spatial and temporal aerosol uniformity within the test section of the chamber was performed.

2.2 Chamber Improvements

The chamber, as is it now constructed, is shown schematically in Figure 2.1 and discussed by Marple and Rubow (1,2). The main improvements were the installation of a new turntable drive mechanism and a new system for mounting the air lines and electrical leads to the turntable. In the older version the electrical leads and air lines entered the test chamber through a hollow turntable shaft. This feature made it difficult to motorize the turntable and, thus, in the revised version the leads enter the chamber through the lower support plate and are attached to the outer rim of the turntable. Besides making it easier to connect a drive mechanism to the table, this approach has the additional advantage of distributing the electrical leads and air lines around the periphery of the table and freeing the center of the table for instrumentation. In essence, the modification provides more useable instrumentation space on the table.

The table is powered by a reversible-variable-speed gearmotor located external to the chamber to prevent creating a heat source within the chamber which may cause convective currents. The drive mechanism from the motor shaft to the turntable shaft is a roller chain with chain tensioning devices so that the table may be rotated in either direction. This arrangement allows the table to rotate from 0.25 to 2 rpm. Since it is not possible to rotate the table more than 360° without tangling the air lines and electrical leads, a switch inside the chamber senses the position of the table and reverses the table direction after it rotates 360°. Thus, the table oscillates, turning no more than 360° in either direction.

2.3 Evaluation of Spatial Aerosol Uniformity

Not only was the chamber upgraded with the new rotating table but a program was undertaken to make the aerosol concentration as uniform as possible throughout the chamber. The uniformity tests were performed by placing 37 mm open-faced plastic filter samplers 40 cm above the turntable in the chamber at the five locations indicated in Figure 2.2. Each filter was upward facing. Monodisperse aerosol particles of liquid oleic acid containing a uranine dye tracer were generated by a TSI Model 3050 vibrating orifice monodisperse aerosol generator (VOMA) (TSI, Inc, St. Paul, MN) and introduced into the upper portion of the chamber. For each run, aerosol from the VOMA was continuously injected into the top of the chamber, drawn down through the central test section, and captured in absolute filters at the lower portion of the chamber. Since there

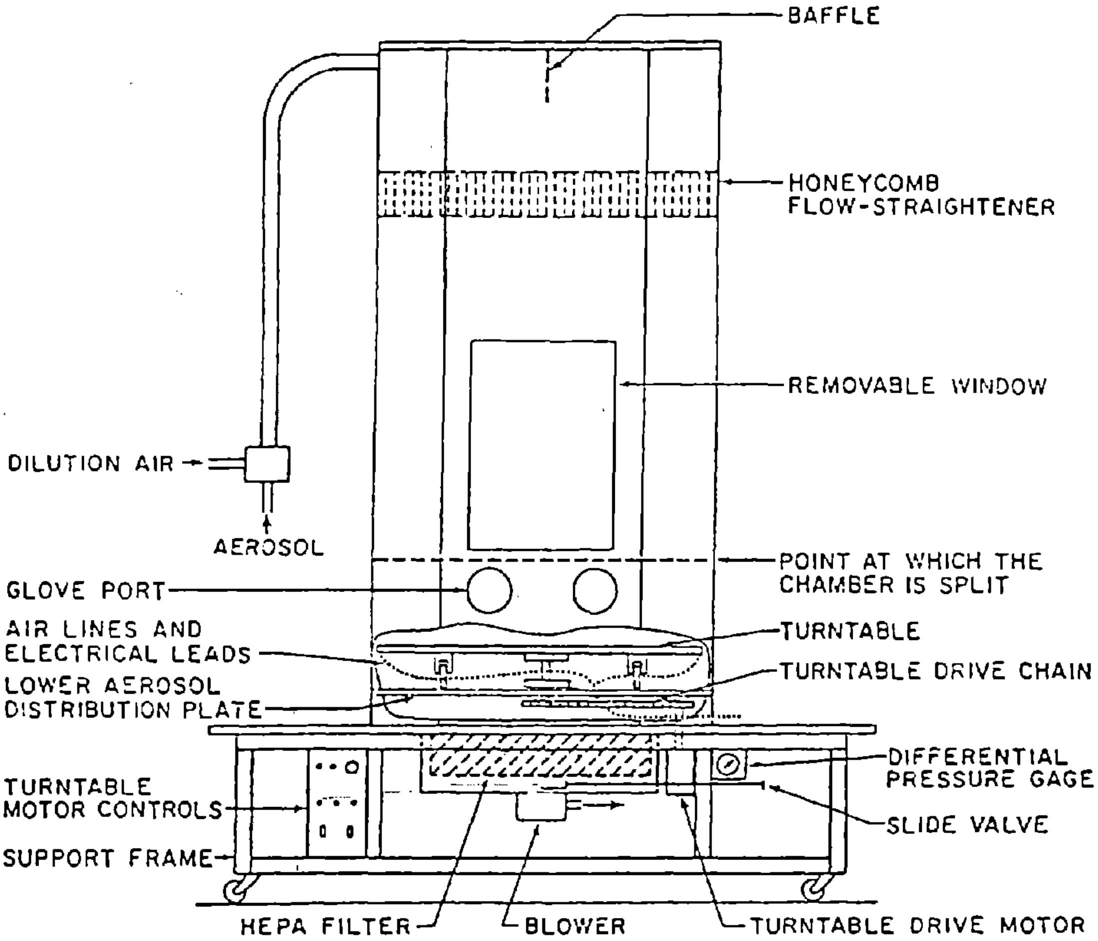

Figure 2.1. Schematic diagram of aerosol test chamber.

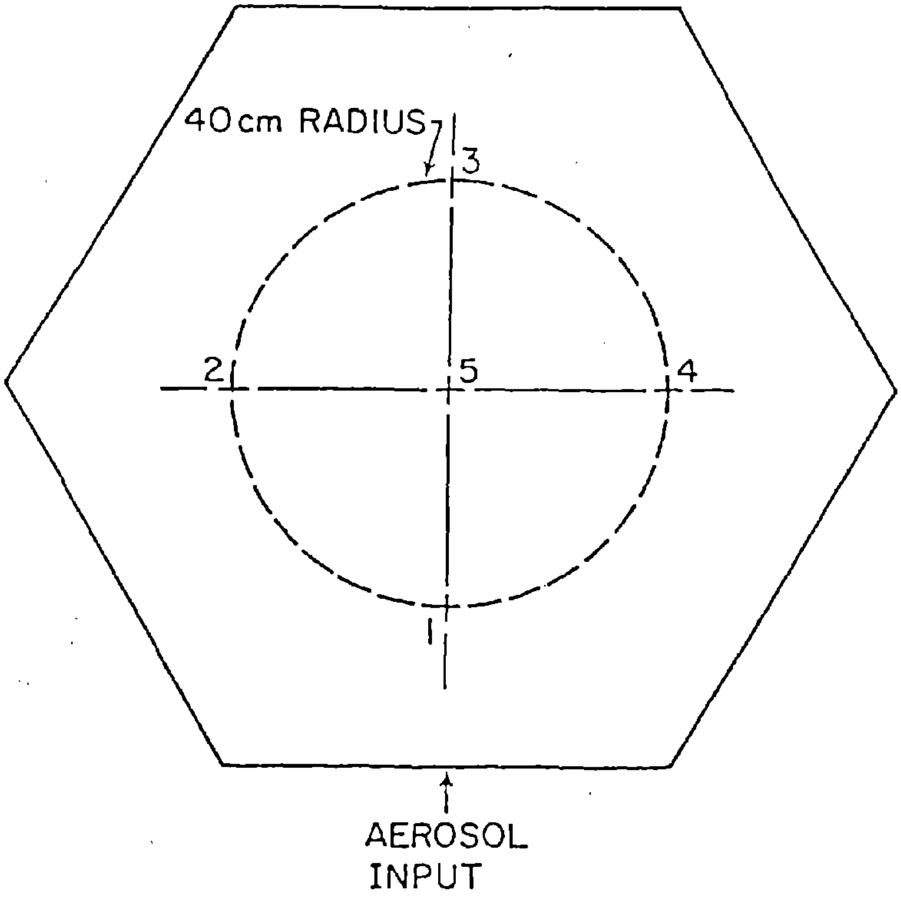

Figure 2.2. Schematic diagram of sampler location within aerosol test chamber.

Table 2.1

Aerosol concentration as a Function of Location for Unmodified Chamber

D_p, um	Relative aerosol concentration at location				
	1	2	3	4	5
2.5	0.98	1.00	0.99	0.97	0.98
15	0.83	0.93	1.00	0.95	0.94

is little crossflow in the chamber, the samplers were essentially exposed to a quiescent environment. The length of each run ranged from 10 to 30 minutes after which the filters were washed in 50 ml of 0.001 N aqueous solution of NaOH. The amount of flourescent material in the wash was then determined by use of a fluorometer. Since the concentration of uranine dye was proportional to the quantity of particles collected on the filters, the aerosol concentration as a function of location could be determined. The uncertainty in the concentration measurement determined through multiple measurements was ±3%.

In the first series of tests with the unmodified chamber, the uniformity of 2.5 and 15 μm aerodynamic diameter particles was determined with the air flow rate through the chamber at 200 L/min. The data from these runs are shown in Table 2.1 as a function of concentration, relative to the average concentration, at the various positions indicated in Figure 2.2. These tests showed that there were higher concentrations of particles directly opposite the inlet than at the other locations. Furthermore, the concentration gradient was particle size dependent. Concentration differences for the 2.5 μm particles were on the order of the measurement uncertainty of 3% but the maximum concentration difference for the 15 μm particles was 17%.

With this uneven concentration being noted, an experimental program was undertaken to determine the type of baffling required in the upper portion of the chamber above the honeycomb flow straighteners to obtain a uniform distribution. Fluid flow visualization studies were first conducted to qualitatively determine the fluid flow patterns in the region above the honeycomb. The technique involved generating a dense aerosol cloud of 0.3 μm oil droplets. This aerosol was passed through a 0.6 cm diameter tube to various regions above the honeycomb. A plexiglass window was installed in the chamber top so that the oil aerosol could be observed when illuminated from below. Tests were conducted with the unbaffled chamber as well as with several baffling systems. These tests showed that the input aerosol jet in the unbaffled chamber impinged on the opposite wall of the chamber resulting in a high concentration of particles being present opposite the aerosol input as indicated in Table 2.1. The flow visualization studies showed a more uniform mixing of the aerosol jet with the air in the upper chamber when baffles were used.

An experimental study was conducted to determine required size, location, and configuration of the baffling to obtain spatial uniformity of the particles. The baffle configurations tested can be divided into two classes. The first class consisted of single deflectors suspended into the aerosol jet from the top of the chamber which were intended to prevent the jet from impinging on the opposite wall by deflecting the aerosol flow to the sides of the chamber. The second class consisted of attaching ledges to the chamber wall opposite the inlet at a location just below the point where the aerosol jet impinged. The intent here was to deflect more of the flow back toward the inlet region of the chamber.

The important parameters of size and placement of the deflectors in the chamber are given in Table 2.2. The designs listed are only representative of a wide variety of evaluated designs. Other designs tested included a wedge shaped deflector, which was positioned approximately 10 cm from the exit of the aerosol inlet pipe and flat obstructions of oval, rectangular and circular shapes which were positioned normal to the direction of the aerosol flow at the center of the

Table 2.2

Upper Chamber Baffling: Type of Baffle

And Resulting Range in Aerosol Concentration

Deflector[1]		Range in Aerosol Concentration[3] Relative to Mean Concentration %
Outside Diameter, cm	Hole Diameter, cm	
7.6	0	12
15.2	0	16
15.2	2.5	7
15.2	3.8	6
Ledge[2]		
Width, cm	Distance Above Honeycomb, cm	
12.7	7.6	6
10.2	7.6	16
6.4	12.7	13

[1] Deflector - Located 58 cm from exit of aerosol input tube
- Oriented normal to direction of input aerosol flow
- Positioned with center of deflector on axis with exit of aerosol input tube.

[2] Ledge attached to wall opposite aerosol input and oriented parallel to honeycomb

[3] For 15 μm diameter aerosols

chamber as shown in Figure 2.3. The size of the deflectors varied from 7.6 to 15.2 cm while the diameters of the concentric holes varied from 0 to 3.8 cm. The ledges were of various widths and were positioned parallel to the top of the honeycomb at various distances above the honeycomb.

The results of the spatial uniformity tests are presented in Table 2.2 for the various baffling systems. Monodisperse 15 μm aerodynamic diameter particles were the test aerosol and the input flow rate was 200 L/min. The aerosol concentrations were monitored at the five locations shown in Figure 2.2. The test procedure used was the same as that described for the unbaffled case.

The maximum range of aerosol concentration relative to the mean concentration for the five sampling positions presented in Table 2.2 are from 6 to 16%. The best chamber performance was achieved with a 15.2 cm diameter deflector with a 3.8 cm hole. This deflector configuration is currently used in the chamber. The range in aerosol concentration relative to the mean concentration was 6% for this system compared to 18% for the unbaffled case. Although the uniformity for the best ledge design was equilivalent for that obtained with a deflector, the particle loss for the ledge was 18% higher than that obtained for the deflector.

A final evaluation of the spatial uniformity was made with this baffling system at input aerosol flow rates of 80 and 300 L/min which corresponds to average downward velocities of 0.13 and 0.48 cm/sec. The test procedure was the same as indicated earlier with the particle sizes of 2.5, 10, and 15 μm aerodynamic diameter as the test aerosol. The relative particle concentrations, as a function of the particle size and input aerosol flow rate, are presented in Table 2.3 for the five sampling positions. Two to five runs were made for each indicated set of test conditions and the mean concentration of uranine at each location determined. The relative particle concentration in Table 2.3 was calculated by dividing the uranine concentration at each location by the average concentration at all locations for that run. The mean, presented in Table 2.3, and the coefficient of variation (CV) for the relative concentrations at each location was calculated. The CV ranged from 0.6 to 1% indicating the concentration variation between runs is within the measurement uncertainty of ±3%. A comparison of the mean concentration between locations for any particle size in Table 2.3 indicates the spatial uniformity. This comparison shows, except for the flow rate of 80 L/min, the concentrations are within ±3% of the average concentration of all locations.

Remember that the evaluation describe above has been performed with a stationary turntable. If the turntable were rotated, any variation in the concentration at the samplers would be eliminated. Even though the particle concentration uniformity for the case of a stationary turntable size is satisfactory for instrument evaluation, rotating the turntable would provide added assurance that the instruments are exposed to the same aerosol concentration.

As a test of the effectiveness of the rotating turntable to average out the non-uniform concentration, baffling in the upper portion of the chamber was arranged to skew the distribution as shown for the stationary case in Table 2.4. The particle size was 15 μm aerodynamic diameter and the aerosol flow rate was 200 L/min. Table 2.4 shows that the particle concentration samplers 1 and 3 deviated by 4% compared to the average. However, by rotating the table 30° once

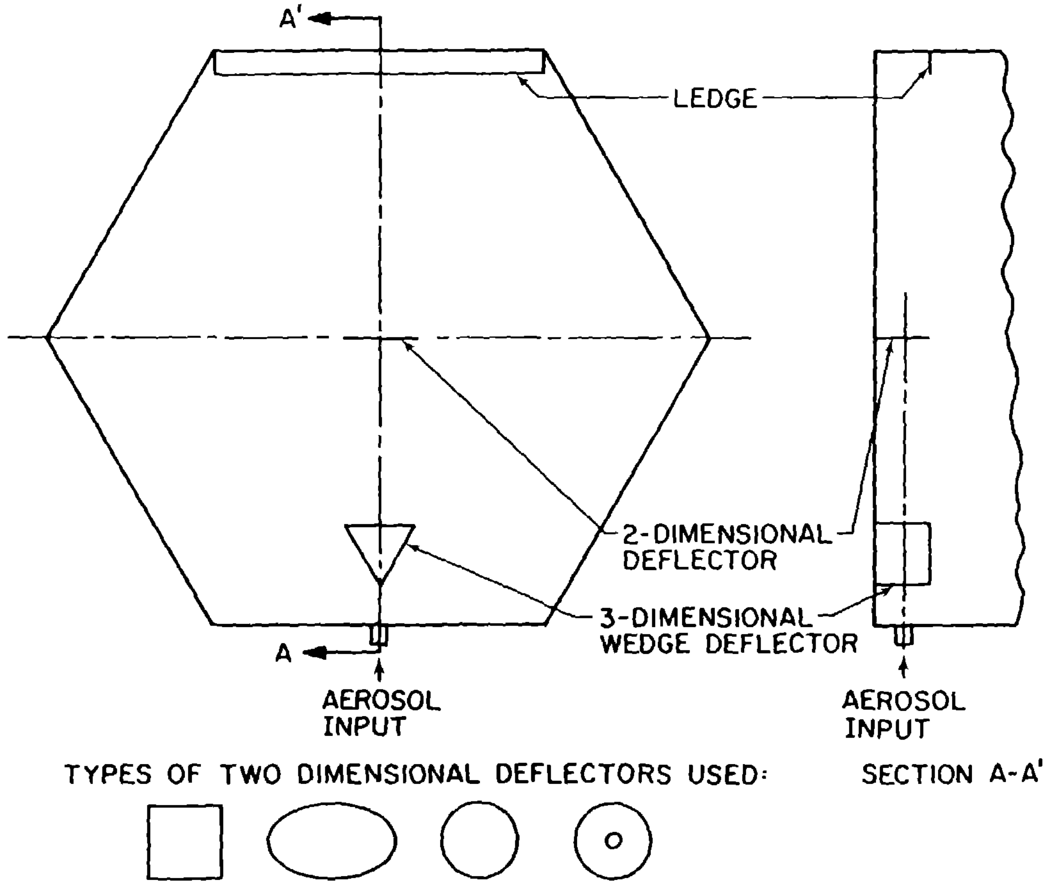

Figure 2.3. Schematic diagram showing the positioning of the various baffling designs within the upper chamber of the aerosol test chamber.

Table 2.3

Relative Particle Concentration as a Function of Location in the Chamber

Particle Diameter, µm	Aerosol Flow Rate 1/min	Relative Particle Concentration at Sampler 1	2	3	4	5
2.5	200	1.00	1.01	1.00	0.99	1.00
10	80	0.92	1.03	1.02	1.01	1.03
	130	1.01	1.01	1.01	0.97	1.01
	200	0.99	1.00	1.01	1.00	1.01
	300	1.03	0.99	1.00	0.99	1.00
15	80	0.95	1.01	1.01	0.99	1.05
	130	0.99	1.00	1.00	0.97	1.02
	180	1.02	1.00	0.97	0.99	1.02
	200	1.02	0.98	0.97	1.01	1.02
	300	1.00	1.01	1.00	1.00	1.00

Table 2.4

Effect of rotating turntable to achieve uniform particle concentrations at samplers on turntable (15 µm diameter particles, 200 1/min flow rate)

Turntable	Relative particle concentration at sampler 1	2	3	4	5
Stationary(1)	0.96	1.02	1.04	0.99	0.98
Rotating	0.99	1.01	1.01	1.00	0.99

(1) For the stationary case, the sampler number corresponds to the location number in Figure 4.

a minute for a 12 minute run, the particle concentration at the sampler was within 1% of the averages shown for the rotating case in the table.

2.4 Evaluation of Temporal Stability of Aerosol Concentration

Finally, the temporal stability of the aerosol concentration within the test section of the chamber was evaluated with both monodisperse liquid particles and coal dust aerosols. The results of a typical temporal stability test sequence are presented in Figure 2.4 for the monodisperse 15 μm diameter particles generated in the VOMA. These data were obtained by allowing the concentration to reach equilibrium in the chamber and then three 10 minute sample runs were obtained during a 55 minute time period. In Figure 2.4 the average particle concentration as obtained from two samplers operating simultaneously in each run (units are related to the uranine mass concentration and are arbitrary) are plotted as a function of time when the run was conducted. The horizontal and vertical length of the bars on the data points correspond to the duration and uncertainty of the concentration measurement, respectively. The mean concentration is presented as a solid line while the dashed lines represent ±5% deviation from this mean. This measurement uncertainty of ±5% was determined from error analysis of the flow rate and concentration measurements. The results show a 1% variation in the concentration during this time period.

To investigate the temporal stability of the fluidized bed dust generator and chamber combination, the output of a photometer, (GCA Model RAM-1) located in the chamber section, was recorded on a strip chart. A typical output is shown in Figure 2.5 for coal dust at a concentration of approximately 3 mg/m^3. The time constant of the RAM-1 response was set at 8 seconds. The strip chart shows no net change in the aerosol concentration during this 105 minute time period which is comparable to a normal instrument evaluation test period. The short term fluctuations (i.e. for periods less than one minute) can be seen to be less than 5% from the average.

2.5 Summary

The aerosol test chamber has been upgraded and extensively evaluated. The improvements include redesigning the turntable drive system and installing a baffle in the upper portion of the chamber to improve the uniformity of the aerosol spatial distribution. The temporal stability and spatial uniformity of the aerosols in the test selection were determined. Temporal stability tests show variations of less than 5% in the aerosol concentration. Variations in the spatial uniformity were found to be less than 3% for particles up to 15 μm diameter and aerosol flow rates ranging from 130 to 300 L/min. Thus, the environment in the aerosol test chamber provides an excellent setting for the simultaneous calibration and evaluation of numerous aerosol sensing instruments since all instruments are exposed to test aerosols with identical particle size distributions and concentrations.

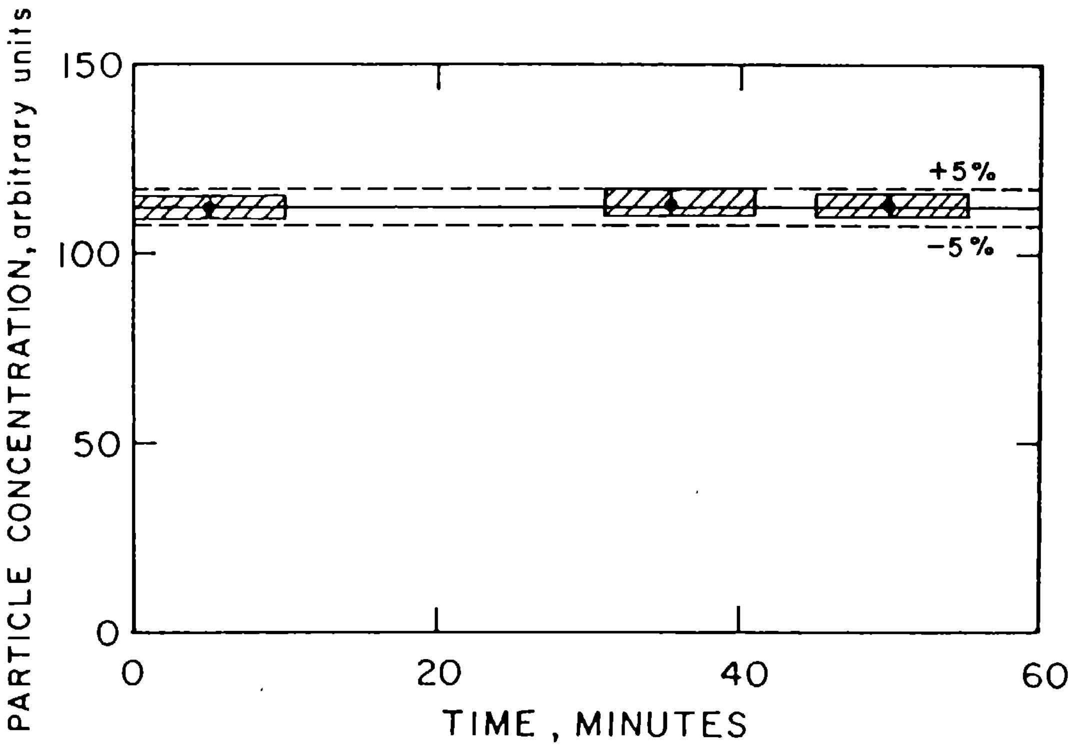

Figure 2.4. Relative concentration of 15 μm diameter particles in the aerosol test chamber as a function of time.

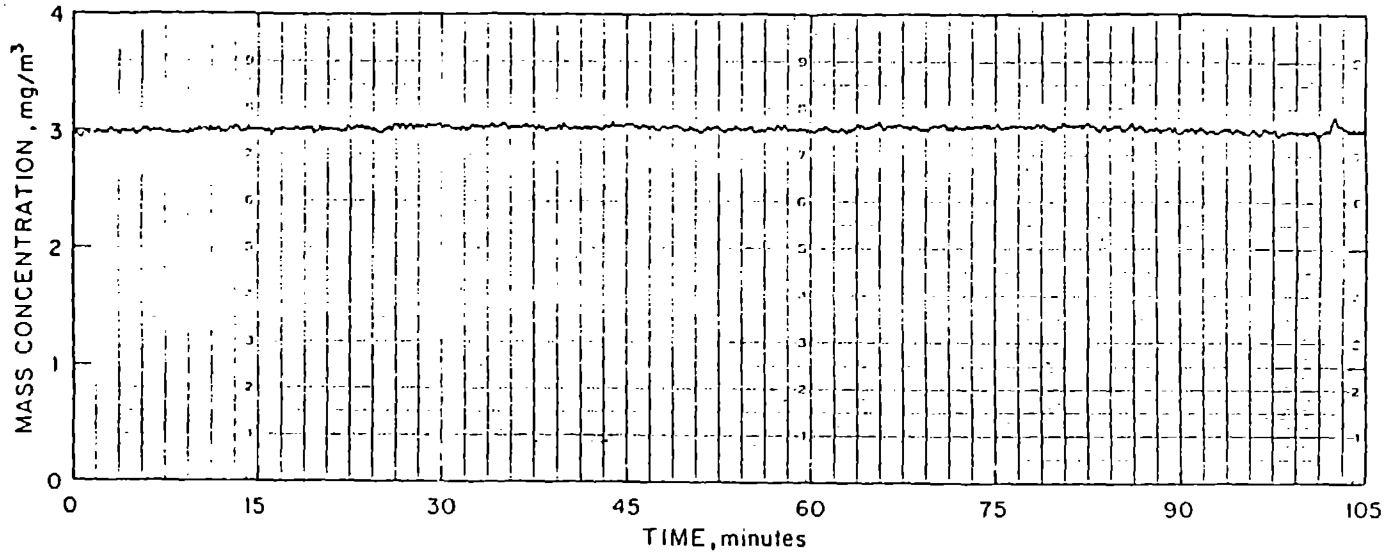

Figure 2.5. Stripchart record of the response from a photometer showing the temporal stability of the aerosol concentration in the aerosol test chamber when generated by a fluidized bed aerosol generator.

CHAPTER 3

DEVELOPMENT OF RESPIRABLE DUST STANDARDS

3.1 Introduction

To evaluate photometers in the aerosol test chamber, the photometer outputs must be compared to reference measurements made by samplers that have known sampling characteristics. Since the photometers have classifiers or optical configurations such that they respond primarily to particles in the respirable size range as defined by some criteria, usually either the American Conference of Governmental Industrial Hygienist (ACGIH) or the British Medical Research Council (BMRC) respirable criteria, the reference samplers or standards must also conform to the same criteria. A description of these two widely used criteria is given by Lippmann (4,5).

To perform the reference measurement of respirable dust in the dust chamber, two samplers were used. One sampler was a cascade impactor which gave the mass size distribution of the dust particles and the quantity of respirable dust was calculated from the size distribution. However, since the cascade impactor collects small amounts of particles on each impaction stage, errors can be introduced in the calculation of the respirable mass.

The other sampler was a single stage impactor followed by a filter. The penetration characteristics of this impactor simulate the respirable criteria. Here all respirable particles are collected on the same filter providing for better weighing accuracy than in the case of the cascade impactor. Since the photometers in the evaluation program had classifiers based on the ACGIH and the BMRC respirable criteria, two of these "respirable" impactors were run simultaneously; one with an ACGIH cutoff and the other with a BRMC. The two types of impactors used to make the reference respirable dust mass concentration measurements are described in the following sections.

3.2 Cascade Impactor

The cascade impactor used as a standard in our chamber was a Sierra Model 266 impactor designed specifically to follow theoretical collection efficiency curves. The design of this impactor is very similar to cascade impactors that have been used in our laboratory for many years. Since these impactors have been calibrated and successfully compared to theory many times in the past, the theoretical collection efficiency curves were used to predict the cut points of the various stages of this impactor.

However, one of the major problem areas of any cascade impactor is that solid particles may bounce off the stage on which they have been impacted and subsequently be collected in a stage further downstream that is intended to collect smaller particles. Thus, it is common practice to use a sticky coating on the impaction plate so the particles will stick when impacted.

A program was undertaken to determine the best sticky substance to use with this impactor in the environment of the aerosol test chamber. Several coatings including AFAX-800 and Apiezon Types H and L high vacuum greases and Hercules Industrial F. D. A Silicone Spray (Hercules Product Division, the Richardson

Company, 11061 Walden Road, Alden, NY 14004) were evaluated. The test procedure involved determining the particle collection characteristics of an impactor when sampling either liquid or solid monodisperse test aerosols. The solid aerosols were either polystyrene latex (PSL) or ammonium fluorescein particles. Liquid oleic acid particles were used to establish the base collection efficiency characteristics for the case of no particle bounce. For the case of the silicone spray, comparisons of the collection efficiency data obtained when sampling solid particles to that obtained with liquid particles showed no evidence of particle bounce. Varying degrees of particle bounce were found for all other coatings. The use of the silicone coating under this and other impactor evaluation projects (6,7) has shown this material to be a satisfactory impaction plate coating. The material possesses a unique combination of properties such as viscosity, surface tension, weight stability, ability to wick through layers of deposited particles, low chemical background and ease of application.

3.3 Respirable Impactor

The respirable impactor as defined above is shown in Figures 3.1 and 3.2. The respirable impactor nozzle plate consists of a number of nozzles of different diameters so the respirable curve can be approximated as described in reference 3. For this work, the nozzle plates are designed with three sizes so that the respirable curves are approximated in three steps. The design parameters for nozzle plates are shown in Table 3.1. The particles penetrating the impactor are collected on a 37 mm filter from which the concentration is measured gravimetrically and this is used as a standard to which the photometers are compared.

The impaction plates are rotated to spread the deposit over a large area. To insure that particle bounce is not a problem, the impaction plates are made of a porous metal saturated with a light mineral oil type NF-9 so the oil continually wicks up through the deposit presenting the incoming particles with a fresh oiled surface. Previous tests performed with this oil impregnated porous implation plate show no indication of particle bounce (8). Gear motors are used to rotate the impaction plate.

The nozzle plates of the respirable impactors can be interchanged and designs have been made which will approximate either the ACGIH or the BRMC respirable criteria at flow rates of either 10 or 30 L/min. These flow rates were chosen so a reasonable sampling time can be used for any aerosol concentration that might be used in the chamber. For example, for large concentrations the 10 L/min impactors operating for several minutes will provide an accurate sample for gravimetric analysis. However, for lower concentrations a flow rate of 30 L/min is necessary to keep sampling times at reasonable lengths. For any one test two samplers are operated in the chamber; one with a ACGIH penetration characteristics and the other with the BMRC.

3.4 Comparison of Cascade and Respirable Impactors

Similar size respirable impactors have been previously built (8,9) and their cutoff characteristics have always been shown to agree well with the predicted theoretical cutoff characteristics and the particle respirable criteria they are intended to approximate. Because of the relevance to this work, a reference is presented in Appendix A. Thus, the particle cutoff characteristics of these

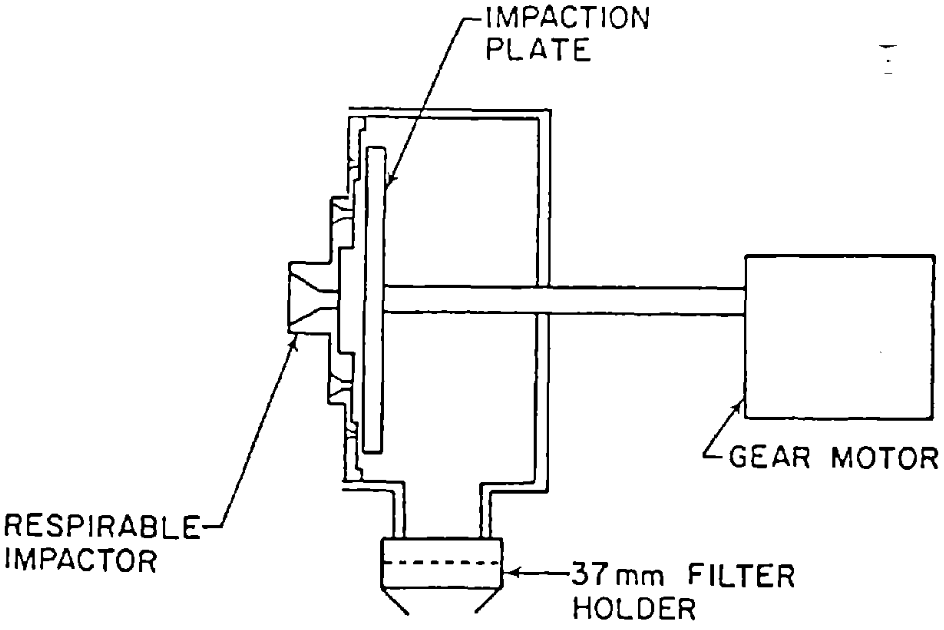

Figure 3.1. Schematic diagram of the impactor for the respirable dust standard.

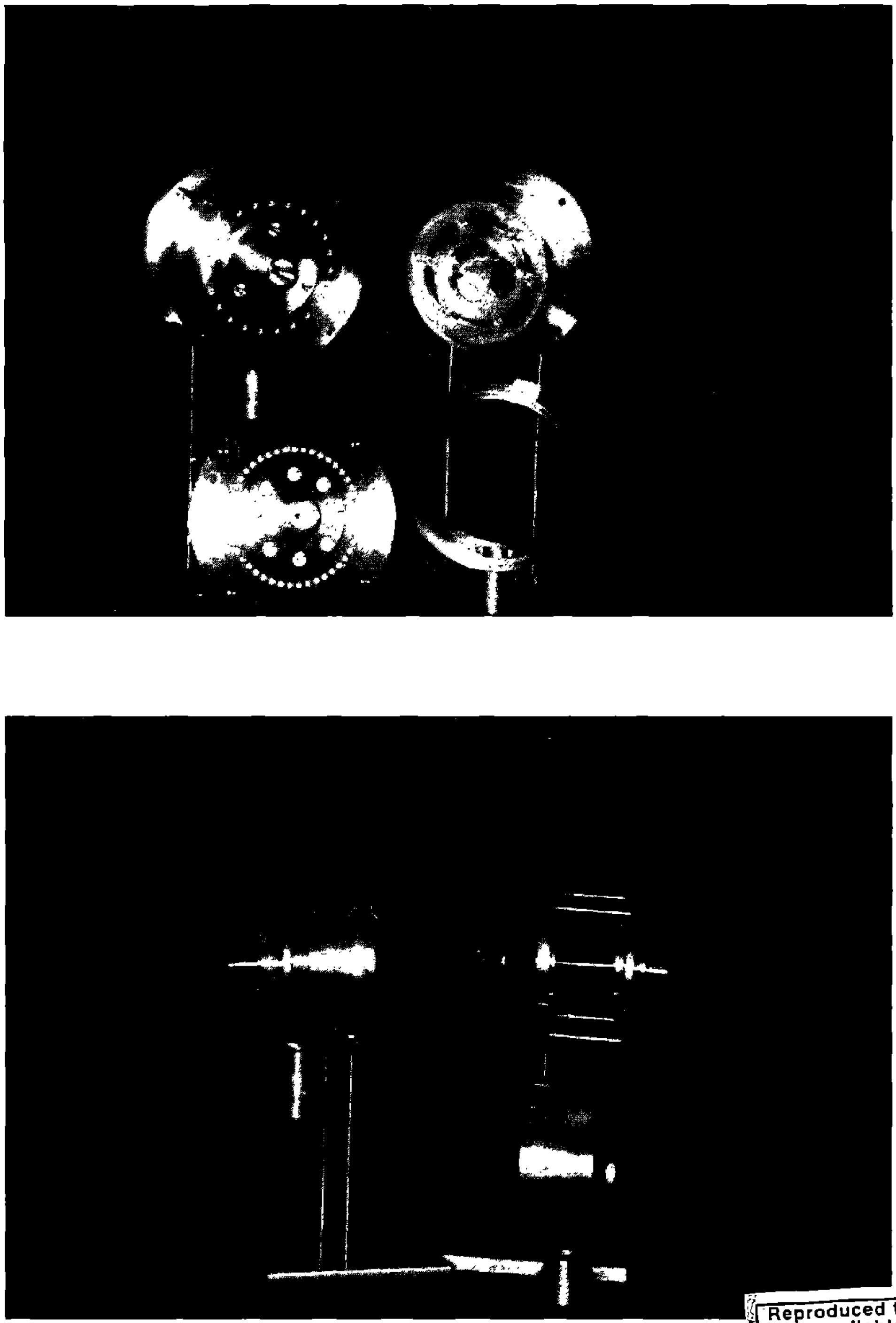

Figure 3.2. Photographs of assembled and partially disassembled respirable impactors.

Table 3.1

Design Parameters For Respirable Impactor Nozzles

Respirable Criteria	Total Flow Rate, l/min	Nozzle Particle Cut-off Diameter, µm	Nozzle Diameter, cm	No. of nozzles
ACGIH	10	5.8	0.408	1
		3.5	0.150	8
		2.2	0.061	45
	30	5.8	0.589	1
		3.5	0.217	8
		2.2	0.088	45
BMRC	10	6.4	0.436	1
		5.0	0.266	3
		2.9	0.091	23
	30	6.4	0.628	1
		5.0	0.383	3
		2.9	0.131	23

Table 3.2

Comparison of Respirable Dust Measurements

		Respirable Mass Concentration, mg/m³				Ratio	
	Total Mass	Respirable Impactor[2]		Calculated[3]		Calc./Resp. Impactor	
Run	Concentration[1], mg/m³	ACGIH	BMRC	ACGIH	BMRC	ACGIH	BMRC
1	1.26	0.46	0.69	0.63	0.70	1.37	1.02
2	1.93	0.94	1.16	1.00	1.12	1.06	0.97
3	9.00	4.9	5.7	5.2	5.8	1.07	1.03
4	10.8	5.4	6.2	5.6	6.3	1.03	1.01

[1] Obtained using upward facing, open face filter sampler.

[2] Obtained using respirable impactor designed for either the ACGIH or BMRC criteria.

[3] Calculated from aerosol size distribution obtained with Sierra Model 266 cascade impactor.

impactors were not experimentally determined.

A series of tests were performed to demonstrate the validity of using the respirable impactor technique to determine the respirable dust concentration. This involved a comparison of the respirable dust collected after the respirable impactors to that calculated from the size distribution measured by the cascade impactor described earlier. The data for this comparison are presented in Table 3.2. The calculated respirable concentration from the cascade impactor data was computed by applying either the ACGIH or BMRC respirable dust criteria to the size distribution obtained with the cascade impactor. The ratio of the calculated respirable mass concentration to that determined by the respirable impactor measurement for each respirable dust criteria is also shown in Table 3.2. The ratios show good agreement between the two techniques. The average difference in mass concentration is only 4% which is within the measurement uncertainty which is 5%, if one excludes the data obtained for the ACGIH criteria from Run 1. The respirable impactor technique is in close agreement with the standard measurement techniques of the cascade impactor and is much simpler method for obtaining the respirable mass of the dust.

3.5 Summary

Two respirable impactors were designed, built and tested. These impactors have particle penetration characteristics defined by the ACGIH and the BMRC respirable dust criteria. Comparisons of the respirable mass obtained through use of the respirable impactors are in close agreement with the data obtained by computing the respirable mass from applying either the ACGIH or the BMRC respirable dust criteria to the size distribution data obtained with conventional cascade impactors. The respirable impactor technique is much simpler and quicker than a cascade impactor for obtaining the respirable mass of a dust aerosol.

CHAPTER 4

PHOTOMETER EVALUATION AND CALIBRATION

4.1 Introduction

Photometers have become increasing popular during the last few years as a means of determining the respirable mass concentration of airborne aerosols. However, photometers, unlike true mass sensing instruments, do not directly measure the aerosol mass concentration, but rather measure the quantity of light scattered from a light beam passing through the aerosol cloud. The quantity of scattered light is a function of the number and size of the particles in the aerosol cloud as well as the index of refraction and shape of the particles. Although photometers are designed to be sensitive to only the mass concentration of the aerosols, other aerosol properties also influence the instrument response requiring the empirical calibration of these instruments.

Although several photometer evaluation programs have been conducted (2, 10-12), the primary objective of this study was to evaluate the mass sensing capabilities of several newly developed, commercially available photometers. The study, which was divided into two parts, specifically involved determining the photometer response as a function of respirable mass concentration, particle size distribution and particle composition. The first part, the results of which are presented in Sections 4.2 and 4.3, involved determining the response of 14 different photometers to various dust aerosols. The second part, reported in Section 4.4, dealt with the response of the GCA RAM-1 to liquid droplets.

4.2 Description of Photometers and Test Procedures

The photometers evaluated during this contract are listed by manufacturer and model in Table 4.1. The number of units of each type are also given. A total of 8 photometer models from 5 manufacturers were included in the tests. The manufacturers were GCA Corporation (Bedford, MA), Ernst Leitz, GmbH. (Wetzler, West Germany), ppm. Inc. (Knoxsville, TN), Sibata Chemical Apparatus, Co., Ltd. (Tokyo, Japan), and TSI, Inc. (St. Paul, MN).

A complicating factor in the evaluation of photometers is that they often are designed to measure only the respirable dust concentration. This may be accomplished by the placement of an aerosol preclassifier on the inlet to the instrument or through the arrangement of the optics and type of light source used. The three different respirable dust criteria utilized by the photometers studied here are the American Conference of Governmental Industrial Hygienists (ACGIH), the British Medical Research Council (BMRC), and the German TBF 50-II criteria. The fraction of respirable dust as a function of aerodynamic particle size for the ACGIH, BMRC and TBF 50-II criteria are presented in Figure 4.1 The response of the GCA RAM-1 and MINIRAM, the TSI Model 5150 and the ppm, Inc. HAM are based on the ACGIH respirable criteria. The particle penetration curve for the Sibata P-5 inlet most closely resembles the BMRC criteria. The German TBF 50-II criteria is applicable to the Leitz Tyndallometer.

For this study, the ACGIH criteria is also applicable to the ppm, Inc. PCAM and PCAM-TX. The PCAM was modified for these experiments by replacing the vertical elutriator inlet with a modified inlet cap and a 10 mm nylon cyclone. The

Table 4.1

Summary of Photometers Evaluated During Contract

Manufacturer	Model	Units Tested
GCA	RAM-1	4
	MINIRAM	3
Leitz	Tyndallometer TM Digital	1
ppm, Inc.	PCAM	1
	PCAM-TX	1
	HAM	2
Sibata[1]	P-5	1
TSI, Inc.	5150	1

[1] Marketed by MDA Scientific, Inc. (Glenview, Ill.)

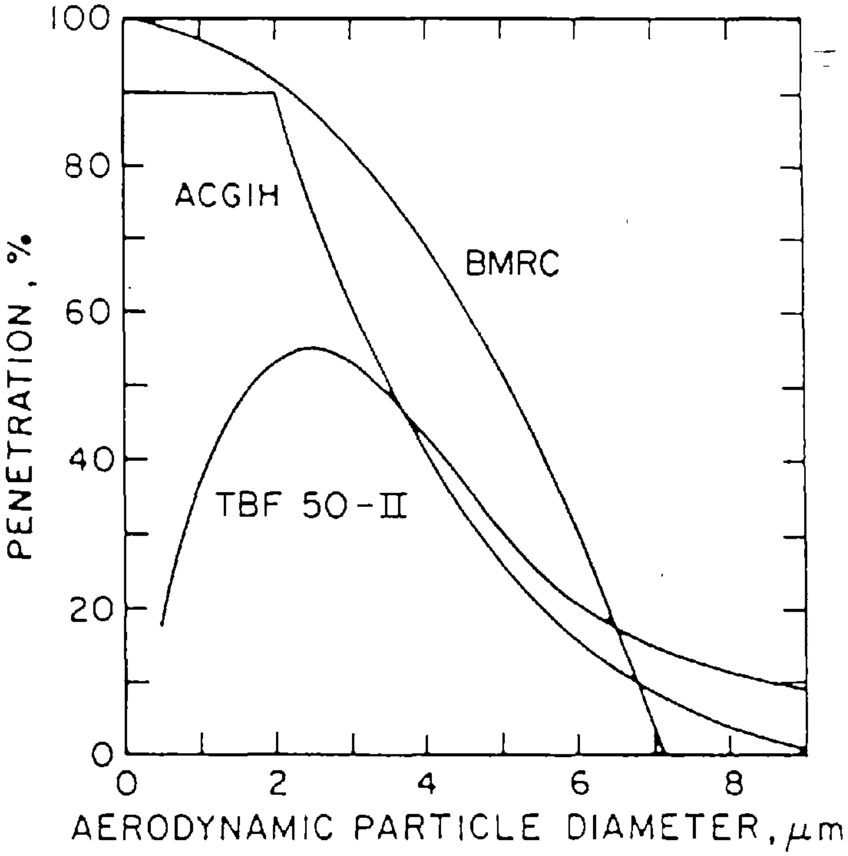

Figure 4.1. ACGIH, BMRC and TBF 50-II respirable dust criteria.

modified inlet cap was supplied by the manufacturer specifically for use in this study. For the PCAM-TX, the ACGIH equivalent mass concentration was calculated from the mass size distribution output of the instrument. The data output of this instrument are in terms of the quantity of mass greater than 7 particle sizes ranging from 2 to 10 μm diameter.

The photometers were evaluated with several different aerosols to determine their response as a function of particle size distribution and particle composition. These aerosols were generated with the TSI Model 3400 fluidized bed aerosol generator. Five different dusts were generated with this aerosol generator, four of which were different coal dusts. The different coal dusts are identified here as "Coal", "Classified Coal", "Coal:0-10", and "Coal:10-30". The material identified as "Coal" and "Classified Coal" are both Illinois No. 6 coals. The size distribution of the later coal was narrowed by removing a portion of the smallest and largest particles. "Coal:0-10" and "Coal:10-30" are from the same coal sample and are the fine and coarse particle fraction from a Donaldson Majac classifier. The particle cut was made at 10 μm. The last dust used was AC Fine Arizona road dust (ARD) (AC Spark Plug Div., General Motors Corp., Flint, MI). The densities of the "Coal" and Arizona road dust particles were measured to be respectively 1.45 and 2.61 gm/cm^3 (13).

For several of the tests dusts, two different particle size distributions were used in the evaluations. These are referred to as "-I" and "-II". The -I and -II refer respectively to dusts generated with the fluidized aerosol generator without and with the aerosol passing through a cyclone placed at the exit of the generator to remove the large particles. This allowed for two size distributions of the same test dust to be used in the evaluation.

The mass size distributions of these test dusts are presented in Figure 4.2 These distribution were obtained using a Sierra Model 266 cascade impactor (Sierra Instruments, Inc., Carmel Valley, CA). The mass median diameter (MMD) and geometric standard deviation (σ_g) of each aerosol are also presented in Figure 4.2 The MMD of the coal aerosols ranged from 2.0 to 14.0 μm. The ARD aerosols had MMD's of 1.5 and 3.8 μm.

The evaluation tests were performed by placing all instruments into the aerosol test chamber and simultaneously exposing them to the dust aerosols. The instruments include the photometers, open-faced filter samplers, ACGIH and BMRC respirable impactors and a cascade impactor. The response from each photometer was then compared to the respective respirable mass concentration which was determined gravimetrically from the impactors. This response was obtained by averaging 10 to 30 concentration readings obtained at 1 minute intervals during the test run. The uncertainty in the gravimetrically determined mass concentration was ±5%.

The total aerosol mass concentration was determined by gravimetric analysis of the material collected by the open-faced filter samplers. These samplers were 37 mm plastic filter cassettes.

The respirable mass concentration for the ACGIH and BMRC criteria were determined using the respirable impactors described in Chapter 3. Each unit was operated at a sample flow rate of 10 L/min. The respirable mass concentration was found through gravimetric analysis of the material deposited on the after-filter in the respirable impactor sampler.

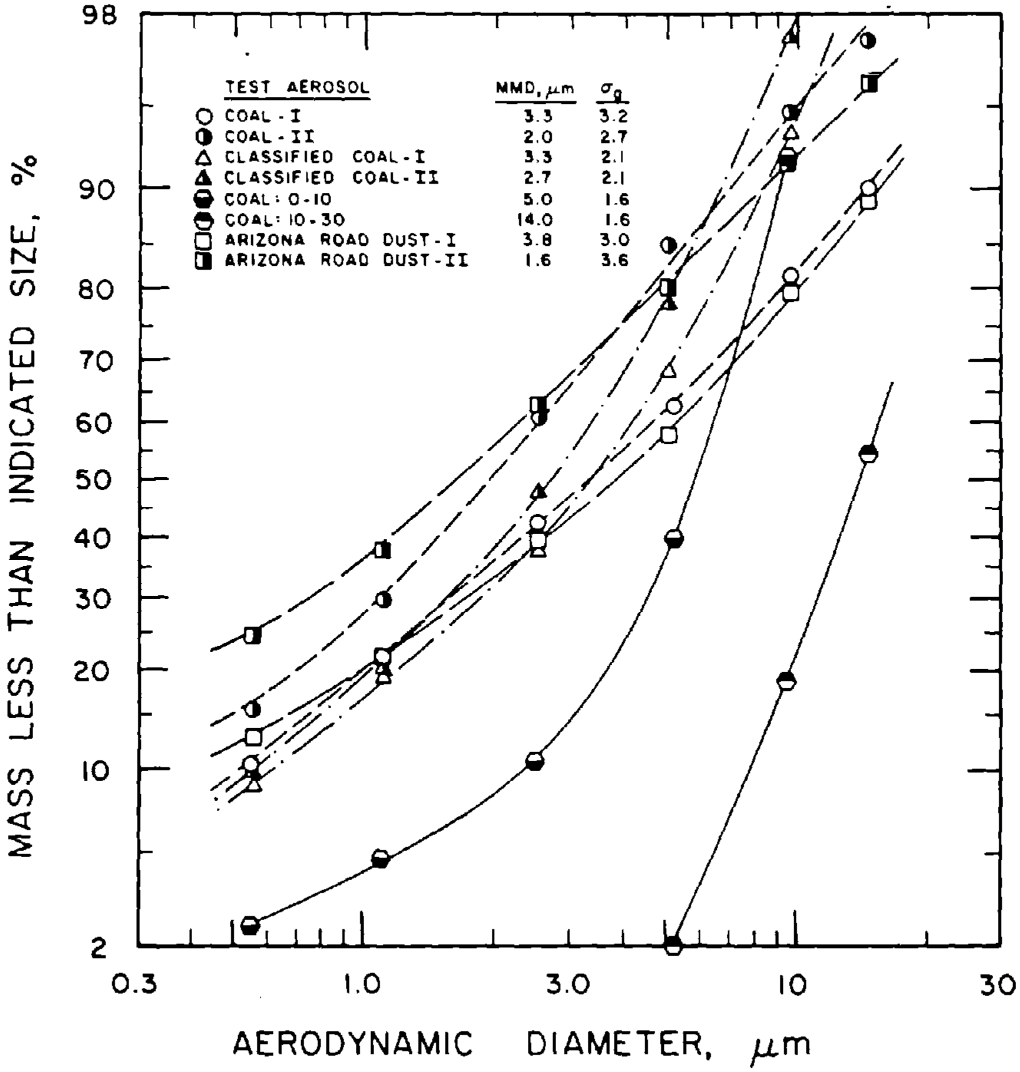

Figure 4.2. Size distribution of test dusts in the aerosol test chamber.

For these evaluations all electronic adjustments and the flow rates of each photometer were set according to the manufacturer's specifications. The one exception was the flow rate through the PCAM which was changed from 1.85 to 2 L/min for proper operation of the 10 mm cyclone preclassifier.

4.3 Dust Aerosol Test Results

Summaries of the photometer calibration data are presented in Tables 4.2 to 4.4 and Figure 4.3 - 4.13. The data are given in three separate data sets which correspond to the three test series conducted during the contract. Listed in the table for each test are the mass concentrations corresponding to the three respirable dust criteria and the mass concentration readings from the photometers. One must be careful to compare the instrument response to the appropriate respirable dust criteria. Respirable mass concentrations ranged from approximately 0.15 to 18 mg/m^3.

The response from all instruments except the TSI and Sibata photometers read out directly as mass concentration in units of mg/m^3. For the TSI and Sibata photometers, the mass concentration is read out in unit of counts/minute. Consequently, the user must either use the instrument's calibration curve or the empirically determined conversion factor in order to relate counts/minute to mass concentration.

The results indicate that the response of all photometers is a linear function of the respirable mass concentration of the test aerosol. This linear response was found to exist over the entire range of aerosol concentrations used in this study which were varied from 0.15 to 18 mg/m^3.

Based on the observed linear response characteristics of these photometers, linear regression analysis was performed on the data obtained with each photometer. The analysis assumed that the response of each photometer was directly proportional to the respirable mass concentration. The resulting regression coefficients are presented in Table 4.5. A regression coefficient of 1 would mean that the response of the instrument was equal to the actual respirable mass concentration. A value of 0.8, for example, would indicate that the response was 80% of the actual respirable concentration. The average regression coefficients for the GCA RAM-1 and MINIRAM range from 0.66 to 1.04 and 0.59 to 1.08 respectively. For the ppm HAM, PCAM and PCAM-TX the average regression coefficients range from 0.98 to 1.57, 0.60 to 0.96 and 0.98 to 1.28 respectively. In general, the data show that the relative response of any photometer increases with decreasing particle size of the test dust. The response is also greater for Arizona road dust than for coal dust. The response of the ppm PCAM-TX and the TSI Model 5150 photometers show the least influence from particle size and dust type.

For a given photometer model and test dust, the regression coefficients can be used for intra-unit variability comparisons. Data for two GCA RAM-1's, 3 GCA MINIRAM's and two ppm HAM's are presented in Table 4.5. The comparison of the regression coefficients for each model type show the response of the RAM's, MINIRAM's and HAM's generally differed by 31, 7 and 4% respectively. However, maximum differences of 83, 49 and 56% respectively were observed for these three models.

Table 4.2

Photometer Calibration Data
(First Test Series)

Run	Dust Type	Respirable Mass Concentration, mg/m^3, For Criteria:			Instrument Response, mg/m3 (1), for listed instruments (2)(3)					
					GCA RAM -I		ppm PCAM	Leitz Tyndallometer	Sibata P-5	TSI 5150
		ACGIH	BMRC	TBF 5011	1097	1098	6-106-009	575	391646	98343
1	Coal-I	0.63	0.70	0.34	0.447	0.481	0.337	0.21	16	48
2		1.00	1.12	0.52	0.768	0.825	-	0.38	-	73
3		5.20	5.80	2.74	5.36	5.59	4.74	2.65	168	-
4		5.60	6.30	2.97	5.03	5.21	4.05	2.60	159	409

1. Except for TSI and Sibata, Counts/min.
2. Instruments listed by serial number.
3. Respirable criteria associated with each instrument

Instrument	Criteria
GCA RAM-1	ACGIH
ppm PCAM	ACGIH
Leitz Tyndallometer	TBF 50-11
Sibata P-5	BMRC
TSI	ACGIH

Table 4.3
Photometer Calibration Data
(Second Test Series)

		Respirable Mass Concentration, mg/m^3		Instrument Response, mg/m^3(1), for listed instruments (2)(3)					
Run	Dust Type	ACGIH	BMRC	GCA RAM-1 1263	GCA RAM-1 1268	ppm PCAM 6-106-009	ppm PCAM-TX -	Sibata P-5 391646	TSI 5150 98343
1	Coal-II	1.00	-	0.98	0.81	0.90	1.25	-	37
2		1.11	-	1.04	0.83	1.00	1.35	95	-
3		1.26	1.38	1.25	1.02	1.50	1.23	113	45
4		1.35	-	1.14	0.88	-	1.39	106	42
5		1.57	1.52	2.15	1.37	1.00	1.65	154	61
6		1.75	-	2.49	1.57	1.50	2.08	175	70
7		2.98	3.22	3.54	2.77	1.80	2.51	264	112
8		4.10	4.32	3.74	2.85	2.50	3.29	271	112
9		5.44	6.01	6.75	4.69	4.65	6.46	511	215
10		5.47	5.81	6.66	4.37	-	-	467	210
11		5.51	6.39	6.58	4.32	4.80	7.16	475	-
1	Classified Coal-I	3.37	-	3.28	2.13	1.29	3.66	202	104
2		3.70	5.01	3.46	2.25	-	-	204	-
3		4.66	6.32	4.49	3.20	2.71	4.85	280	139
4		4.72	6.22	4.28	3.15	-	-	255	129
5		7.50	-	7.17	5.25	4.29	8.01	-	210
6		7.55	10.07	7.16	5.34	-	-	-	223
7		11.89	16.85	12.30	8.68	7.58	-	695	376
8		12.26	16.82	12.33	9.00	-	11.5	698	370
9		17.67	-	14.60	12.40	-	-	1159	534
10		18.75	31.86	14.45	12.66	-	-	1173	585
11		20.26	-	17.32	14.21	-	-	1267	700
12		21.25	-	17.89	14.35	-	-	1324	738
1	Classified Coal-II	3.66	4.68	4.00	2.87	2.45	4.20	244	-
2		4.15	5.25	5.07	3.02	2.47	4.70	250	-
3		8.44	10.71	7.45	6.41	-	-	497	261
4		8.85	10.79	7.27	6.48	10.59	11.87	534	278
5		12.14	-	11.98	10.27	-	-	795	398
6		13.15	17.15	12.43	10.60	-	-	830	420
7		16.59	22.60	17.15	13.71	-	-	1092	558
8		18.57	25.71	17.65	14.70	-	-	1180	562
1	Arizona Road Dust-I	1.58	1.64	2.11	1.31	1.92	1.30	310	61
2		2.65	2.75	2.78	2.39	2.54	1.92	470	93
3		4.04	5.48	4.67	3.34	4.46	4.46	803	175
4		4.28	5.88	3.96	2.94	-	-	800	167
5		4.46	5.86	4.07	3.01	5.29	4.71	820	164
6		5.88	8.10	5.10	3.51	-	-	1006	231
7		5.93	8.37	5.40	3.47	4.62	4.83	1009	248
8		7.39	10.05	7.35	5.25	-	-	1305	301
9		7.79	10.02	7.48	5.42	6.98	8.01	1359	315
10		8.84	11.49	7.64	5.44	6.62	10.49	1524	323
11		9.16	12.53	8.39	5.70	-	-	1579	359
12		11.06	14.75	10.49	6.91	-	9.16	1879	375
13		12.95	16.14	11.32	7.47	-	-	2023	438

Table 4.3, Continued
Photometer Calibration Data
(Second Test Series)

		Respirable Mass Concentration, mg/m^3		Instrument Response, mg/m^3(1), for listed instruments (2)(3)					
Run	Dust Type	ACGIH	BMRC	GCA RAM-1 1263	GCA RAM-1 1268	ppm PCAM 6-106-009	ppm PCAM-TX -	Sibata P-5 391646	TSI 5150 98343
1	Arizona	2.20	2.77	1.66	1.21	-	-	364	66
2	Road	2.21	2.58	1.60	1.18	1.85	2.05	361	65
3	Dust-II	2.96	3.38	2.92	2.05	-	-	503	100
4		3.34	4.35	3.22	2.23	3.12	2.82	556	110
5		8.00	10.44	7.74	5.86	-	-	1356	264
6		8.20	9.89	7.70	5.65	7.98	7.89	1388	254

[1] Except for TSI and Sibata, counts/min.

[2] Instruments listed by serial number.

[3] Respirable criteria associated with each instrument:

Instrument	Criteria
GCA RAM-1	ACGIH
ppm PCAM	ACGIH
ppm PCAM-TX	ACGIH
Sibata	BMRC
TSI	ACGIH

Table 4.4

Photometer Calibration Data (Third Test Series)

		Mass Concentration, mg/m^3			Instrument Response, mg/m^3, (1)(2)							
		Respirable		Total	GCA RAM-1		GCA MINIRAM			ppm HAM		TSI
Dust Type	Run	ACGIH	BMRC		1263	1268	3	5	6	007	014	98343
Classified Coal-I	1	0.15	0.16	0.19	-	-	0.13	0.11	0.08	-	0.184	
	2	0.18	0.19	0.23	-	-	0.13	0.13	0.10	-	-	14
	3	2.91	3.80	-	2.40	1.72	2.32	2.55	2.12	3.51	3.51	100
	4	3.03	3.64	5.13	2.23	1.63	2.32	2.54	2.10	3.28	3.56	92
	5	3.09	3.88	5.35	2.27	1.67	2.37	2.42	1.90	3.36	3.60	95
	6	4.67	5.91	7.76	3.97	2.95	3.93	4.30	3.67	5.86	6.22	163
	7	4.93	5.98	8.03	4.14	3.08	4.01	4.39	3.78	6.05	6.32	161
	8	11.8	15.2	17.1	9.45	6.56	8.59	9.05	8.49	15.1	14.1	412
	9	12.6	16.2	23.8	10.41	7.21	10.3	10.0	9.24	16.9	15.6	426
	10	12.5	16.3	24.7	10.45	7.38	10.2	9.92	9.44	17.8	15.9	430
Classified Coal-II	1	2.22	2.85	2.91	2.76	2.14	2.48	2.50	2.50	3.35	3.94	89
	2	2.54	3.28	3.20	2.77	2.16	2.54	2.60	2.25	3.29	4.13	95
	3	3.68	4.67	5.18	4.13	2.92	3.75	3.83	3.45	5.18	5.89	137
	4	4.14	5.08	5.72	4.41	3.12	3.83	3.99	3.70	5.30	5.95	140
	5	5.90	7.58	-	5.91	4.35	5.67	-	5.23	8.17	8.38	225
	6	5.92	7.24	-	6.25	4.42	-	-	4.99	8.75	8.88	234
	7	6.28	7.12	-	6.21	4.53	5.83	-	5.43	9.16	9.22	234
	8	9.69	12.0	13.8	9.85	7.23	8.58	-	7.57	-	14.78	375
Coal:0-10	1	1.87	2.77	5.38	1.57	1.00	0.72	1.16	1.22	1.82	1.66	-
	2	1.93	3.01	5.51	1.55	1.07	0.70	1.21	1.33	1.93	1.63	-
	3	5.7	8.9	23.0	4.36	2.77	2.78	5.01	4.33	5.67	5.76	-
	4	5.9	9.1	23.7	4.51	2.66	2.80	5.09	4.37	5.90	5.94	-
	5	7.6	11.3	25.8	5.22	3.46	3.16	5.77	4.89	7.62	7.24	-
	6	7.9	12.4	28.7	6.01	3.80	3.80	6.18	5.29	7.47	7.84	-
	7	14.6	20.8	47.0	11.15	6.87	5.61	10.2	9.45	15.67	13.90	-
	8	15.2	21.7	47.1	10.84	6.45	6.28	9.67	9.58	15.41	13.90	-

Table 4.4 Continued
Photometer Calibration Data (Third Test Series)

		Mass Concentration, mg/m^3			Instrument Response, mg/m^3, (1)(2)							
		Respirable		Total	GCA RAM-1		GCA MINIRAM			ppm HAM		TSI
Dust Type	Run	ACGIH	BMRC		1263	1268	3	5	6	007	014	98343
Coal:0-10[3]	1	1.74	2.29	5.45	1.39	1.03	0.31	0.72	-	1.70	1.61	-
	2	1.76	2.54	5.69	1.48	1.07	0.34	0.77	-	1.67	1.67	-
	3	5.6	8.4	14.4	4.09	2.60	1.42	3.82	2.67	5.30	5.28	-
	4	5.3	8.8	-	4.25	2.58	1.45	3.85	2.70	5.60	5.45	-
	5	7.8	12.5	27.4	5.40	4.17	2.56	4.56	3.81	7.38	7.41	-
	6	7.9	11.6	-	5.54	4.20	2.61	4.60	3.85	8.18	8.01	-
	7	12.4	17.9	40.7	9.70	6.40	3.58	6.24	5.21	12.40	12.13	-
	8	13.0	17.8	38.8	9.80	6.64	3.65	6.24	5.65	11.93	11.94	-
Coal:10-30	1	0.27	0.48	16.8	0.22	0.10	0.14	0.20	-	0.17	0.55	-
	2	0.31	0.38	19.6	0.32	0.12	-	0.28	-	0.24	0.48	-
	3	0.32	0.41	19.6	0.29	0.12	-	0.33	-	0.40	0.50	-
ARD-I	1	1.87	2.21	2.76	2.16	1.76	1.98	2.11	2.13	2.67	2.50	78
	2	1.91	2.15	2.82	2.10	1.72	-	2.05	2.06	2.60	2.53	-
	3	1.97	-	2.96	2.17	1.78	2.10	2.17	2.15	2.62	2.54	78
	4	3.39	3.95	4.66	4.09	3.24	3.61	3.84	3.83	4.13	4.95	130
	5	3.42	3.98	4.91	4.07	3.26	3.64	3.86	3.88	4.87	4.99	134
	6	4.57	4.96	6.77	5.07	3.97	4.83	5.10	4.74	7.38	6.88	161
	7	4.91	5.38	6.73	5.61	4.25	4.97	5.26	4.99	7.97	7.19	168
	8	7.85	-	11.05	8.79	7.24	7.92	8.44	7.96	13.12	12.23	-
	9	7.96	8.30	9.95	9.13	7.61	8.52	9.06	8.89	13.38	12.63	285
ARD-II	1	1.50	1.52	-	1.51	1.23	1.34	1.45	1.47	1.78	1.69	53
	2	1.53	1.50	1.78	1.71	1.37	1.47	1.57	1.49	1.93	1.86	58
	3	2.63	2.74	-	3.06	2.48	2.62	2.92	2.94	3.68	3.59	97
	4	2.73	2.72	2.71	2.94	2.42	2.60	2.79	2.85	3.57	3.48	94
	5	2.89	2.87	2.98	3.11	2.54	2.78	3.01	3.04	3.75	3.64	102
	6	4.46	5.04	4.91	5.39	4.41	4.92	5.27	5.19	7.32	7.21	163
	7	4.65	5.08	4.93	5.34	4.44	4.97	5.36	5.22	7.46	7.32	165
	8	7.52	7.91	8.16	8.31	6.85	7.72	8.33	7.52	10.52	11.04	252
	9	8.43	9.10	8.96	9.84	7.86	8.92	9.63	9.06	13.24	12.83	293

[1] Except for TSI in counts/min.

[2] Instruments listed by serial number.

[3] GCA MINIRAM operated in active sampling mode using cyclone sampler during these tests. For all other tests the MINIRAM was operated in passive sampling mode.

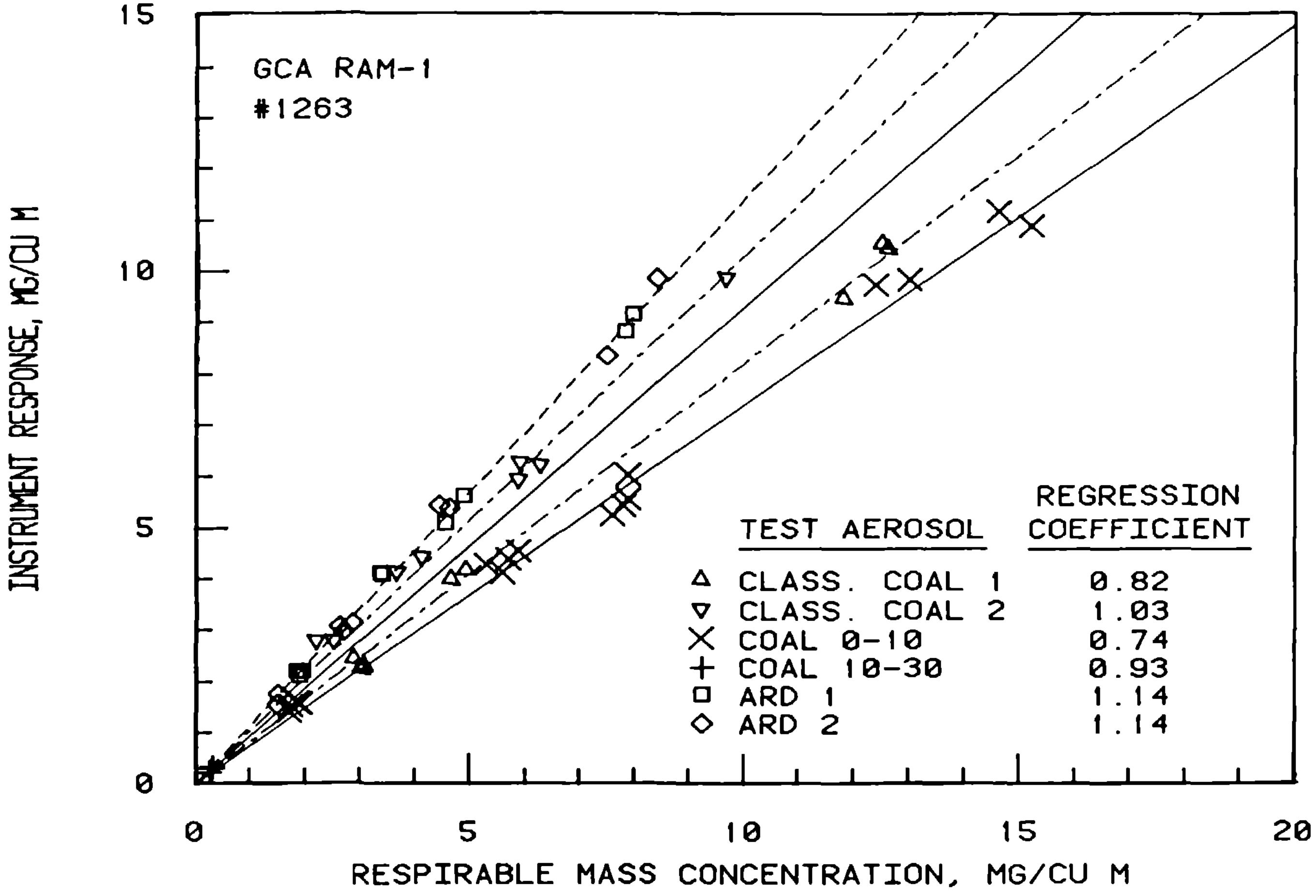

Figure 4.3. Calibration data for GCA RAM-1 serial number 1263.

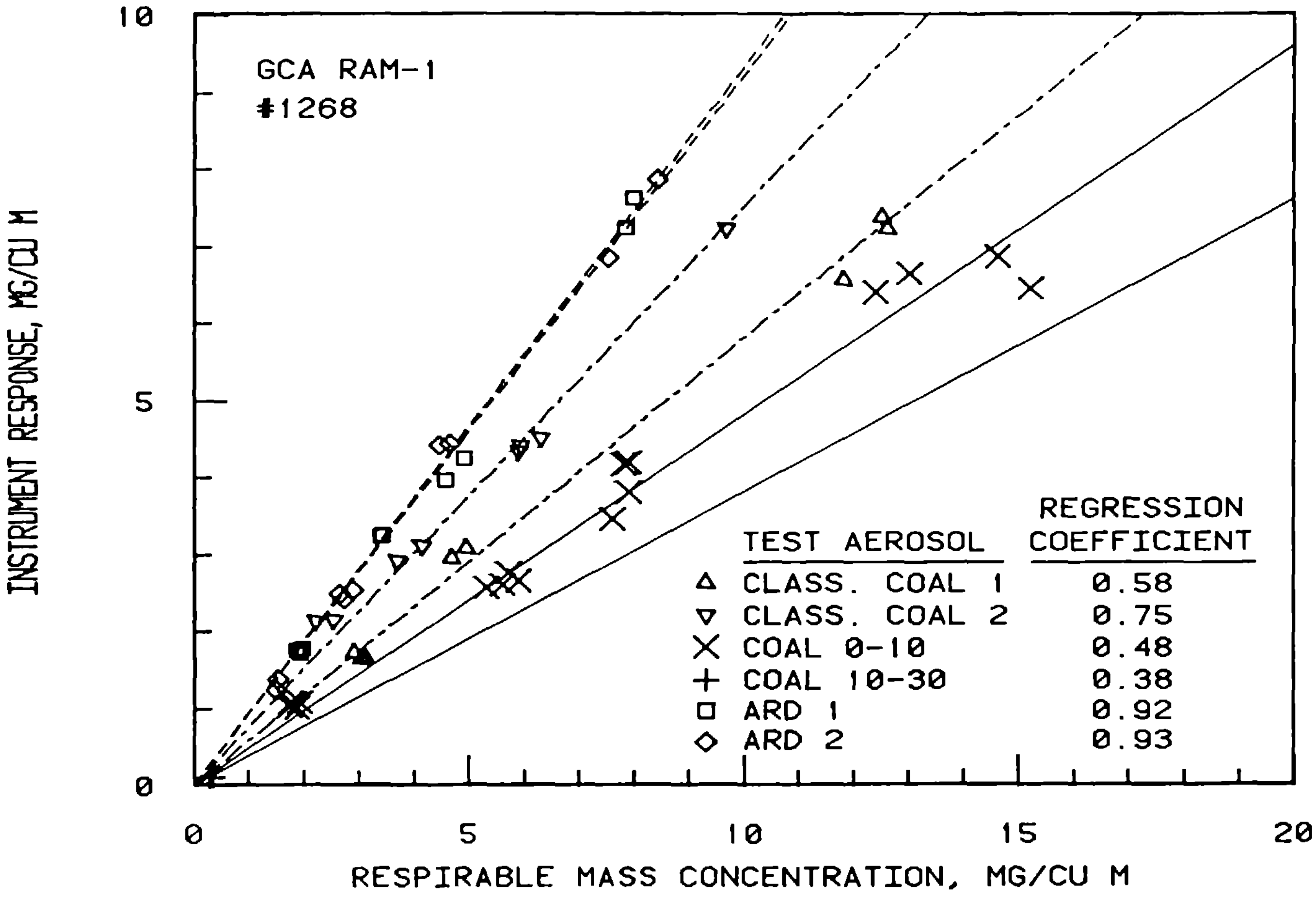

Figure 4.4. Calibration data for GCA RAM-1 serial number 1268.

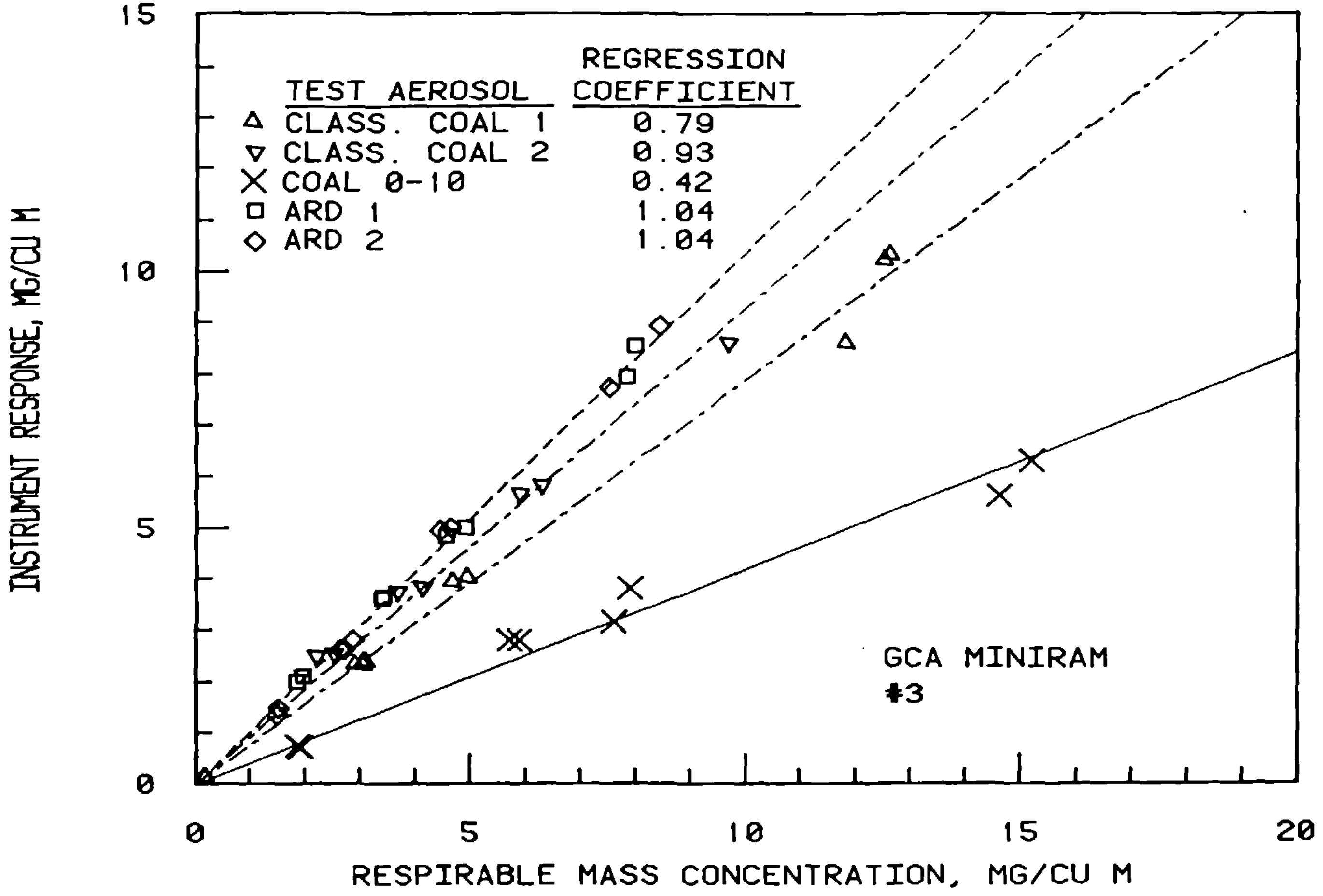

Figure 4.5. Calibration data for GCA MINIRAM serial number 3.

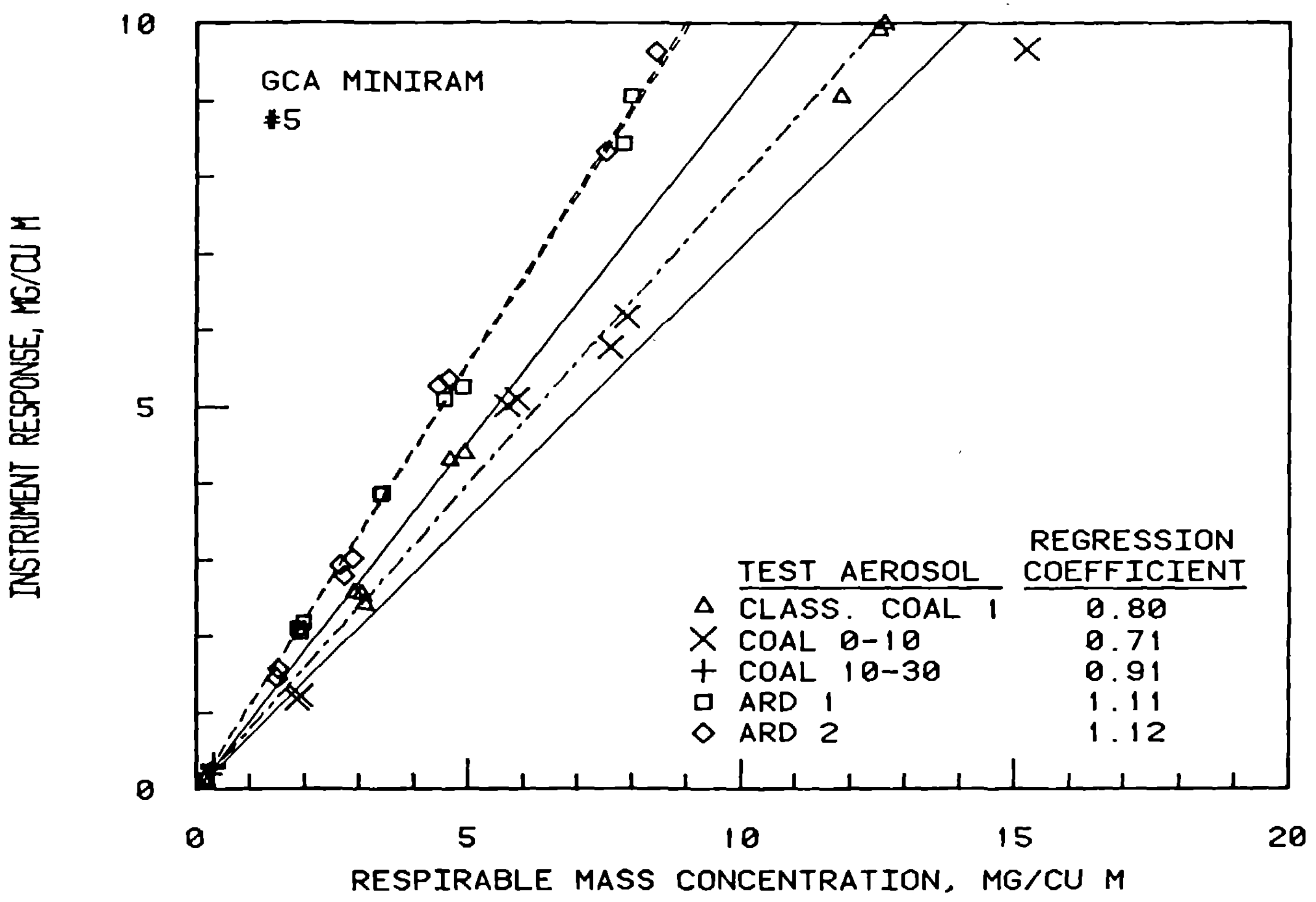

Figure 4.6. Calibration data for GCA MINIRAM serial number 5.

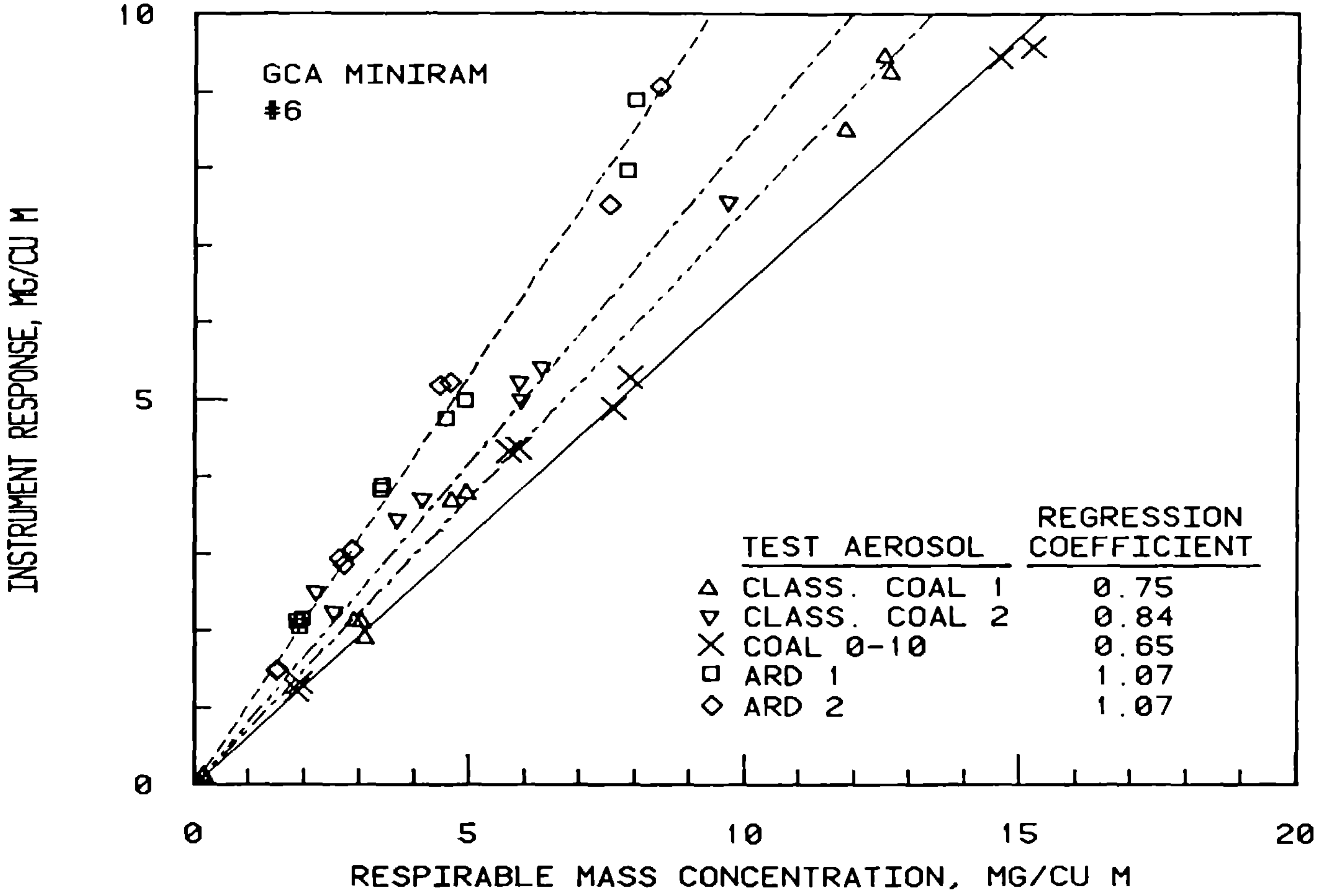

Figure 4.7. Calibration data for GCA MINIRAM serial number 6.

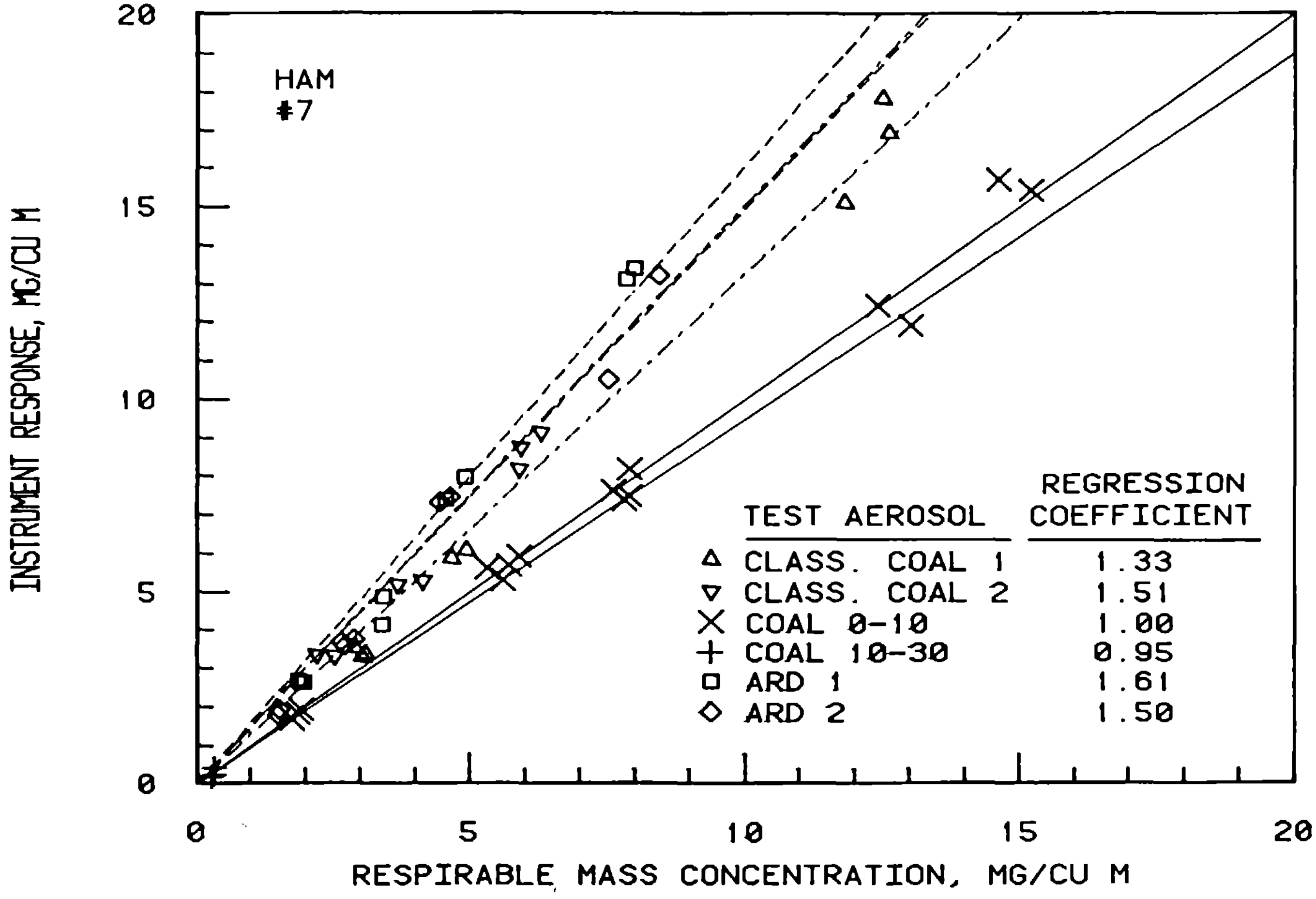

Figure 4.8. Calibration data for ppm HAM serial number 7.

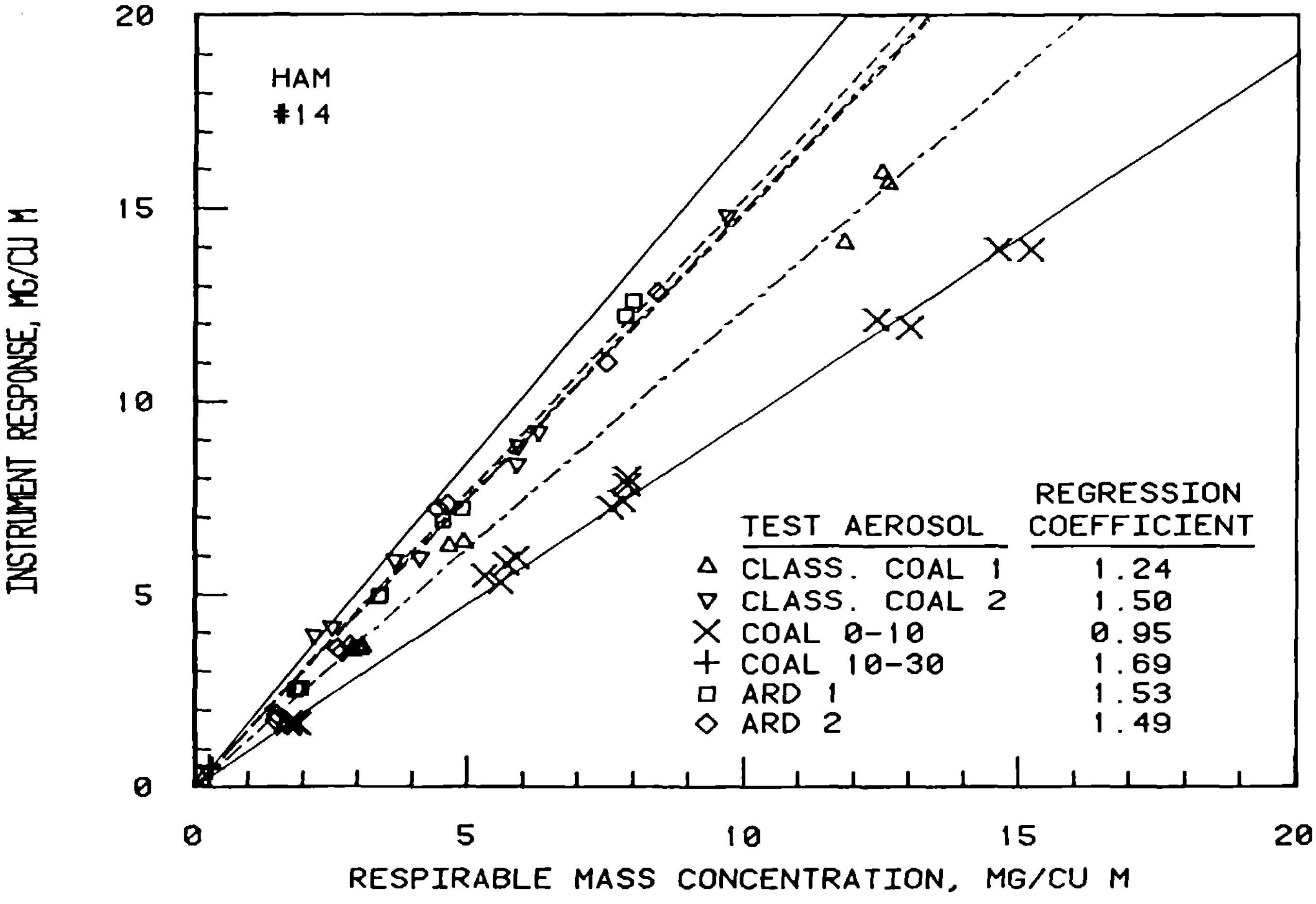

Figure 4.9. Calibration data for ppm HAM serial number 14.

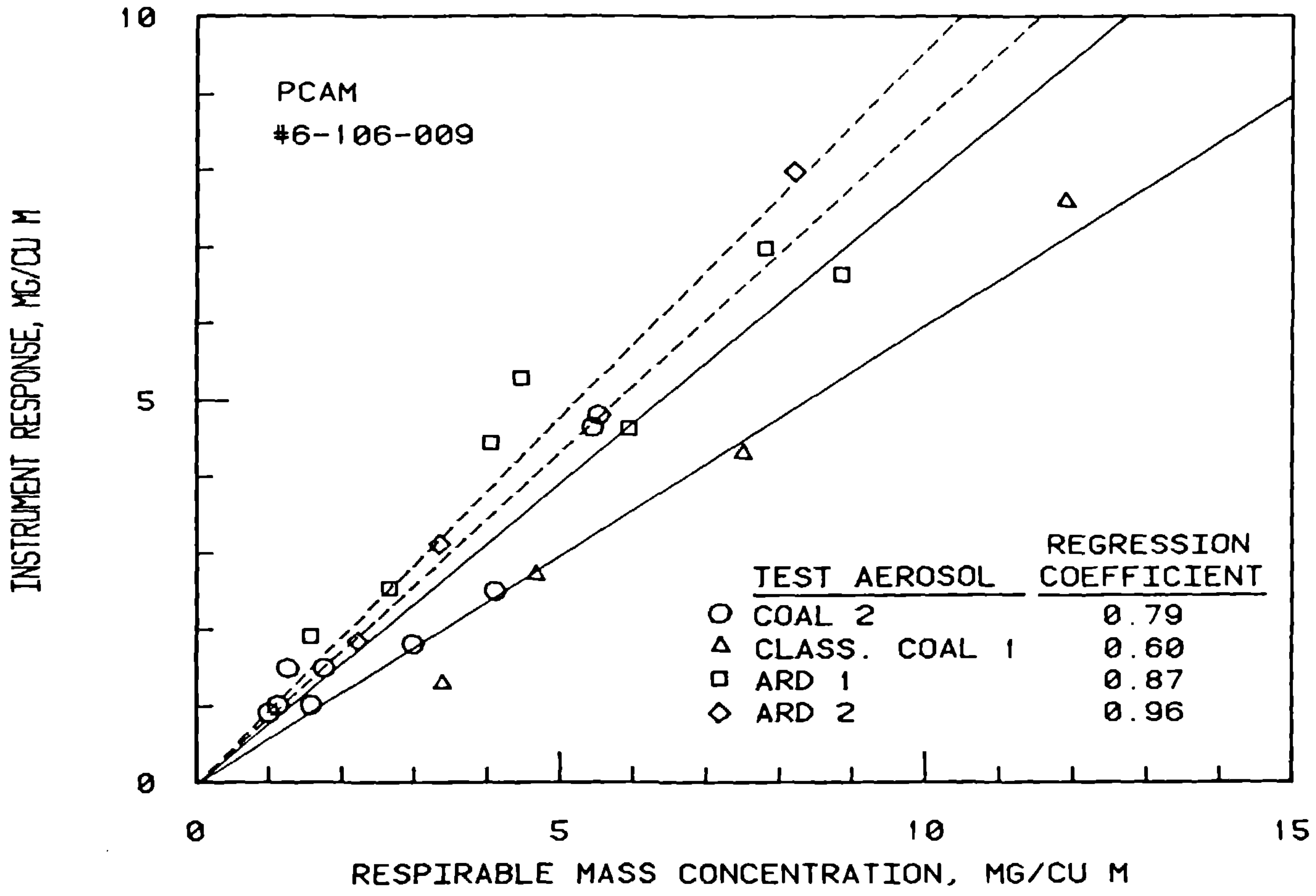

Figure 4.10. Calibration data for ppm PCAM serial number 6-106-009.

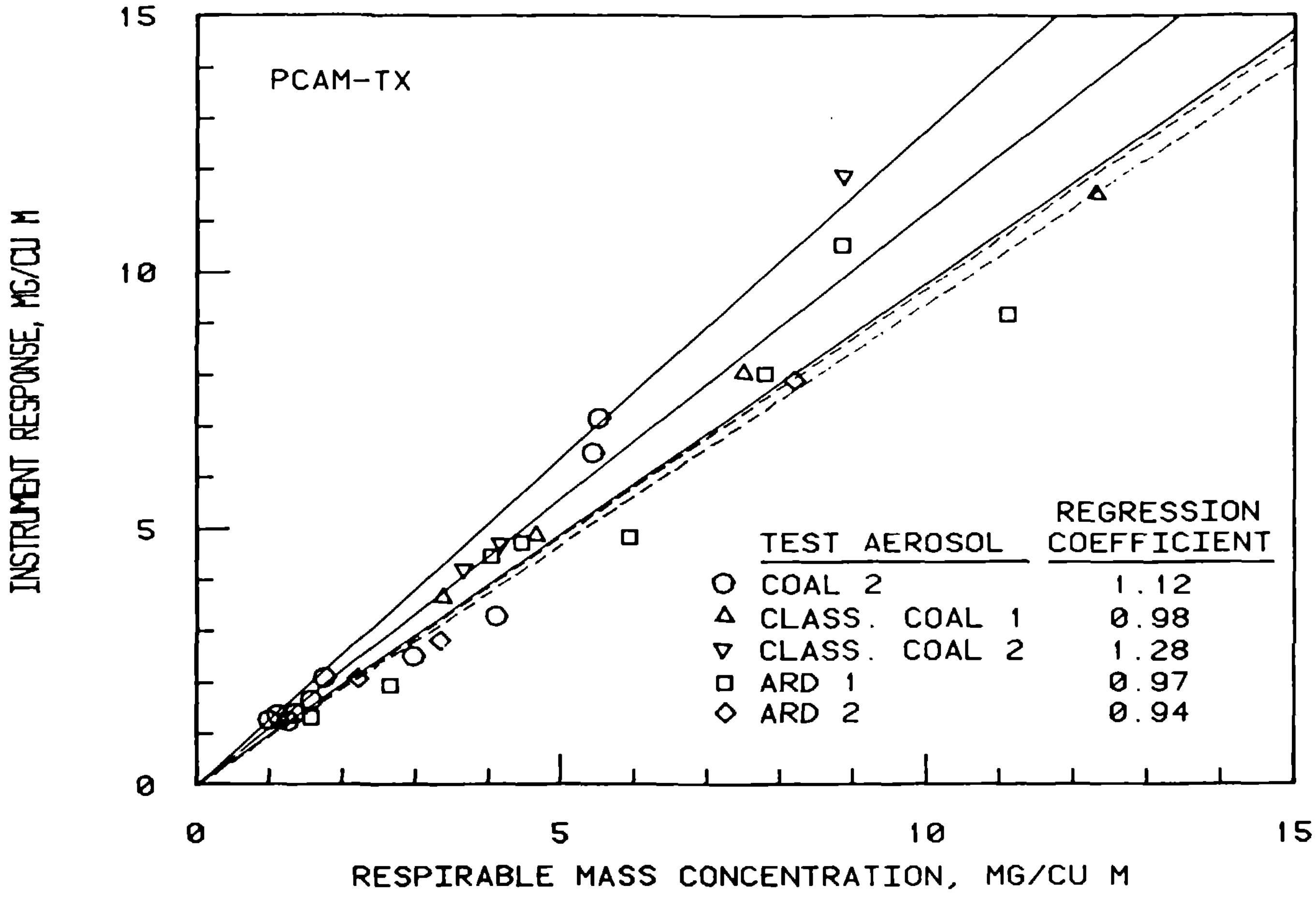

Figure 4.11. Calibration data for ppm PCAM-TX.

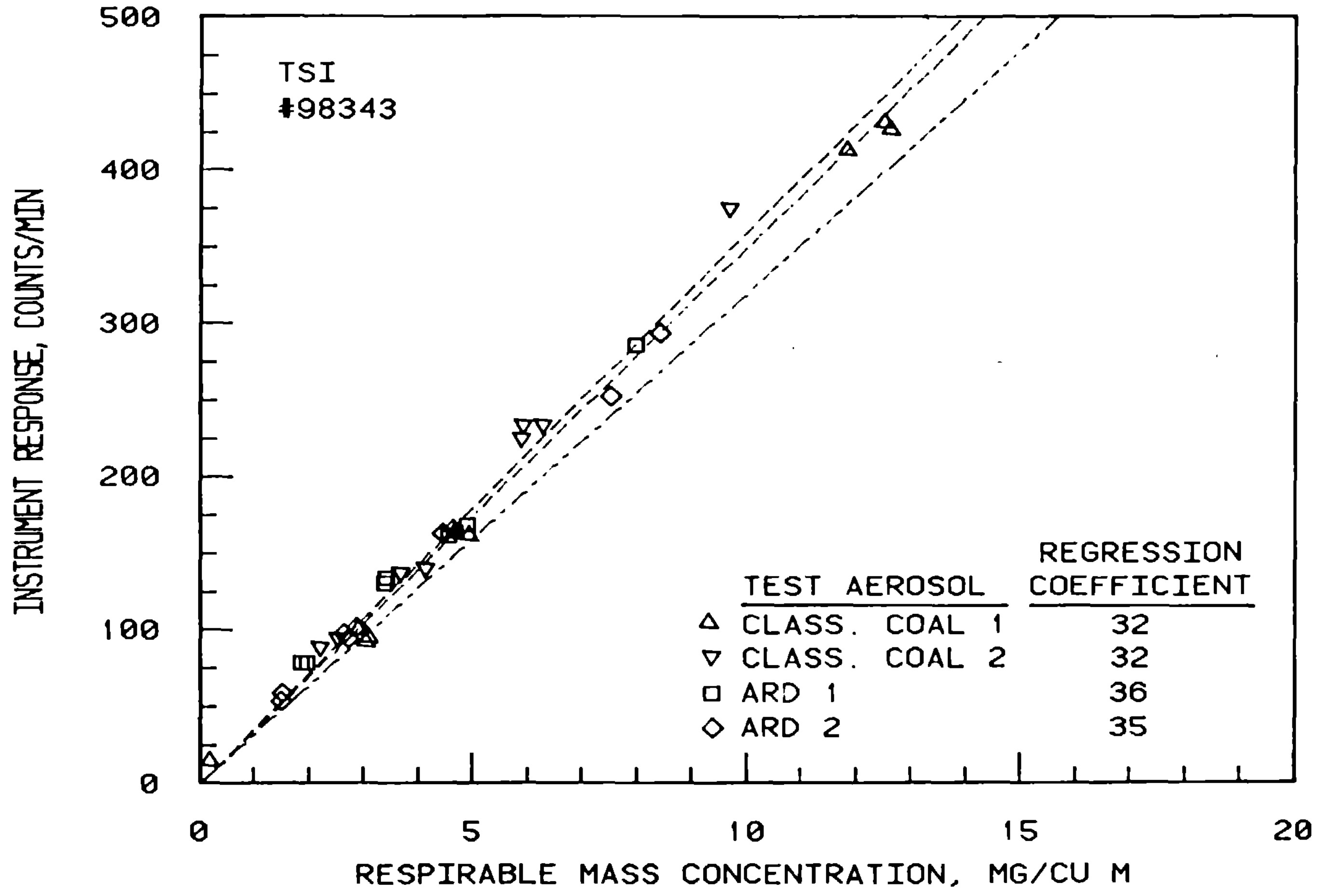

Figure 4.12. Calibration data for TSI Respirable Aerosol Photometer serial number 98343.

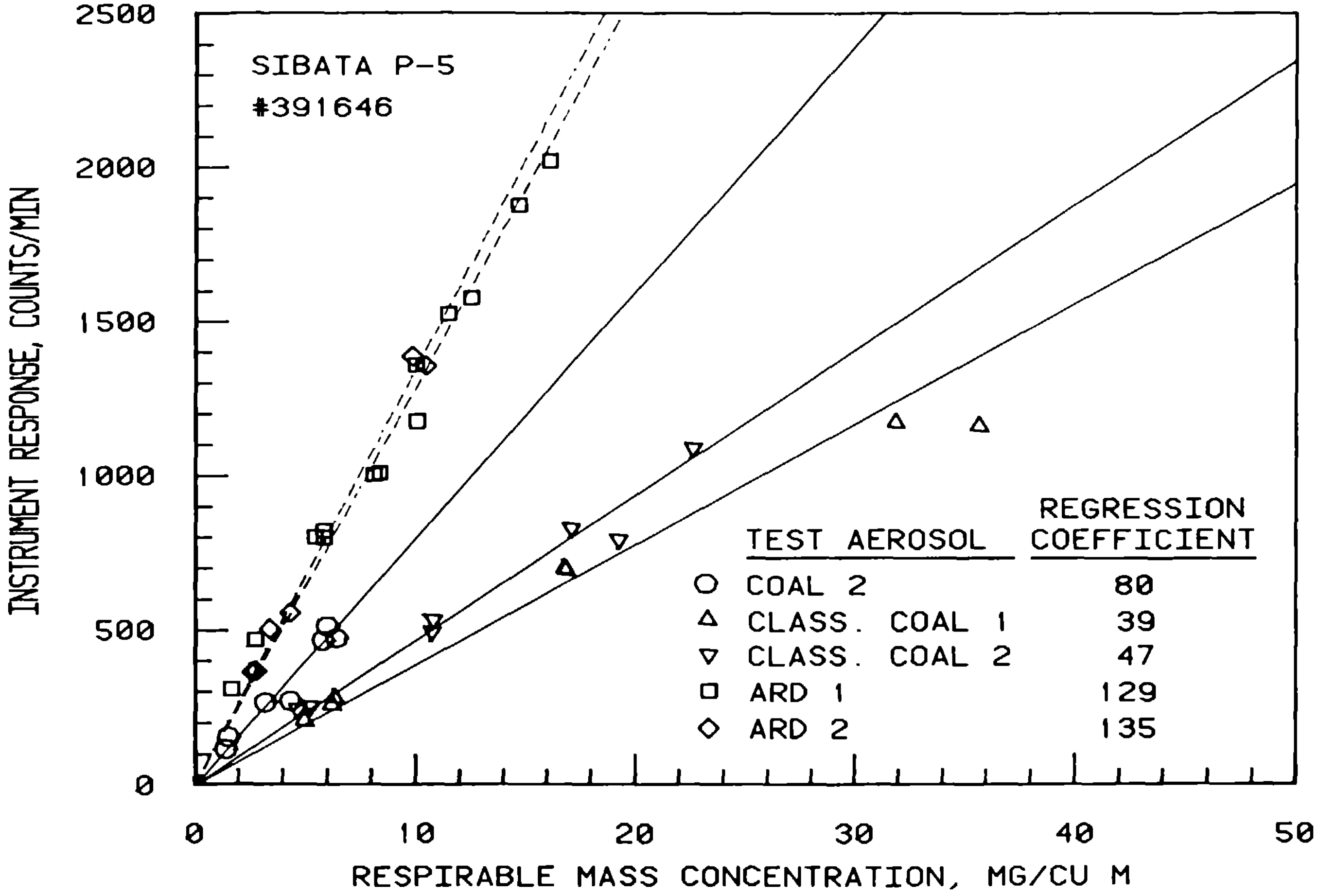

Figure 4.13. Calibration data for Sibata P-5 serial number 391646.

Table 4.5
Regression Coefficients for Photometer Response Calibration Curves

Instrument	Regression Coefficient for						
	Coal-II	Classified Coal-I	Classified Coal-II	Coal: 0-10	Coal: 10-30	ARD-I	ARD-II
GCA RAM-1:							
1263	1.17	0.82	1.03	0.74	0.93	1.14	1.14
1268	0.81	0.58	0.75	0.48	0.38	0.92	0.93
Ave.	0.98	0.70	0.89	0.61	0.66	1.03	1.04
GCA MINIRAM:							
3	-	0.79	0.93	0.42	-	1.04	1.04
5	-	0.80	-	0.71	0.91	1.11	1.12
6	-	0.75	0.84	0.65	-	1.07	1.07
Ave.	-	0.78	0.89	0.59	0.91	1.07	1.08
3[1]	-	-	-	0.29	-	-	-
5[1]	-	-	-	0.54	-	-	-
6[1]	-	-	-	0.45	-	-	-
Ave.	-	-	-	0.43	-	-	-
ppm HAM:							
007	-	1.33	1.51	1.00	0.95	1.61	1.50
014	-	1.24	1.50	0.95	1.69	1.53	1.49
Ave.	-	1.28	1.50	0.98	1.32	1.57	1.50
ppm PCAM	0.79	0.60	-	-	-	0.87	0.96
ppm PCAM-TX	1.12	0.98	1.28	-	-	0.97	0.94
Sibata P-5	80	39	47	-	-	129	135
TSI 5150	37	32	32	-	-	36	35

[1] GCA MINIRAM operated in active sampling mode using cyclone sampler.

Another method of correlating the responses between photometers of the same type is through the use of scatter plots. This type of analysis is straightforward since all photometers were simultaneously exposed to the same test aerosol. To illustrate this correlation, scatter plots of the response obtained from two GCA MINIRAM's, two GCA RAM-1's and two ppm HAM's are presented in Figures 4.14 to 4.16. This data show good correlation between each photometer as a function of instrument response regardless of the test aerosols.

The comparison of the regression coefficients obtained for each test aerosol provides a relative measure of the effect of the aerosol properties, such as material composition and particle size distribution, on the response of the instrument. The relative response of each type of photometer to the different test aerosols is presented in Table 4.6. The data for each photometer has been normalized by the response obtained for the Classified Coal-I aerosol. The mass median diameter and respirable fraction of each test aerosol is also listed.

The relative regression coefficients in Table 4.6 show that all photometers, except the ppm PCAM-TX, have higher responses to Arizona road dust than to coal dust. The relative responses for the GCA RAM-1 and MINIRAM are typical 48 and 38% higher, the ppm HAM and PCAM are 20 and 52% higher, Sibata P-5 is 237% and the TSI is 12% higher.

The data in Table 4.6 also show that the response of these photometers is particle size dependent. The relative response would be 1 among dusts of the same type if the response did not depend on particle size. The results show that the effect of smaller test aerosols is to increase the relative response of the instrument. These results were observed with both the coal and ARD aerosols. For example, the relative response of the GCA RAM-1 increases from 0.87 to 1.27 to 1.40 for the Coal:0-10, Classified Coal-II and Coal-II aerosols. The MMD of these aerosols are 5.0, 2.7 and 2.0 μm, respectively. The MMD of the Classified Coal-I is 3.3 μm. These results are expected since the quantity of scattered light per unit mass of particles increases with decreasing particle size for particles greater than approximately 0.3 μm diameter.

Of special concern for both the GCA MINIRAM and the ppm HAM was the effect of the nonrespirable particle on the instrument response. Neither of these photometers use particle preseparators to remove the large nonrespirable portion of the test aerosol. Consequently, this portion of the aerosol is allowed to pass through the aerosol sensing region of the photometer. The total aerosol mass concentration, which would have been in the aerosol sensing region of these photometers, is listed in Table 4.4 for each test. The respirable fraction of each test dust was obtained by averaging the ratio of the respirable mass concentration for each test. These two mass concentrations are listed for each test in Table 4.4. The respirable fraction, as presented in Table 4.6, range from 0.93 to 0.016.

One way to investigate the sensitivity of the MINIRAM and HAM responses to nonrespirable particles is to compare the relative response of these two instruments, along with the RAM instrument, to changes in the particle size and respirable fraction of the test aerosol. The RAM is used because it has a preclassifier to remove the nonspirable particles before they reach the sensing region. The relative response to all three photometers are very similar for Classified Coal-I and -II, and Coal:0-10. In particular, when changing from

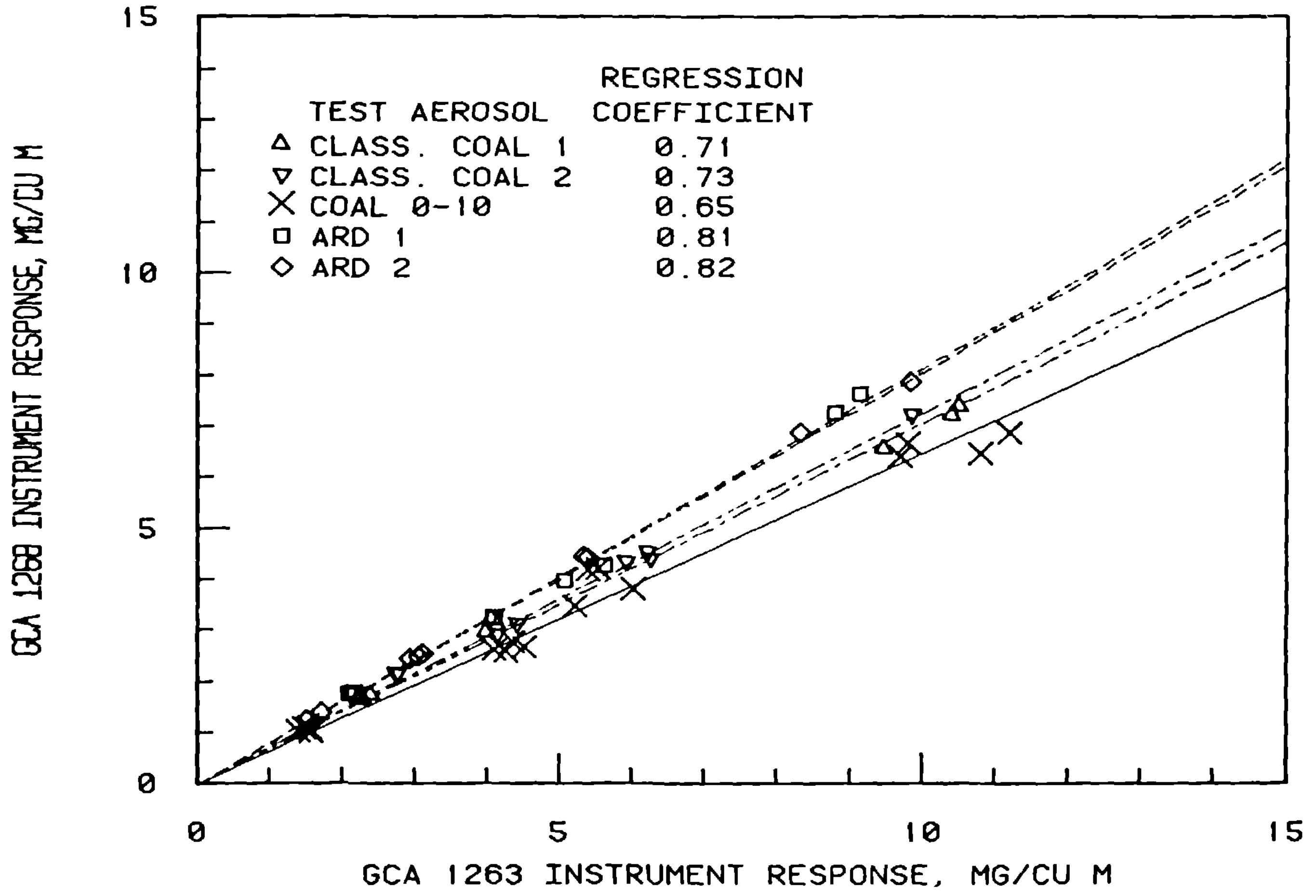

Figure 4.14. Response comparison between 2 GCA RAM-1 photometers.

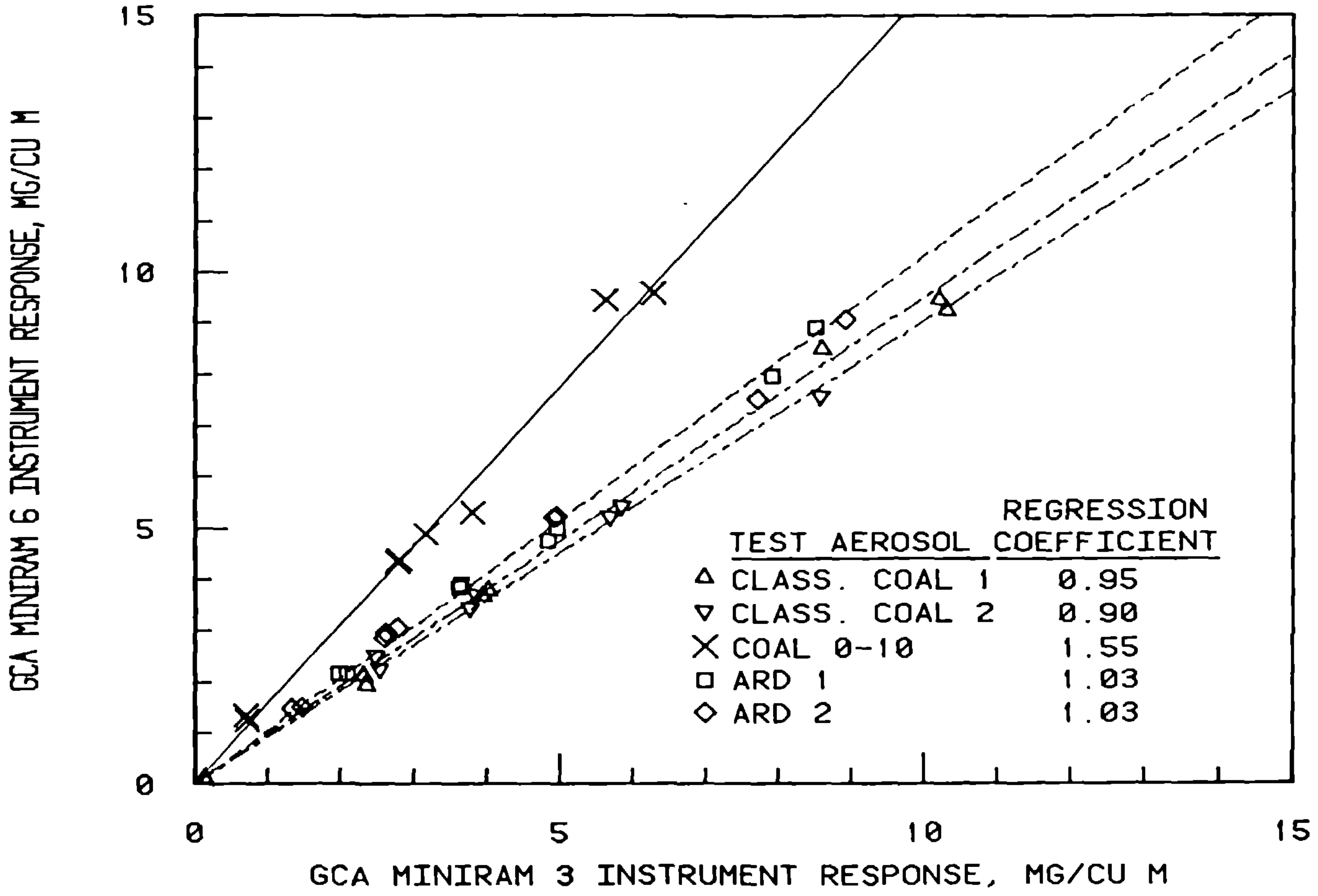

Figure 4.15. Response comparison between 2 GCA MINRAM photometers.

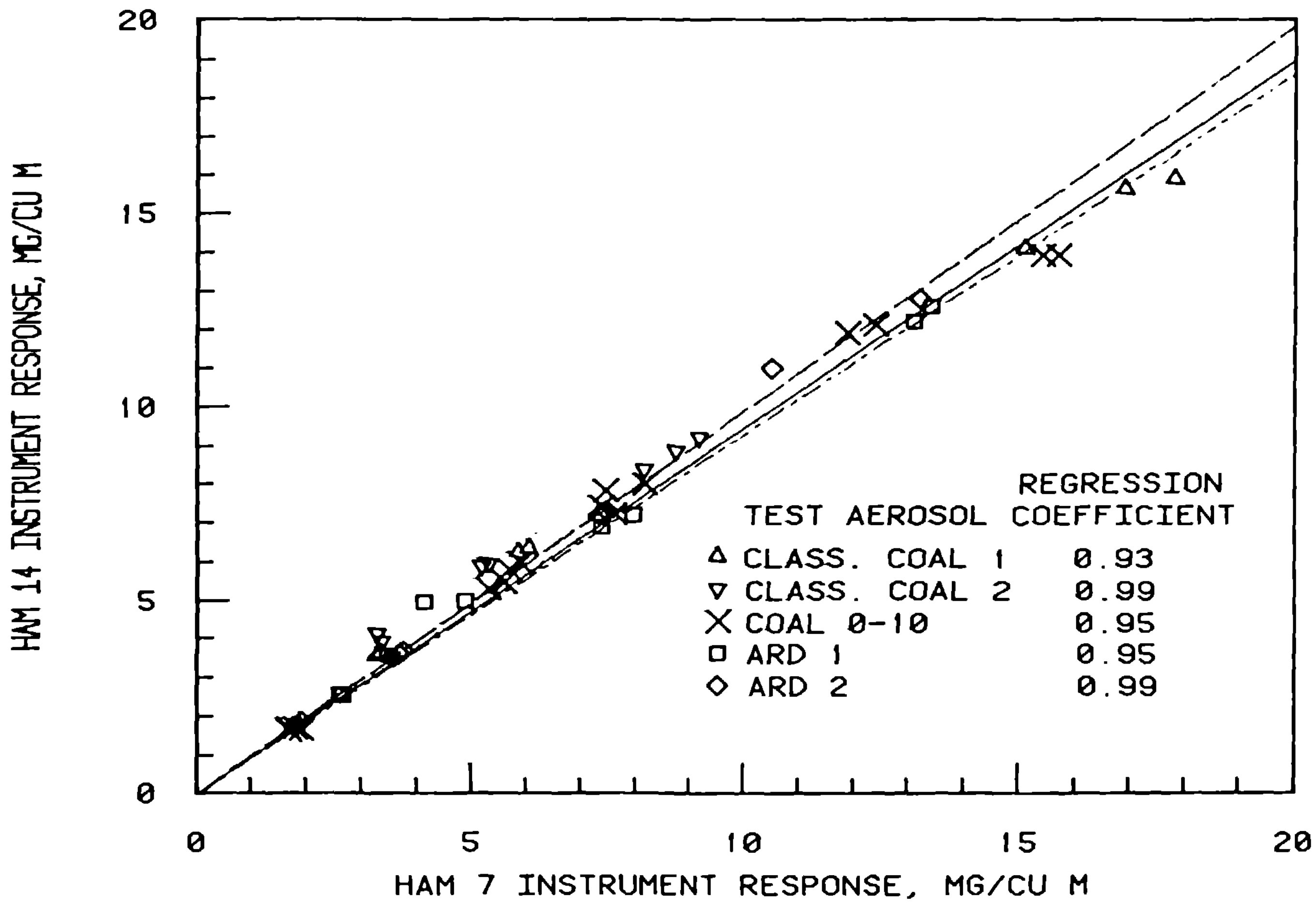

Figure 4.16. Response comparison between 2 ppm HAM photometers.

Table 4.6
Relative Photometer Response as a Function of Aerosol

Dust	Respirable fraction[1]	MMD, µm	Relative Photometer Response[2,3] GCA RAM-1	GCA MINIRAM	ppm HAM	ppm PCAM	ppm PCAM-TX	Sibata P-5	TSI 5150
ARD-II	0.93	1.6	1.49	1.38	1.17	1.60	0.96	3.46	1.09
ARD-I	0.73	3.8	1.47	1.37	1.23	1.45	0.99	3.31	1.13
COAL-II	0.74	2.0	1.40	----	----	1.32	1.14	2.05	1.16
CLASSIFIED COAL-II	0.72	2.7	1.27	1.14	1.17	----	1.31	1.21	1.00
CLASSIFIED COAL-I	0.56	3.3	1.00	1.00	1.00	1.00	1.00	1.00	1.00
COAL: 0-10	0.31	5.0	0.87	0.76	0.77	----	----	----	----
COAL: 10-30	0.016	14.0	0.94	1.17	1.03	----	----	----	----

[1] Ratio of respirable mass concentration based on ACGIH criteria to total mass concentration.
[2] Normalized by response obtained for Classified Coal-I aerosol.
[3] Analysis based on average regression coefficient data presented in Table 4.5.

Classified Coal-II to Coal:0-10 the relative response of the RAM-1 decreases from 1.27 to 0.87. For the same conditions, the MINIRAM and HAM decrease from 1.14 to 0.76 and 1.17 to 0.77 respectively. The relative response for each instrument decrease by about 40%. This decrease is due to the increase in particle size as was discussed earlier. More importantly, the change in relative response was the same for all photometers even through the quantity of nonrespirable particles increased from 28 to 69% of the total aerosol. When going from Coal:0-10 to :10-30, the relative response of the RAM increases from 0.87 to 0.94 while the relative response of the MINIRAM and HAM increases from 0.76 to 1.17 and 0.77 to 1.03 respectively. These latter two are increases of 54 and 34%. These increases indicate that that is a response to nonrespirable particles. However, these increases are 2.5% or less of the 20 fold increase in the nonrespirable fraction of the coal dust. Thus, one can conclude that the MINIRAM and HAM respond to nonrespirable particles, but the response can be considered negligible when compared to the degree of response to particles in the respirable size range.

A special series of tests was performed with the GCA MINIRAM's to determine the effect of sampling in the active mode, as opposed to the passive mode, on the response characteristics. In the active sampling mode a 10 mm diameter nylon cyclone and adapter were installed on the MINIRAM and the aerosol sampled at a flow rate of 2.0 L/min. The tests were performed with the Coal:0-10 aerosol. The data obtained for both passive and active sampling are presented in Table 4.4 and Figures 4.17 to 4.19. The regression coefficients obtained from linear regression analysis are presented in Table 4.5 The response of the MINIRAM when operated in the active mode was found to be a linear function of mass concentration; however, the response was typically 27% less than that observed when the units were operated in the passive sampling mode. This decrease results from the collection of particle in the respirable size range in the cyclone. The effect of operating the MINIRAM with the cyclone is to monitor the respirable fraction of the respirable fraction of the sampled aerosol. This occurs because only the respirable fraction pass through the cyclone and then the MINIRAM optically senses the respirable fraction of the remaining aerosol.

A special series of tests was also performed with the GCA RAM-1 to determine the effect of sample flow rate on response. The RAM-1 is equipped with the 10 mm nylon cyclone used as the particle preseparator. While the light scattering and sensing characteristics of the RAM-1 are independent of sample flow, the degree of particle deposition in the cyclone is flow rate dependent. Two RAM-1s were used in this study. The first, which was operated only at a sample flow rate of 2.0 L/min, was used to monitor the aerosol concentration in the test chamber. The sample flow rates of 1.7, 1.8 and 2.0 L/min were used with the second unit. The results, given in Table 4.7, are normalized by the response of the RAM-1 obtained at a flow rate of 2.0 L/min. The aerosol concentration was held constant during these tests. These tests were conducted with four different test aerosols. The response of the RAM-1 at a flow rate of 1.8 L/min was found to be from 17% to 24% greater than that obtained at a flow rate of 2.0 L/min. The response at a flow rate of 1.7 L/min was from 23% to 32% greater than that obtained at a flow rate of 2.0 L/min. The higher response was expected since the fraction of particles, which pass through the cyclone, increases with decreasing flow rate. All of the data presented in Tables 4.2 to 4.4 were obtained using a sample flow rate of 2 L/min.

Table 4.7

Effect of Sample Flow Rate

on GCA RAM-1 Response

Material	Normalized Response[1] at Sample Flow Rate L/min of	
	1.7	1.8
Classified Coal-I	1.31	1.22
Classified Coal-II	1.32	1.24
ARD-I	1.25	1.17
ARD-II	1.23	1.20

[1] Normalized by response obtained at sample flow rate of 2.0 L/min

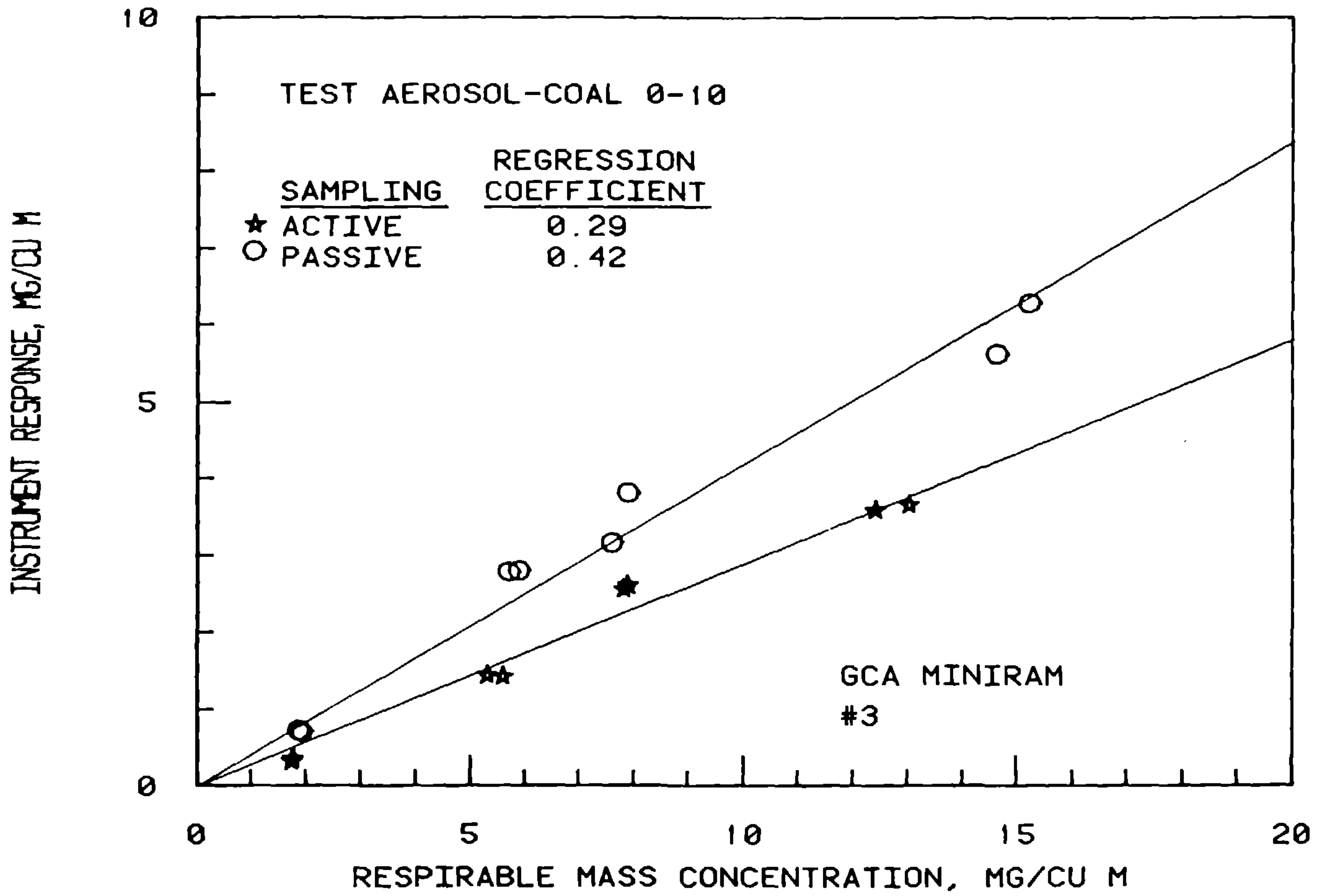

Figure 4.17. Effect of active versus passive sampling on the response of GCA MINIRAM serial number 3.

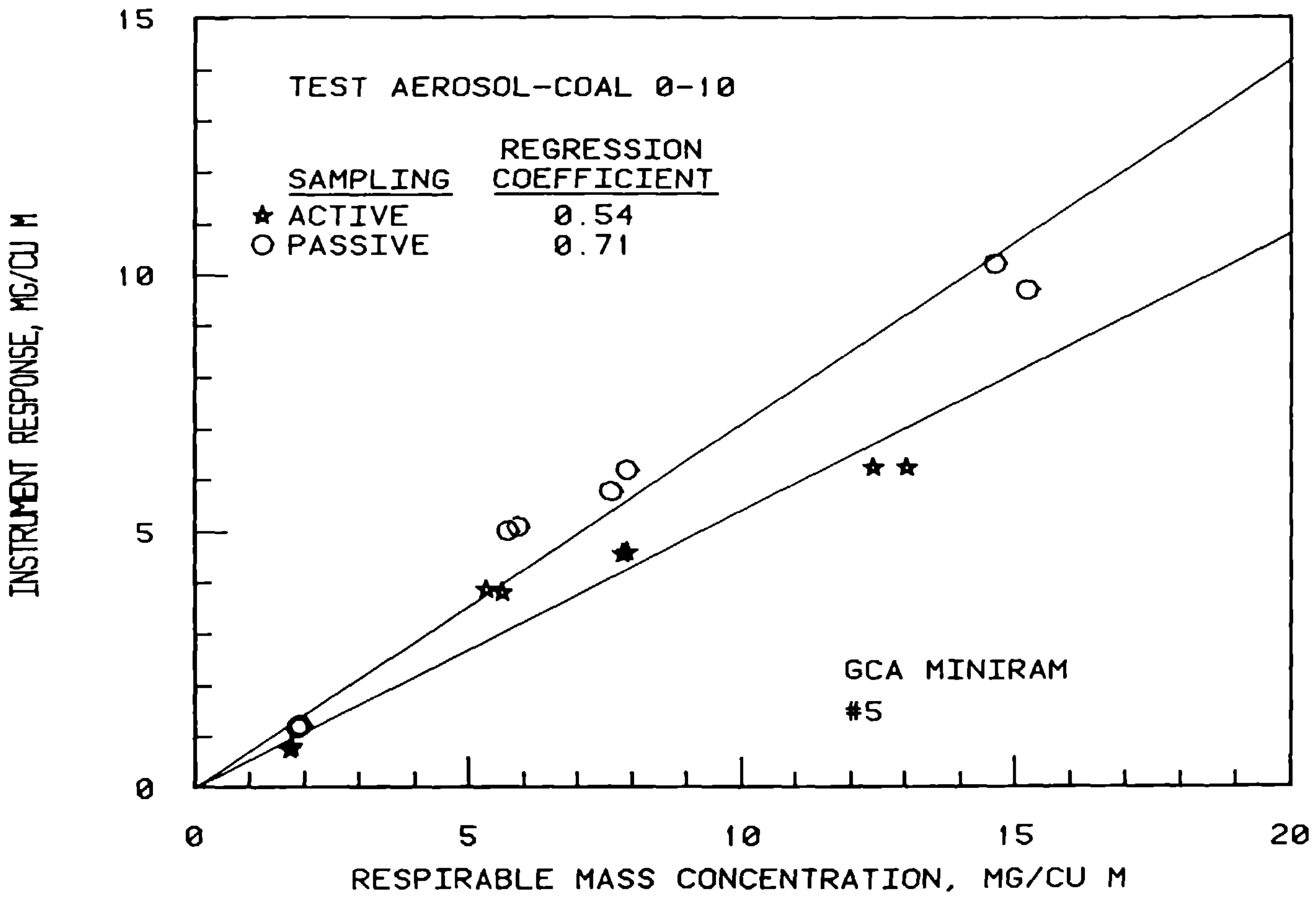

Figure 4.18. Effect of active versus passive sampling on the response of GCA MINIRAM serial number 5.

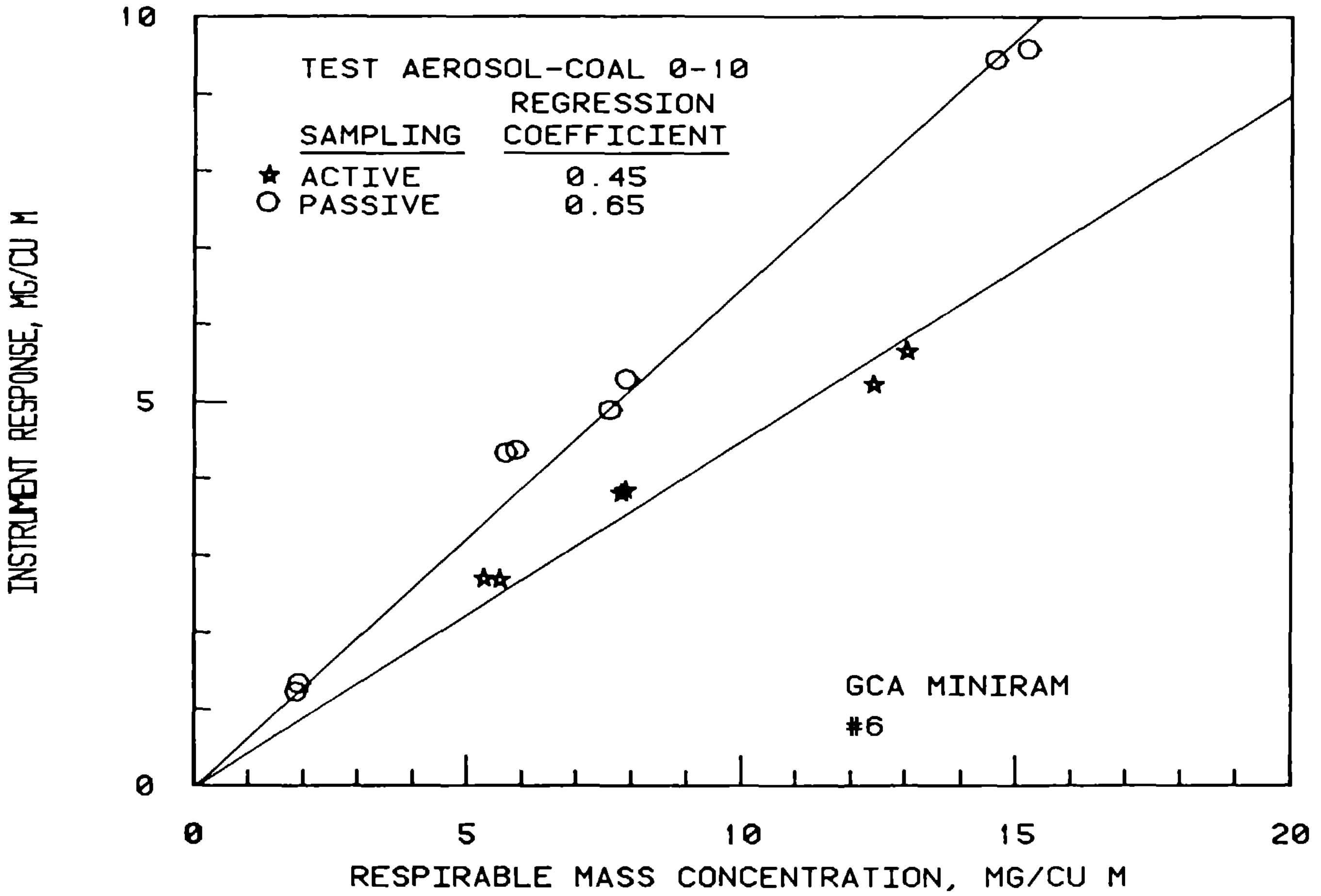

Figure 4.19. Effect of active versus passive sampling on the response of GCA MINIRAM serial number 6.

4.4 Liquid Droplet Study

The objective of this study was to determine how the GCA RAM-1 responds to water droplets in the respirable particle size range. Since water droplets easily change size due to evaporation, and thus could not conveniently be used for experimentation, it was necessary to attack the problem in two steps. First, a relationship was developed between the instrument response predicted theoretically and that measured experimentally for oleic acid droplets which do not evaporate and are stable. Second, by assuming this relationship is similar for both oleic acid and water droplets, the relationship was used to infer the response of the RAM-1 to water droplets from the results of the theoretical study on water drops.

4.4.1 Theoretical Study

The scattering intensity of infrared radiation from particles in the view volume of the RAM-1 was theoretically predicted from algorithms based on Mie scattering theory. The particular algorithms used were those developed by Dave (14,15). The quantity of scattered radiation in a given direction from a particle is a function of the particle size, shape and index of refraction and the wavelength of the incident radiation. A wavelength of 940 nm was used, since this is the mean wavelength of the RAM-1 light emitting diode. The scattering intensity was computed over the scattering angles of 45 to 95°. The particles were assumed to be spherical. The index of refraction for oleic acid and water (16) were taken to be 1.44 + i0 and 1.328 + i0.000023 respectively.

4.4.2 Experimental Study

The experimental study consisted of simultaneously determining the mass concentration of a monodisperse test aerosol by means of the RAM-1 measurement and gravimetric analysis. The test setup, schematically shown in Figure 4.20, consisted of an aerosol generator, transport tube, test chamber, RAM-1, and two filter samplers associated with flow meters and pumps. The test aerosols of oleic acid were generated by a TSI Model 3050 vibrating orifice monodisperse aerosol generator (VOMA) (TSI, Inc. St. Paul, MN), charge neutralized by a Kr-85 neutralizer, and continuously injected into a 0.22 m^3 chamber at a flow rate of 80 L/min. The two filter samplers and the RAM-1 were arranged symetrically about the center of the chamber. Unsampled aerosol particles passed though a baffle and into a HEPA filter.

The RAM-1 was operated with the optional inlet instead of the 10 mm cyclone so the response of the RAM-1 could be directly compared to the gravimetrically determined mass concentration. The filter samplers were open-faced 37 mm filter cassettes. The flow rate through each filter sampler, which was 10 L/min, was continuously monitored by a TSI Model 2012 mass flow meter (TSI, Inc. St. Paul, MN). Millipore Type AA (0.8 μm pore size membrane filter (Millipore Corp. Bedford, MA) were used in the filter cassettes to collect the aerosol particles. The particle collection efficiency of these filters was greater than 99.99% (17).

For this study, two upward-facing open 37 mm filter cassettes to be used as standards were placed within the chamber along with the RAM-1. The particle sampling efficiencies of these cassettes and the RAM-1 inlet were determined to

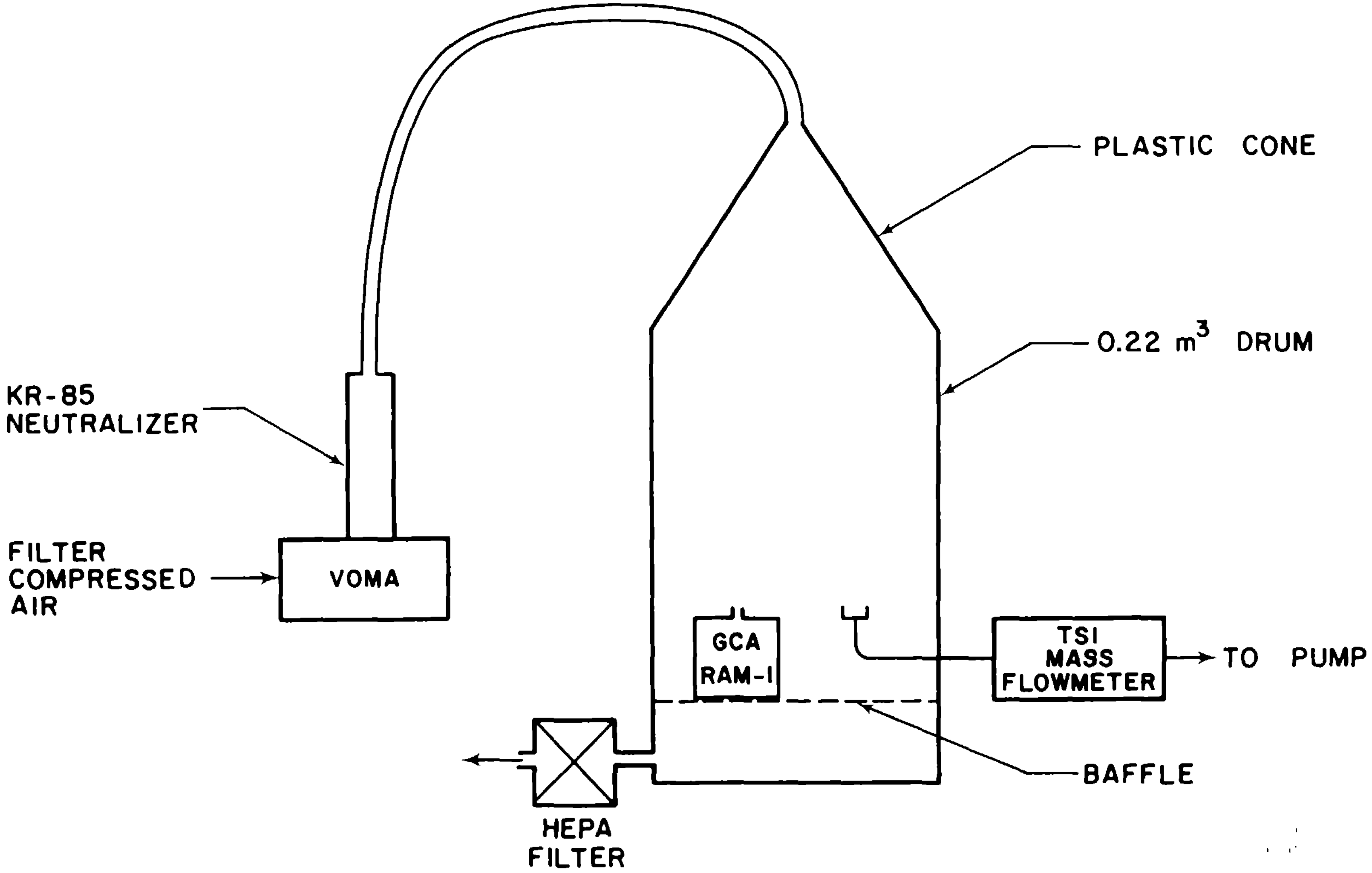

Figure 4.20. Schematic diagram of the test setup used to determine the "mass sensitivity" of the GCA RAM-1 to oleic acid droplets.

be nearly 100% over the particle size range used in this study by applying the theory of Agarwal and Liu (18). This theory applies to inlets sampling from quiescent air and includes the effects of gravity and particle inertia.

4.4.3 Test Results

In this study the experimental data and theoretical results are presented in terms of the RAM-1 "mass sensitivity" defined as the ratio of the RAM-1 indicated mass concentration to the actual aerosol mass concentration. This mass sensitivity is independent of mass concentration since the calibration data presented in Section 4.3 shows that the response of the RAM-1 is linearly proportional to the actual mass concentration. The proportionality factor is the mass sensitivity.

The experimentally determined RAM-1 mass sensitivity data for monodisperse oleic acid particles are presented in Table 4.8 and Figure 4.21 as a function of particle size. The data show that the mass sensitivity decreases monotonically with increasing particle size from 1.16 at 2 µm diameter to 0.095 at 10 µm. For example, the mass sensitivity of 0.095 indicates that the RAM-1 measured mass concentration was only 9.5% of the gravimetrically determined value.

The theoretically predicted RAM-1 mass sensitivity is presented in Figure 4.21 for both oleic acid and water droplets. These mass sensitivities were determined by multiplying the theoretically predicted radiation scattering intensity per unit particle mass by an "instrument response factor".

The "instrument response factor" is defined as the ratio of the experimentally determined mass sensitivity of the RAM-1 to the theoretically predicted radiation scattering intensity per unit particle mass. This factor accounts for the actual volume of the viewing volume in the RAM-1, the intensity of the radiation emitted by the diode, the electronic gain in the RAM-1 circuitry and particle loss in the passageways from the inlet to the viewing volume. Assuming that the theory correctly predicts the radiation scattering in the RAM-1, the "response factor" is only a scaling factor which is independent of particle size or index of refraction. Thus, this factor, once obtained for oleic acid, can be applied to the theoretically predicted radiation scattering data for the water droplets to predict the mass sensitivity of the RAM-1 to water droplets.

The theoretically predicted mass sensitivity for oleic acid and water droplets are presented in Figure 4.21 as a function of Stokes particle diameter. For spherical particles the Stokes diameter is equivalent to the physical diameter of the droplet. The data show that the mass sensitivity curves for both liquids exhibit a maximum in the vicinity of 0.6 µm diameter. The maximum mass sensitivity is 3.9 for oleic acid and 1.75 for water. From this maximum, the mass sensitivities monotonically decrease with increasing particle size. The mass sensitivity equals 1, which means that the RAM-1 indicated mass concentration is equivalent to the actual mass concentration, for a 2.2 µm diameter oleic acid droplet and a 1.1. µm diameter water droplet. For particles greater than 1 µm, the RAM-1 sensitivity for water is 10 to 30% less than that found for oleic acid.

Typical values of the RAM-1 mass sensitivity to water droplets in the respirable size range are presented in Table 4.9. Data are presented for the

Table 4.8

Experimentally Determined "Mass Sensitivity" of GCA RAM-1 to Oleic Acid Droplets as a Function of Particle Diameter

Stokes Particle Diameter, μm	Mass Sensitivity[1,2]
2.00	1.16
3.16	0.55
3.50	0.51
3.98	0.38
5.03	0.24
7.24	0.16
8.90	0.115
10.0	0.095

---

[1] Serial No. 1268

[2] Mass sensitivity = $\frac{\text{instrument reading in}^3\text{mg/m}}{\text{true aerosol mass concentration, mg/m}^3}$

Table 4.9

Theoretically Predicted "Mass Sensitivity" of the GCA RAM-1 to Water Droplets as a Function of Droplet Diameter

	Mass Sensitivity[1]	
Droplet Diameter, μm	Without Cyclone Preclassifier	With Cyclone Preclassifier[2]
2	0.7	0.63
2.5	0.55	0.41
3.5	0.36	0.18
5.0	0.21	0.052
10.0	0.12	0

[1] Mass sensitivity = $\frac{\text{instrument reading in mg/m}^3}{\text{true aerosol mass concentration, mg/m}^3}$

[2] Assuming particle penetration characteristics of the 10 mm cyclone are equivalent to the ACGIH respirable dust criteria.

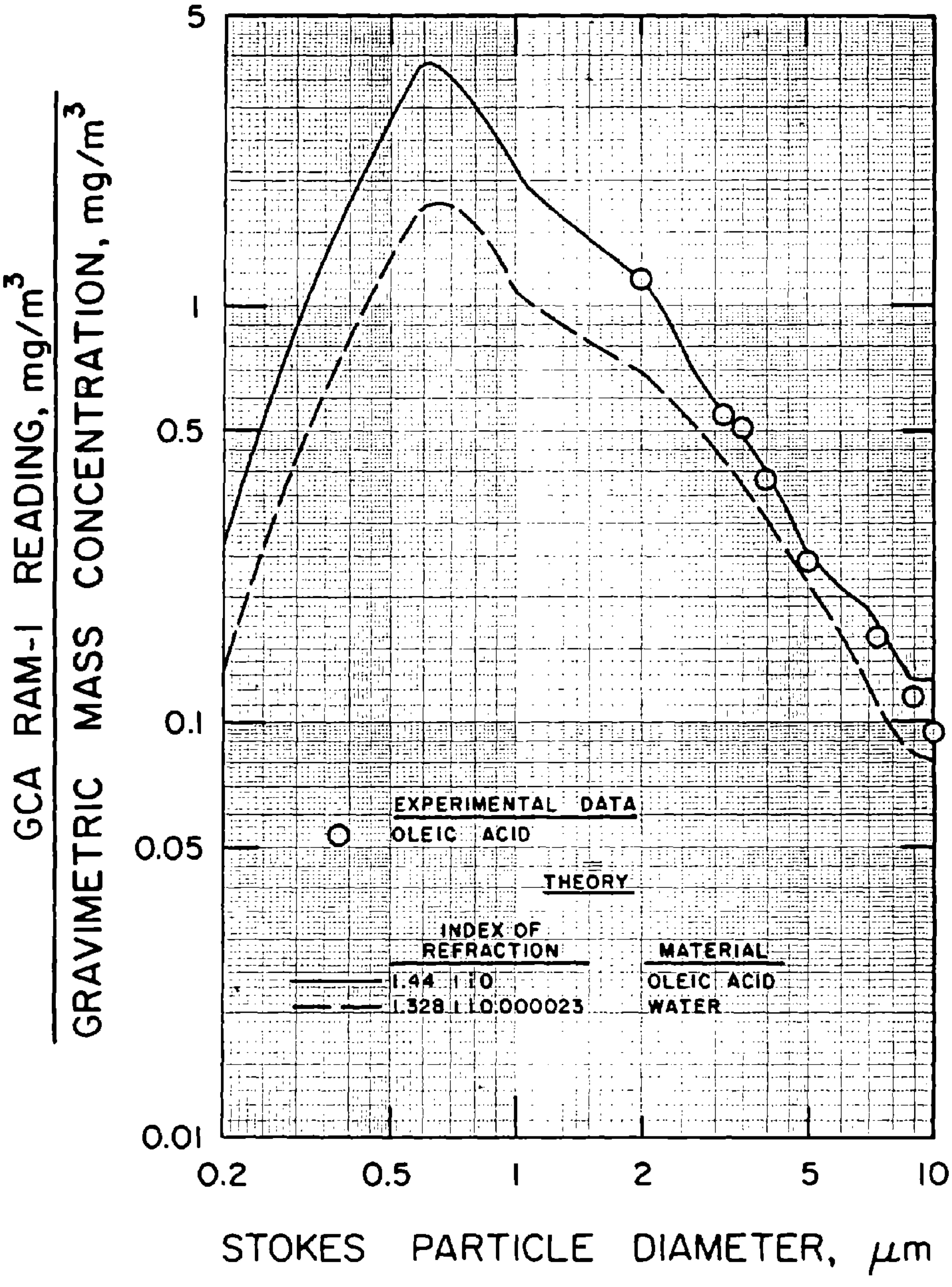

Figure 4.21. Experimentally determined and theoretically predicted "mass sensitivity" of the GCA RAM-1 to oleic acid and water droplets.

response of the RAM-1 when operated with and without the 10 mm Dorr-Oliver cyclone. The particle penetration through the cyclone was assumed to be equivalent to the ACGIH respirable dust criteria. For the case of RAM-1 operation without the cyclone, the data show that the mass sensitivity decreases from 0.7 to 0.12 as the particle diameter increases from 2 to 10 μm. When the cyclone is used, the mass sensitivity decreases from 0.63 to 0 from the same particle size range.

4.5 Summary

The response of a wide variety of commercially available photometers to various test aerosols have been determined. The tests were divided into two sets of experiments. The primary and most extensive work dealt with several dust aerosols. The second set of experiments involved a determination of the mass sensitivity of the GCA RAM-1 to water droplets.

The mass sensing capabilities of 8 photometer models from 5 manufacturers has been determined for dust aerosols which consisted of various dust types, mass concentrations, particle sizes and respirable mass fractions. The test aerosols consisted of five different coal dusts with mass median diameters ranging from 2.0 to 14.0 μm and two Arizona road dust aerosols with mass median diameters of 1.6 and 3.8 μm. The respirable mass concentration of the test aerosol was varied from 0.15 to 18 mg/m^3 with the respirable fraction of the aerosols ranging from 0.93 to 0.016. Test results show that the response of photometers are linerly proportional to the respirable mass concentration, but a calibration should be performed on each photometer to obtain the proportionality constant as this constant ranged from 0.66 to 1.28 of the actual respirable mass concentration. The proportionality constant was greater for Arizona road dust than for coal dust and decreased with increasing particle size. The GCA MINIRAM and ppm HAM photometers primarily respond to the respirable fraction of the test aerosol independent of the nonrespirable amount even though no inertial preseparator are used. Lastly, data were obtained to determine the effect of the GCA RAM-1 operating flow rate and active versus passive sampling with the GCA MINIRAM on the response of these instruments.

The second portion of the photometer studies dealt with determining the mass sensitivity of the GCA RAM-1 to water droplets in the respirable particle size range. This sensitivity was obtained in an indirect manner due to the difficulty of experimentally determining the droplet size of water droplets. The approach involved an experimental and theoretical determination of the mass sensitivity of the RAM to oleic acid droplets. Comparison of the two determinations show that the theory quite accurately predicts the sensitivity as a function of particle size. Based on this comparison, the mass sensitivity of the RAM to water droplets was theoretically established.

The theoretically predicted mass sensitivity for water droplets shows that the RAM-1 will respond to water droplets in the respirable size range. The maximum response, which occurs at 0.6 μm diameter, is 1.75 times the actual mass concentration. For larger droplets, the response monitonically decreases with responses of 70% and 12% occurring for 2 and 10 μm diameter droplets respectively.

No work was performed under this contract to determine the expected size distribution and mass concentration of water droplets which could exist in underground mining environments. However, discussions with several researchers indicate that water droplets in the respirable size range can be found.

CHAPTER 5

10 mm DORR-OLIVER CYCLONE EVALUATION

5.1 Introduction

A brief study conducted by U. S. Bureau of Mines personnel (19) has shown that the respirable mass concentration obtained when using a 10 mm Dorr-Oliver cyclone as a preseparator is affected by the free stream (wind) velocity and cyclone orientation. The tests were performed with free stream velocities varying from 0.43 to 10.2 m/sec (85 - 2,000 ft/min). Free stream velocities in this range could be experienced in underground mining operations. Furthermore, they showed that the placement of a cylindrical shield around the cyclone in the area of the inlet reduced the effects of free stream velocity and cyclone orientation on the cyclone performance.

In another study (20), which dealt strictly with low free stream velocities, no significant differences in the quantity of sampled coal dust were found as a function of sampler orientation or free stream velocity. Free stream velocities ranging from 0.25 to 1.51 m/sec (50 to 300 ft/min) and cyclone orientations of facing the inlet toward, away from, and perpendicular to airflow direction were used in the study.

The objective of the work performed under this contract was to determine if the results obtained in the Bureau study could be reproduced; thus, the task was to ascertain the effect of free stream velocity, cyclone inlet orientation, and particle size on the particle sampling efficiency and size selective cut-off characteristics of the cyclone. These tests were to be performed with free stream velocities ranging from 1 to 9 m/sec. For these tests, cyclone orientations of 0, 90, 180, 270 degrees were used with zero being defined as the inlet directed into the airflow, i.e. the free stream flow was perpendicular to the plane that is tangent to the cyclindrical cyclone body at the inlet. Due to the limited scope of this contract, the work was to be limited to demonstrating the effect of free stream velocity and inlet orientation on the performance of the cyclone. Furthermore, tests were also to be performed with a shielded cyclone inlet. However, the intent of these tests was to demonstrate whether or not shielding was a promising technique rather than to determine through a definitive study the optimum parameters for this cyclone shield.

5.2 Experimental Setup and Procedures

The cyclone evaluation tests were performed in a wind tunnel located in the Particle Technology Laboratory. A schematic diagram of the wind tunnel setup is presented in Figure 5.1. The wind tunnel is a horizontal duct with air flow maintained by a suction blower. Aerosol plus filtered air is drawn into the inlet of the wind tunnel and passed through two different test sections. The first section has a 51 x 51 cm square cross section while the second has a 35.5 cm diameter circular cross section. The air flow velocities in these two sections can be varied from approximately 0.14 to 3 m/sec in the first section and from 1 to 10 m/sec in the second one. Experimental tests were conducted utilizing both sections.

For these tests, two different aerosol types were used. The initial tests were performed using monodisperse aerosol generated with a TSI Model 3050

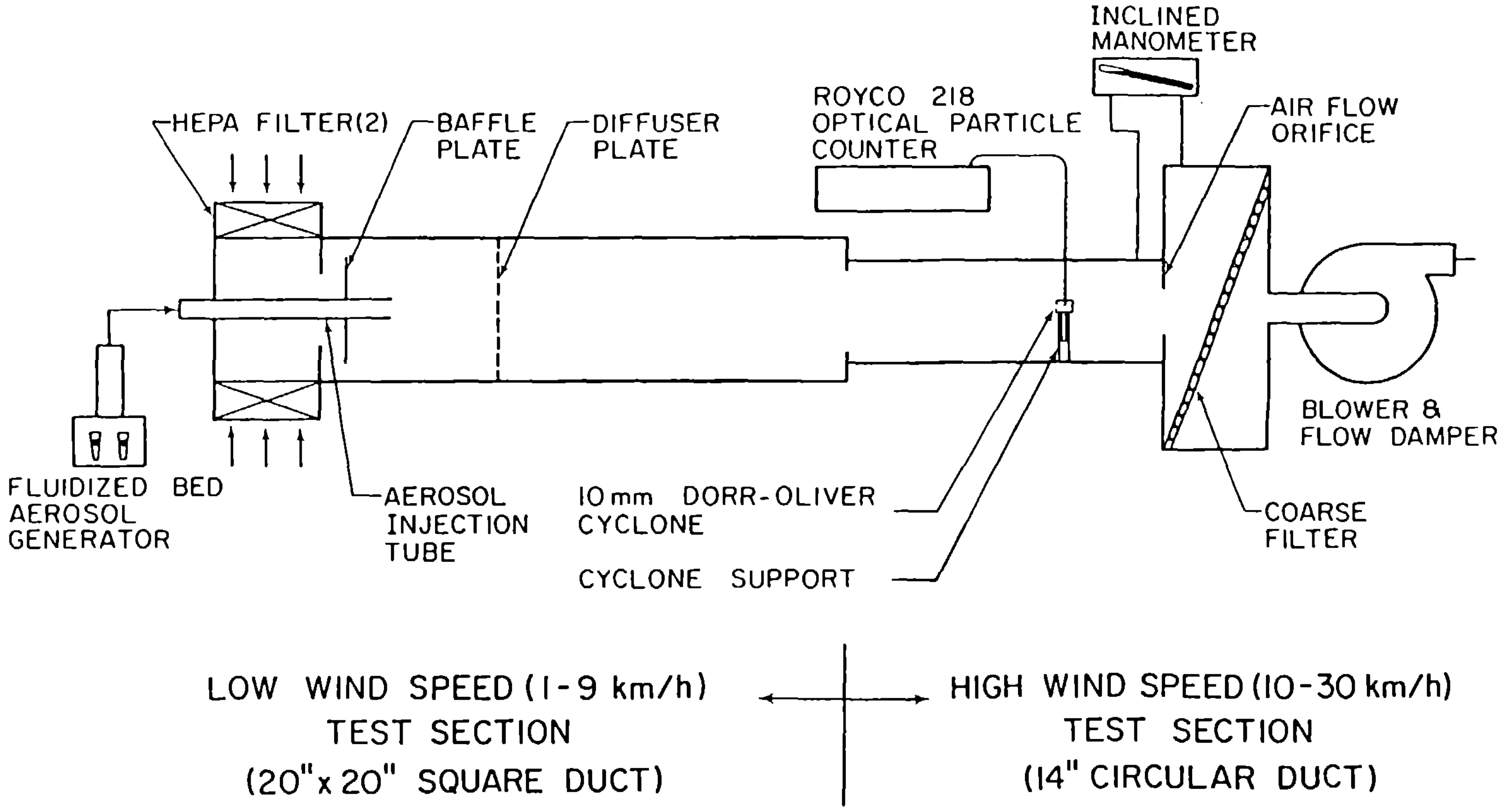

Figure 5.1. Schematic diagram of wind tunnel test setup.

vibrating orifice monodisperse aerosol generator (VOMA). The particles generated with these techniques were 3.5 and 7 μm diameter solid ammonium fluorescein particles. The second type of test aerosol used was polydisperse coal dust generated using the TSI Model 3400 fluidized bed aerosol generator.

Two different techniques were used to determine the particle concentration downstream of the cyclone. The first utilized the fact that ammonium fluorescein can be detected using fluorometric techniques. These particles, upon passing through the cyclone, were collected on an afterfilter which was the standard 37 mm filter used with the 10 mm Dorr-Oliver cyclone. Aerosol was drawn into the cyclone at a flowrate of 2 L/min by a Bendix Model BDX 60 permissable air sampling pump. After each test, these filters were removed, washed in 20 cc of 0.1 normal ammonium hydroxide solution, and a fluorometer utilized to determine the fluorescein concentration. To make a test run, the actual aerosol concentration in the wind tunnel was first determined using an isokinetic sampling probe. Next, this probe was replaced with the cyclone. The fraction of particle penetrating through the cyclone to the afterfilter was determined by comparing the quantity of particulate matter collected on the afterfilter to that collected on the filter in the isokinetic probe. Initial tests at high free stream velocities indicated the particle concentration produced by the generator was too low to accurately determine the particle concentration without testing for an inordinate length of time. However, the tests at low free stream velocity conditions of 1 to 6 m/sec did show that the particle penetration through the cyclone was in the 20 to 30% range for 3.5 μm diameter particles and about 4% for the 7 μm diameter particles.

The second technique made use of the Royco 218 optical particle counter (OPC) and the polydisperse coal dust. This OPC had been modified under a previous Bureau of Mines contract (13, 21) to operate at 2 L/min. The OPC was connected directly onto the exit of the cyclone and the pump contained in the OPC used to draw the aerosol through the cyclone and into the OPC. The OPC was used to determine the particle concentration as a function of particle size in the 0.8 to 15 μm aerodynamic particle size range. The data was divided into five particle size ranges using a multichannel analysis (MCA). The response of the OPC as a function of aerodynamic particle size was calibrated under a previous Bureau of Mines contract (13) using a technique described by Marple and Rubow (22).

Figure 5.2 shows the various orientations of the cyclone inlet, relative to the direction of the airflow, utilized in this experiment. The cyclone orientation was defined as the angle between the actual direction of the wind and a line which is drawn perpendicular to a plane that is tangent to the cylindrical body of the cyclone at the inlet side. For these experiments, directions of 0, 90, 180, and 270 degrees were primarily used. Directions of 45, 75, 105, 135, 225 and 315 degrees also were used in one set of experiments.

A schematic diagram of the cross section of the cyclone with the shield mounted on it is shown in Figure 5.2. The shield is composed of a metal tube, which had an external diameter of 3.7 cm and a length of 2.5 cm. The axis of the shield coincided with the axis of the cyclone and the midpoint of the shield was centered at the midpoint of the cyclone inlet.

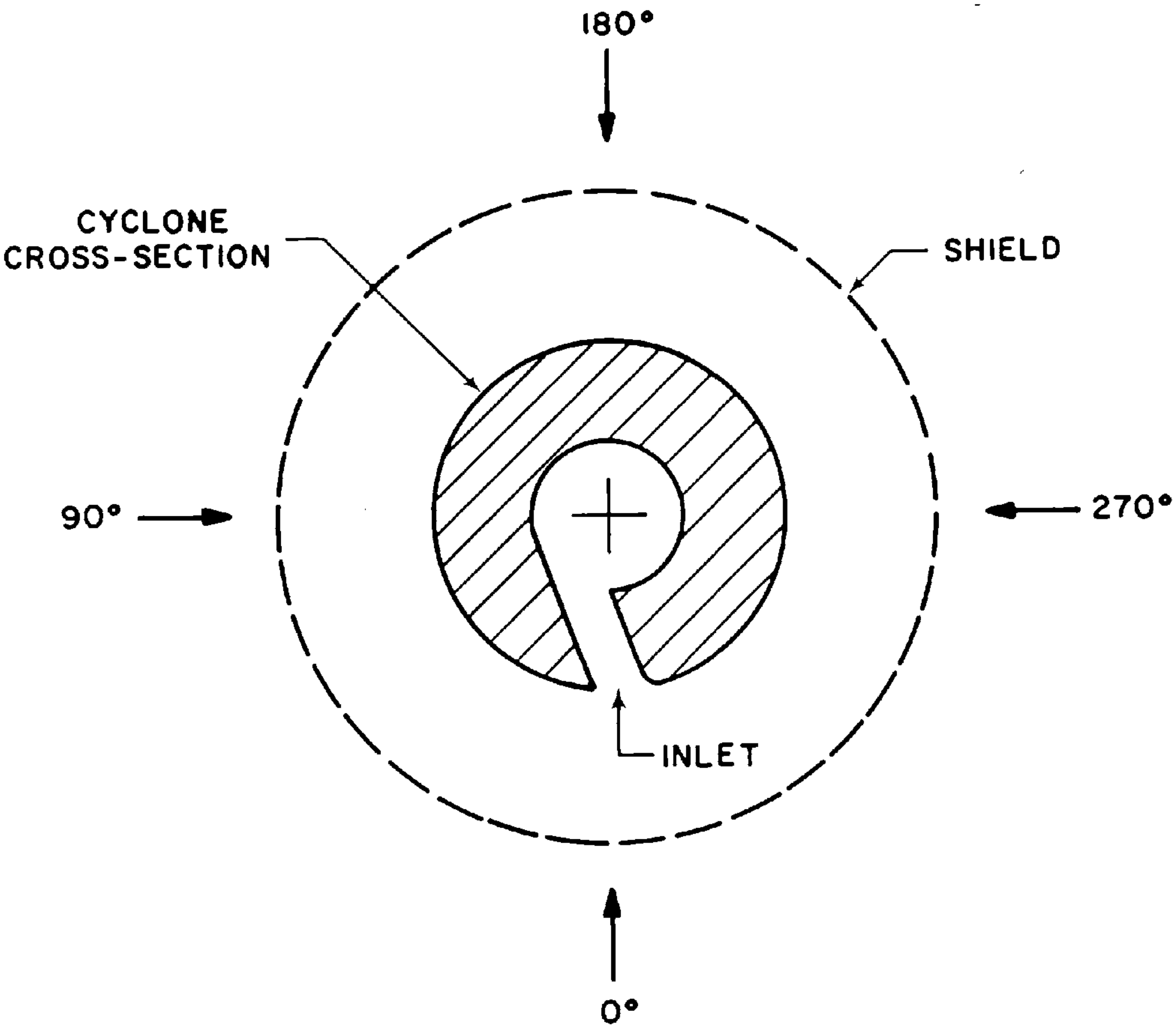

Figure 5.2. Schematic diagram of cyclone cross section showing the inlet orientation relative to air flow direction.

5.3 Results

The results of the unshielded cyclone evaluation are presented in Figures 5.3 to 5.5 and Table 5.1. Data for each particle size and free stream velocity have been normalized to the particle concentration obtained with the unshielded cyclone at an orientation of 0°. Since the particle concentration was measured downstream of the cyclone, this data includes the combined effect of both inlet sampling efficiency and penetration through the cyclone. The uncertainty for all the data is indicated by the error bars of the graphs. The uncertainty is typically on the order of 10% and determined by computing the standard deviation with the data obtained from two to six runs for each test condition. In general, the results presented in Figure 5.3 and 5.5 show that the sampling efficiency decreases with increasing particle size and increasing the free stream velocity. The effects are most pronounced at orientations of 90 and 270°. Also, at orientations of 90 and 270 degrees, the data show the sampling efficiencies at velocities in the range of 1 to 3 m/sec are greater than those obtained for the 0° orientation. The magnitude of this result increases with increasing particle size. For velocities greater than 3 m/sec, the sampling efficiencies relative to those obtained for the 0° orientation are less than 100%. The magnitude of the difference from 100% increases with increasing particle size and velocity. For example, the sampling efficiency for the largest size particles, i.e. those in the 3.8 to 6 μm range, decreases to approximately 31% as the free stream velocity approaches 9 m/sec. However, for the smaller particle sizes, i.e. those in the 0.8 to 1.1 μm range, the efficiency only drops off to approximately 75% for the 90° orientation. The results for the 180° orientation show no discernable effect of velocity on the sampling efficiency. Likewise there is no discernable effect of particle size.

To determine the effect of sampler orientation on the cyclone particle sampling characteristics in more detail, a special study was conducted at a free stream velocity of 8.1 m/sec. These results are presented in Table 5.2 and Figure 5.6. The results show minimum sampling efficiencies at two orientations: a little less than 90° and a little less than 270°. From about 135° to 225° the sampler collection efficiency is relatively insensitive to orientation.

The data obtained when using the shielded cyclone are presented in Figures 5.7 to 5.11 and Table 5.1. The data for each of the four orientations has been normalized by those obtained for the unshielded cyclone with an orientation of 0°. The uncertainty in the data is on the order of 8% and was obtained by computing the standard deviation obtained from the two to six runs performed for each condition. These results show that the shield greatly reduces the effect of free stream velocity and cyclone orientation on sampling efficiency. Variation in the sampling efficiency with changes in particle size, cyclone orientation and free stream velocity are usually less than 5% with the maximum variation found to be 15%. These variations are comparable to the uncertainty in the data. Thus, the results show the cyclone, when operated with the shield, would be a suitable way to minimize the effect of free stream velocity and particle size on the sampling characteristics of the cyclone. One should note that no attempt was made to optimize the size and shape of the shield used in this study.

The data obtained in this study are in good agreement with those reported by Cecala and coworkers (19). They used a polydisperse coal dust which had a mass median diameter of approximately 4.5 μm and geometric standard deviation of

Table 5.1

Experimentally Determined Cyclone Sampling Efficiency as a Function of Free Stream Velocity, Cyclone Orientation and Particle Size

MCA Channel[1]	Sampling Efficiency Relative to Unshielded 0° Orientation, %, for Free Stream Velocities, m/sec and (ft/min)						
	1.02 (200)	1.52 (300)	2.03 (400)	4.06 (800)	6.1 (1200)	8.1 (1600)	9.0 (1770)
	90° Orientation, Unshielded						
2	100	98	97	91	87	80	74
3	99	98	100	84	68	64	53
4	100	110	103	76	65	45	39
5	109	110	113	69	57	39	31
	180° Orientation, Unshielded						
2	99	96	99	101	101	98	96
3	98	99	99	98	101	97	91
4	96	102	102	102	102	96	97
5	95	104	108	95	108	94	81
	270° Orientation, Unshielded						
2	98	96	98	88	83	80	63
3	100	94	94	84	69	66	53
4	96	94	96	76	56	49	36
5	94	100	102	63	41	41	26
	0° Orientation, Shielded						
2	97	96	99	95	97	99	
3	98	96	94	92	96	96	
4	95	96	98	94	98	108	
5	99	98	99	87	90	112	
	90° Orientation, Shielded						
2	97	96	99	95	102	98	
3	100	96	95	93	98	96	
4	104	97	98	90	103	102	
5	104	105	95	86	101	110	
	180° Orientation, Shielded						
2	98	96	99	97	100	99	
3	100	96	97	96	97	100	
4	100	96	100	94	98	103	
5	97	102	97	90	92	115	
	270° Orientation, Shielded						
2	96	97	97	95	94	96	
3	100	94	94	90	95	91	
4	98	93	97	90	101	95	
5	98	105	100	93	101	102	

[1] MCA channels correspond to the following aerodynamic particle diameters - 2:0.8-1.1 µm, 3:1.1-2.0 µm, 4:2.0-3.3 µm and 5:33-6.0 µm.

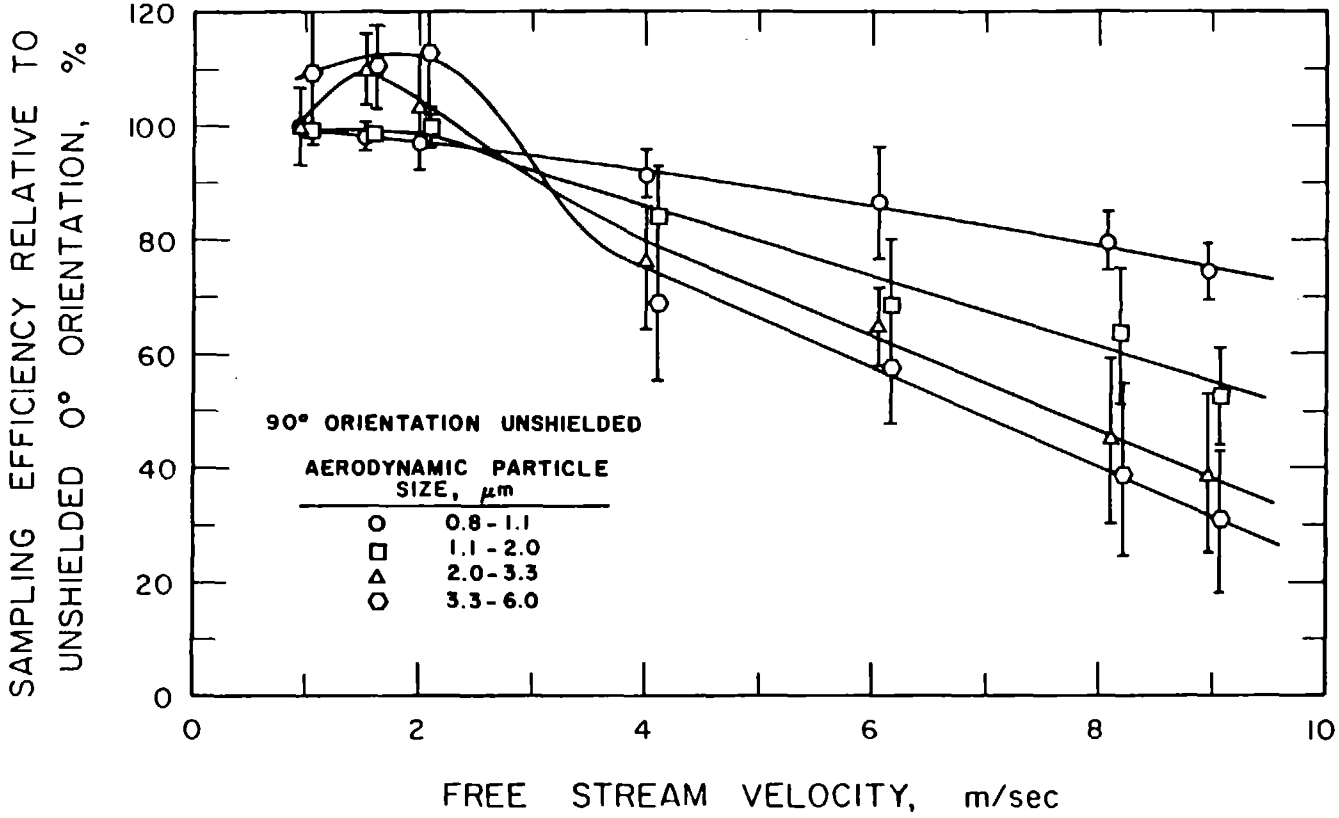

Figure 5.3. Sampling efficiency of unshielded cyclone at 90^0 orientation relative to unshielded 0^0 orientation.

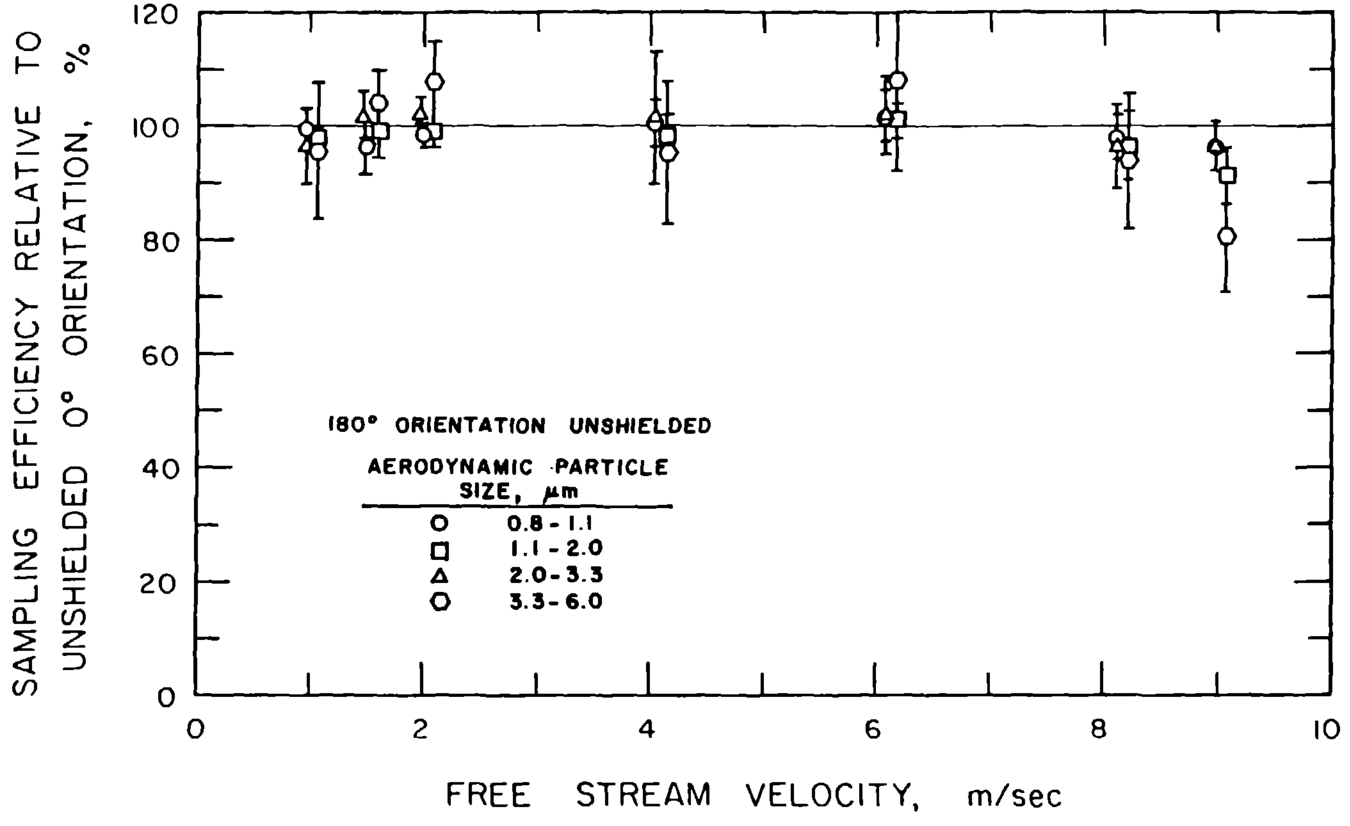

Figure 5.4. Sampling efficiency of unshielded cyclone at 180^0 orientation relative to unshielded 0^0 orientation.

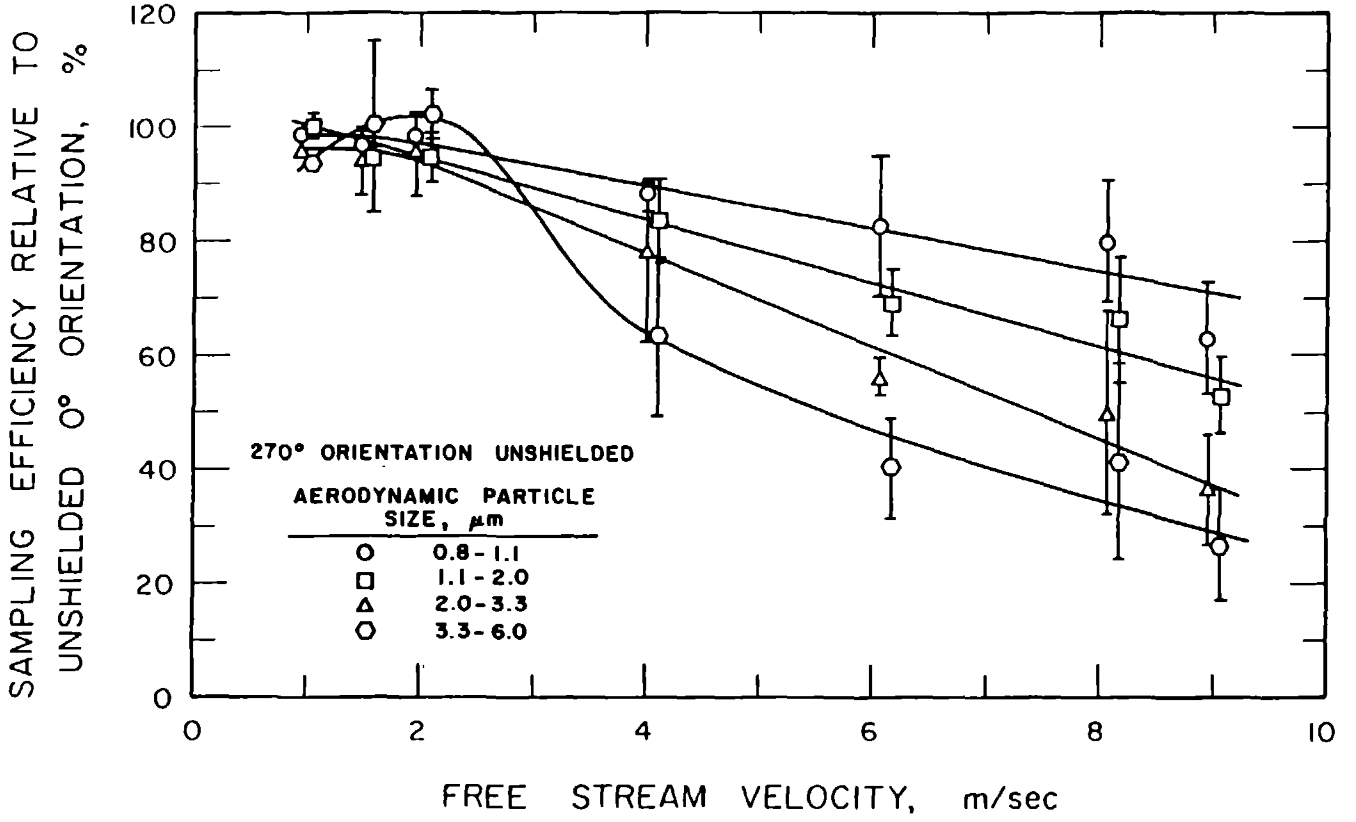

Figure 5.5. Sampling efficiency of unshielded cyclone at 270^0 orientation relative to unshielded 0^0 orientation.

Table 5.2
Experimentally Determined Cyclone Sampling Efficiency as a Function of Cyclone Orientation for a Free Stream Velocity of 8.1 m/sec

Orientation, °	Sampling Efficiency Relative to Unshielded 0° Orientation for Particle Size Ranges, μm, of			
	0.8-1.1	1.1-2.0	2.0-3.3	3.3-6.0
45	97	86	69	62
75	69	54	27	12
90	80	64	45	39
105	95	85	69	50
135	105	104	104	94
180	98	97	96	94
225	100	99	96	81
270	80	66	49	41
315	89	88	73	66

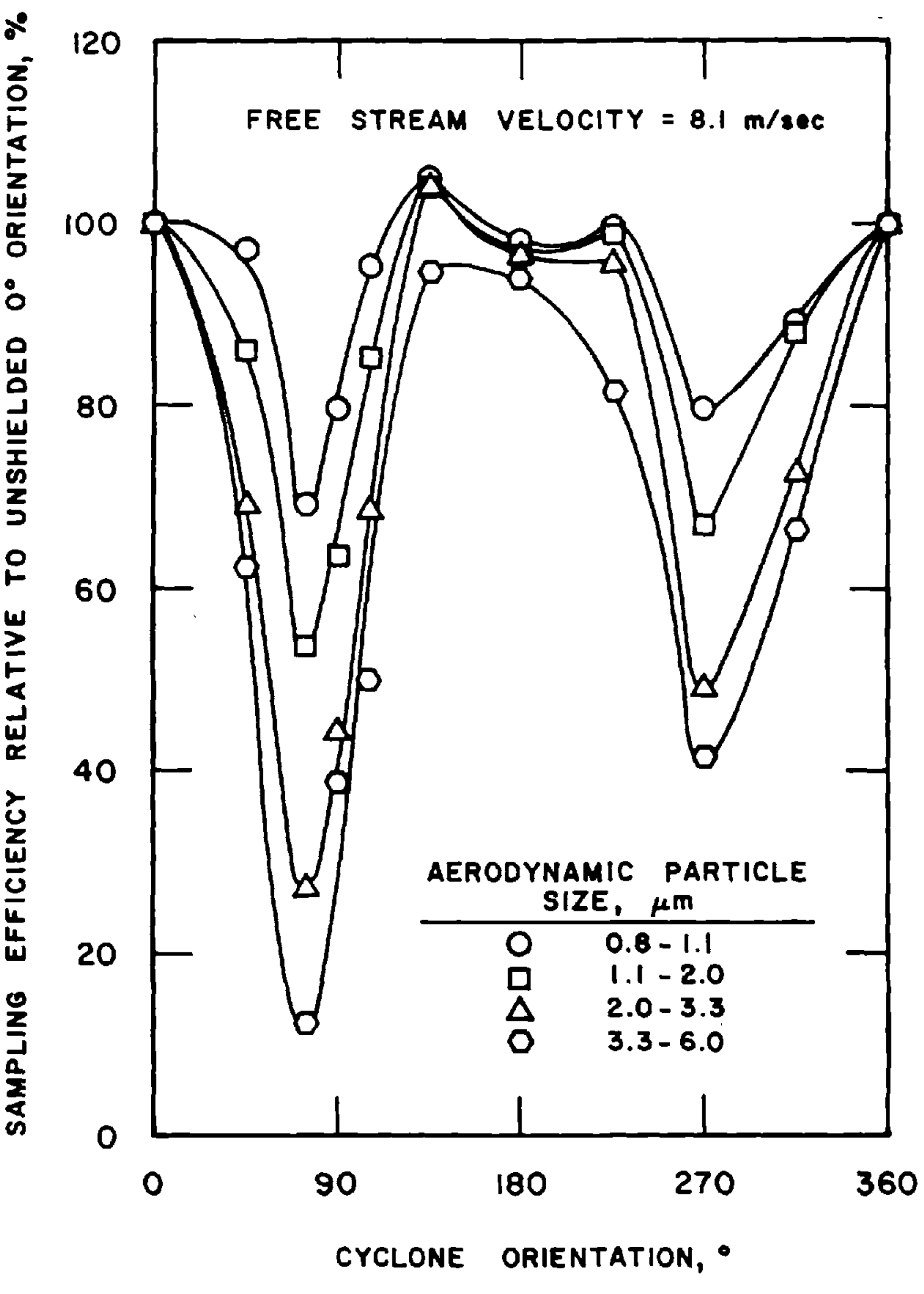

Figure 5.6. Sampling efficiency of unshielded cyclone as a function of cyclone orientation relative to unshielded 0° orientation.

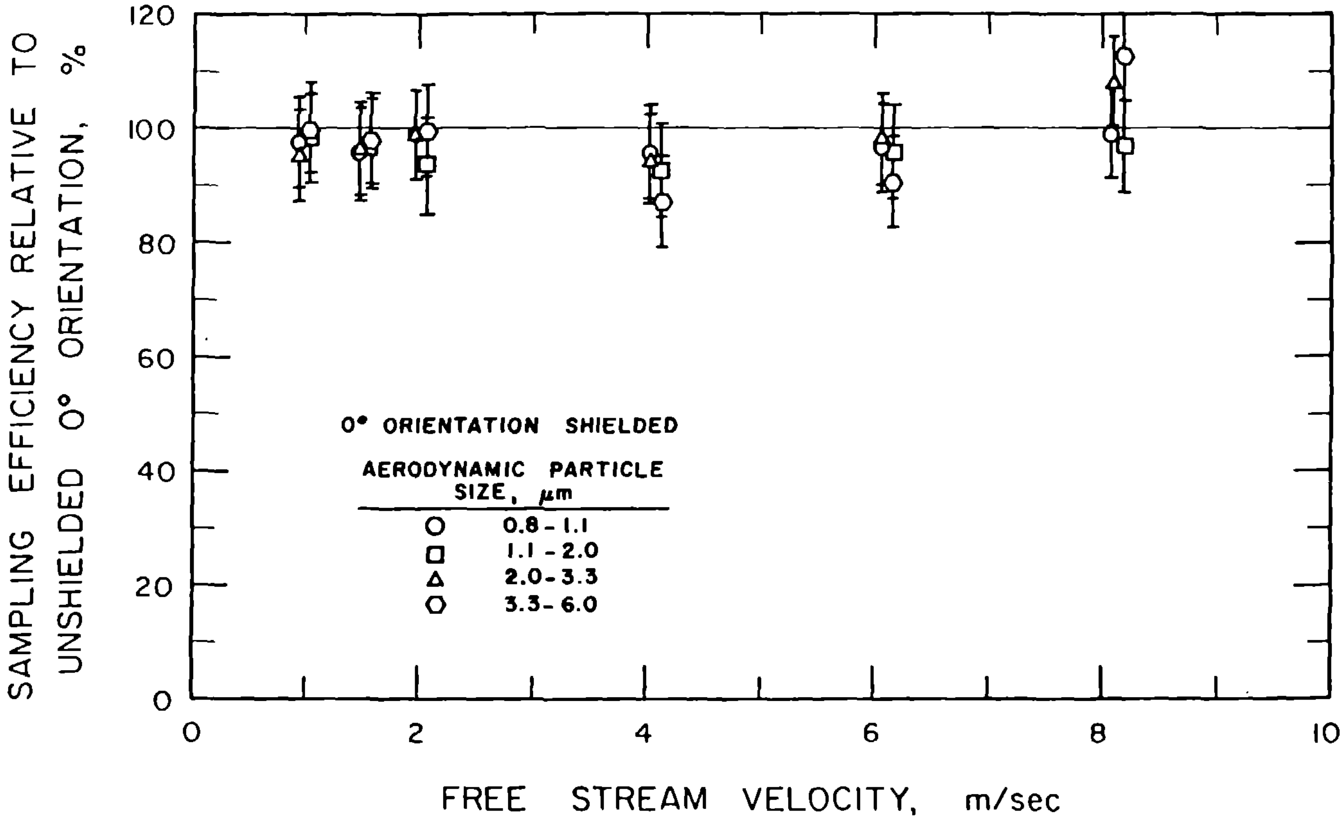

Figure 5.7. Sampling efficiency of shielded cyclone at 0^{0} orientation relative to unshielded 0^{0} orientation.

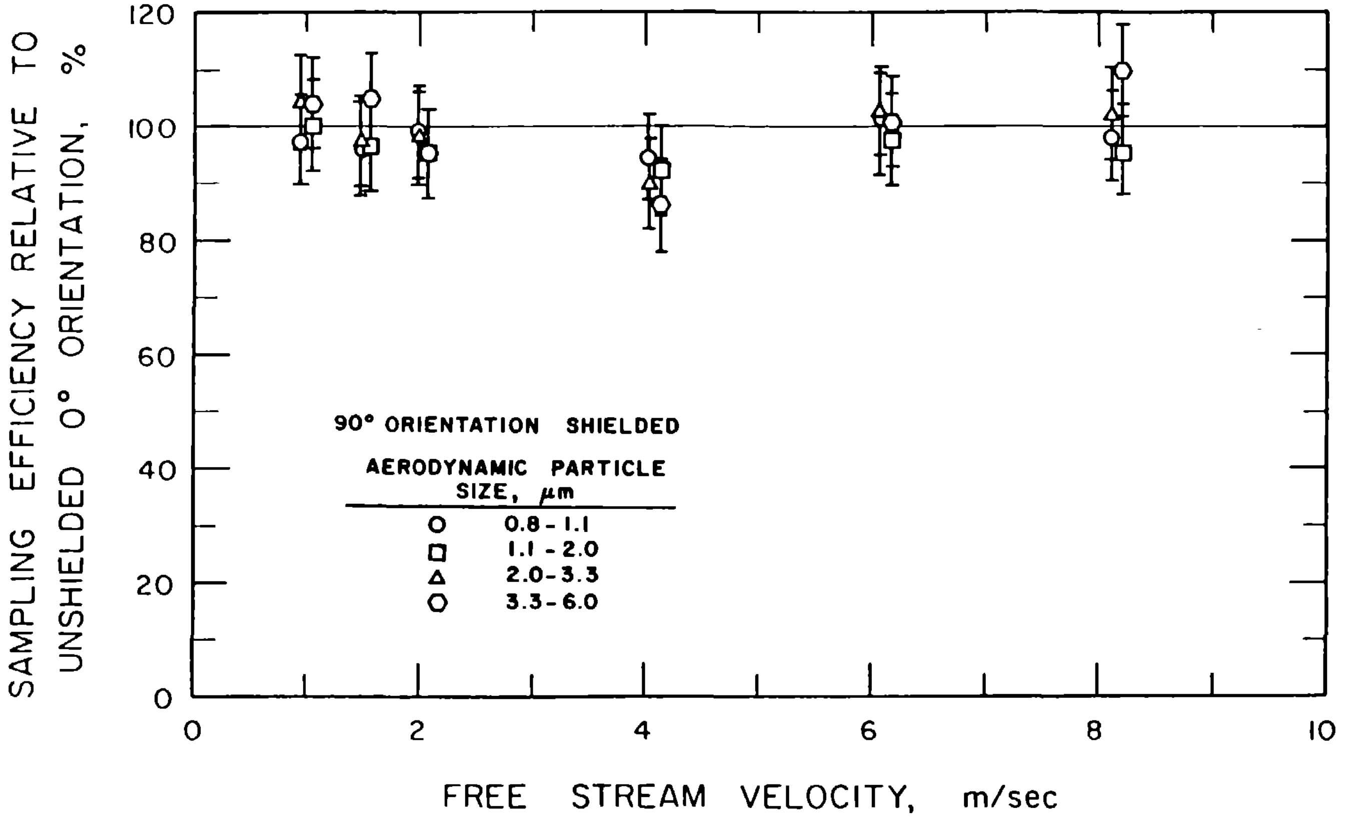

Figure 5.8. Sampling efficiency of shielded cyclone at 90^0 orientation relative to unshielded 0^0 orientation.

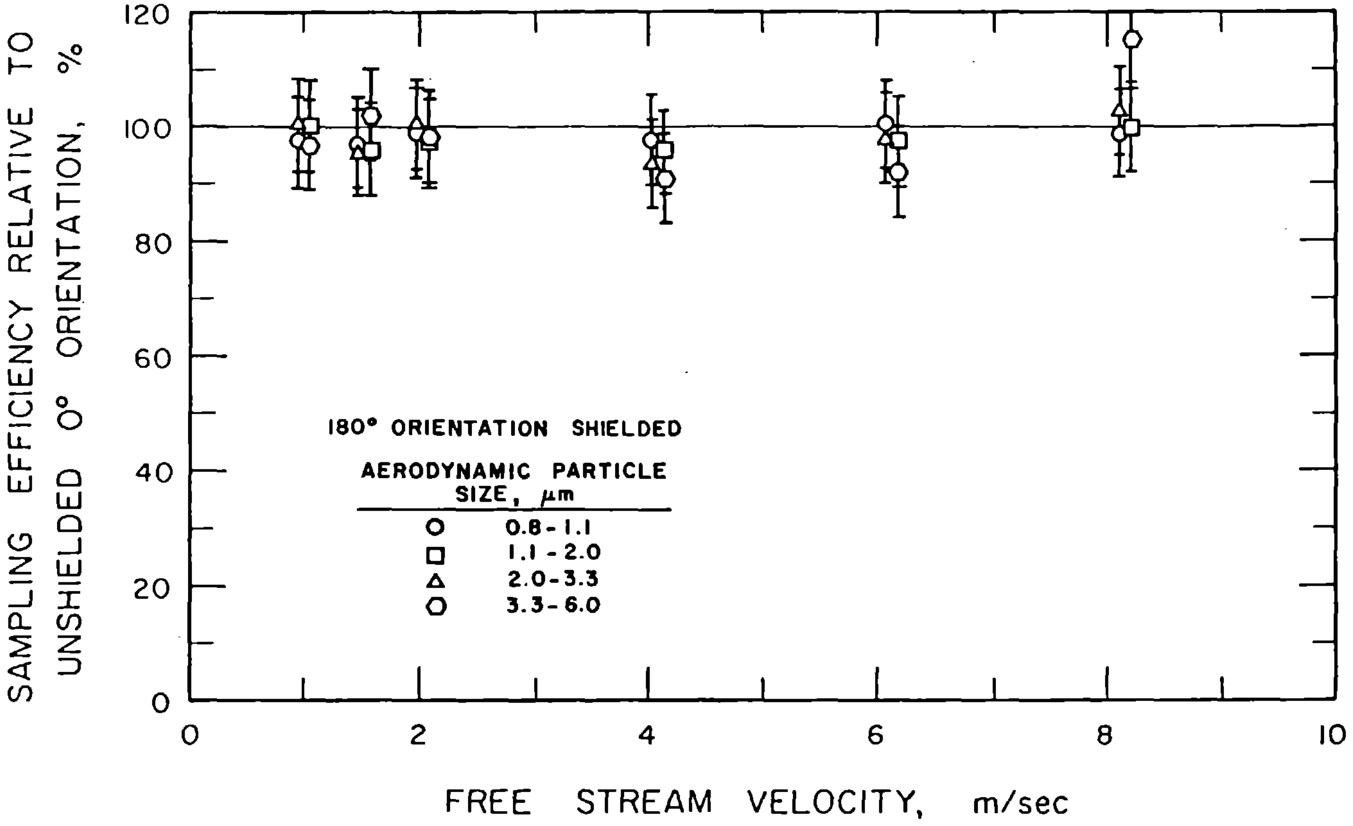

Figure 5.9. Sampling efficiency of shielded cyclone at 180^0 orientation relative to unshielded 0^0 orientation.

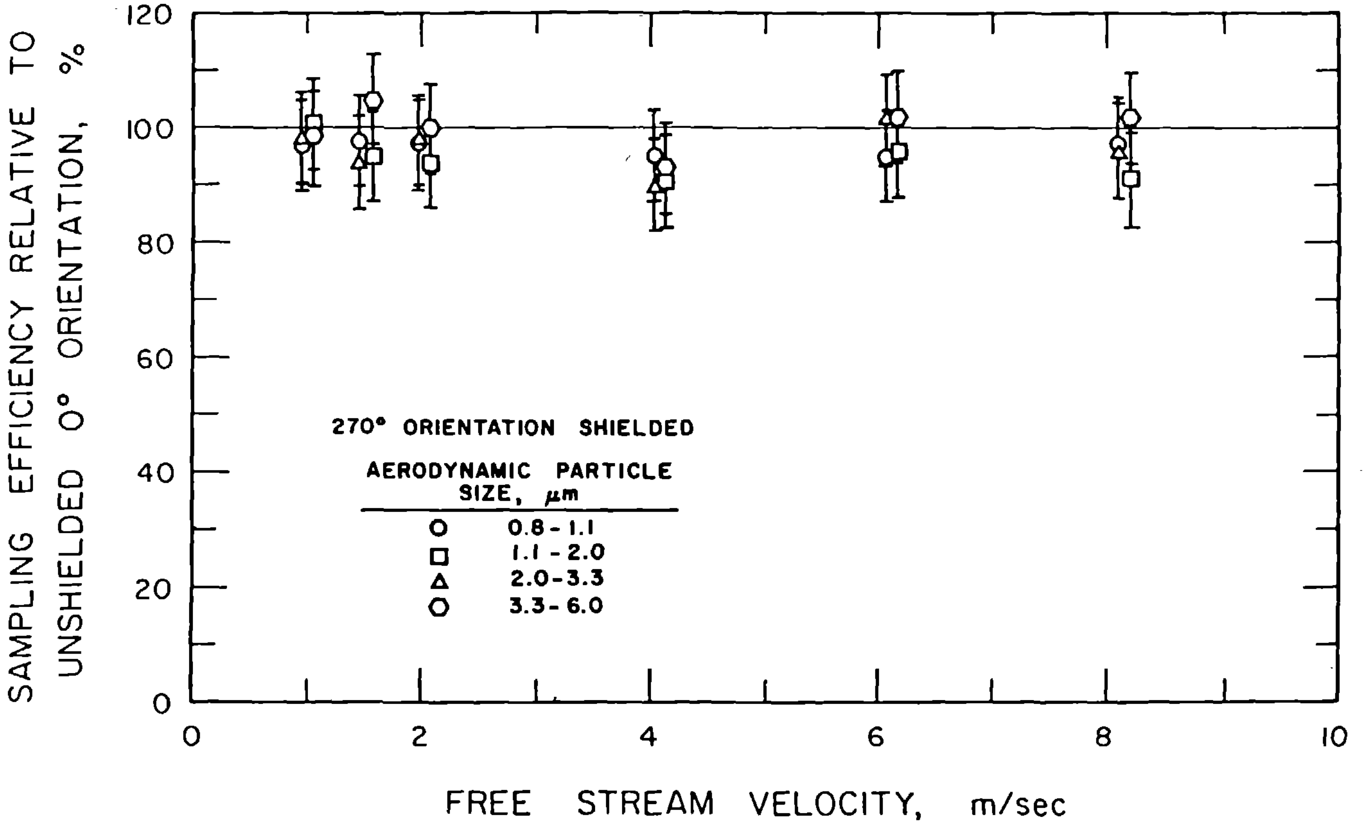

Figure 5.10. Sampling efficiency of shielded cyclone at 270^0 orientation relative to unshielded 0^0 orientation.

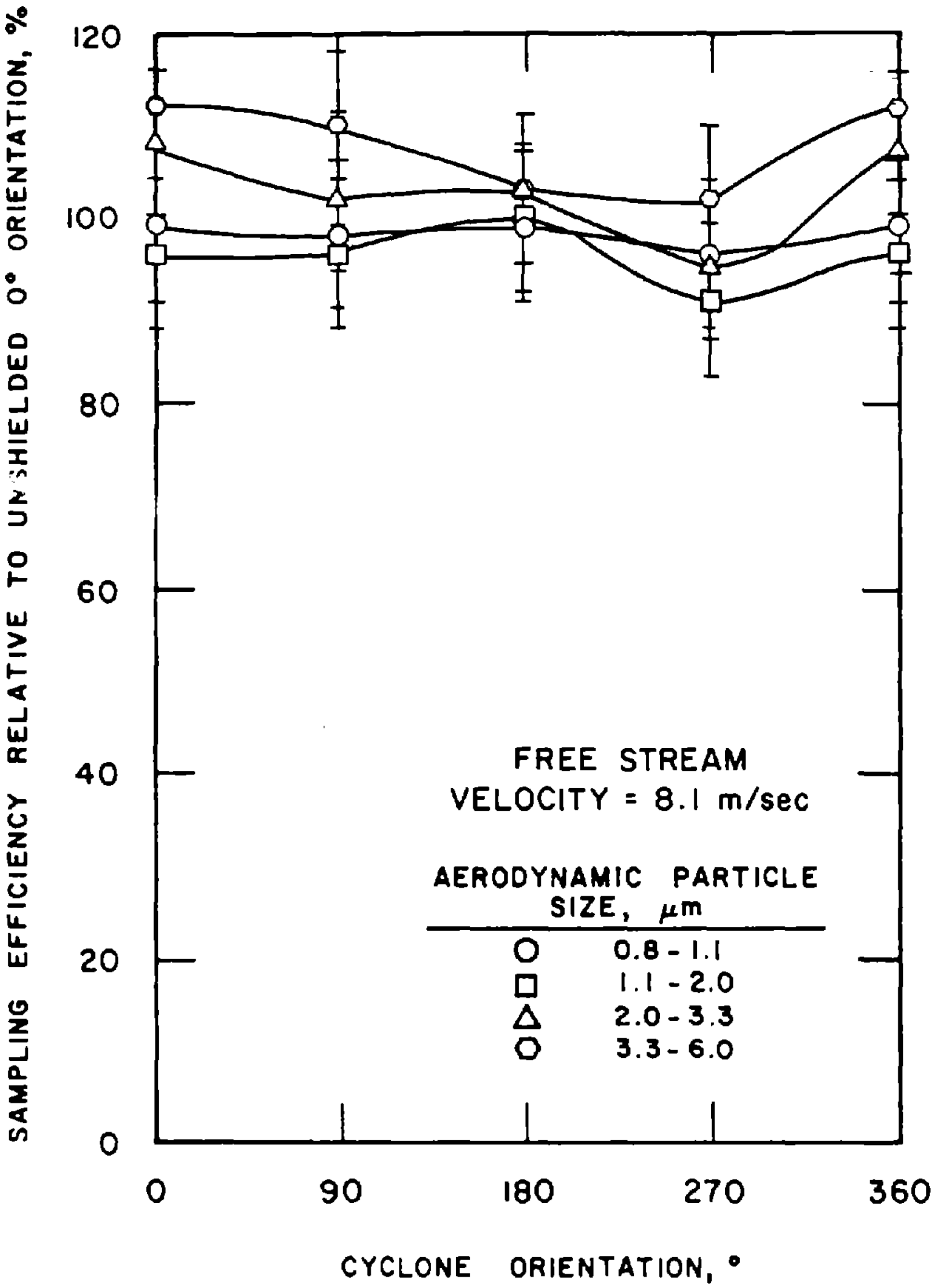

Figure 5.11. Sampling efficiency of shielded cyclone as a function of cyclone orientation relative to unshielded 0° orientation.

about 2.5. The mass median diameter of the respirable fraction of this aerosol, i.e., that which penetrated the cyclone and was detected by their aerosol concentration detector, was on the order of 2 to 2.5 μm. Consequently the latter mean particle size should be used when comparing the data of their study with this study. The results of both studies compare quite favorably with both quantitatively showing the same effect of free stream velocity, cyclone orientation and shielding of the inlet.

The absolute magnitude of the effect of free stream velocity and cyclone orientation on the cyclone sampling efficiency cannot be directly determined from the data obtained in this study. This is because the data is presentnd relative to that obtained for the unshielded cyclone when operated in the 0° orientation. The data obtained for the 0° orientation is also dependent on free stream velocity and particle size. This occurs because the particle sampling was done under anisokinetic sampling conditions and the cyclone consists of a blunt body as opposed to a sharp-edged orifice sampler. Anisokinetic sampling means that the mean free stream velocity upstream of the cyclone inlet was not identical to the mean fluid velocity in the inlet. The experiments were performed with subisokinetic as well as superisokinetic sampling, i.e. the velocities were less than and greater than the mean sampler inlet velocity.

As a first approximation, the effect of free stream velocity and particle size on the cyclone sampling efficiency for the 0° orientation case can be estimated using the empirically and theoretically determined data for anisokinetic sampling using thin walled and thick walled sampling tubes. Numerous researchers have studied the anisokinetic sampling problem with thin walled tubes but little experimental or theoretical work exits for blunt or thick walled sampling probes. Furthermore, these studies have been almost exclusively limited to isoaxial sampling in a cylindrical tube. For the case of the cyclone, the inlet is not only rectangular in shape but also is located on a cylindrical body, the axis of which is located perpendicular to the direction of the free stream flow. However, as a first approximation, the degree of sampling bias as a function of free stream velocity and particle size can be predicted for the cyclone using the coaxial thin walled sampling tube results.

The inlet aspiration efficiency based on the semiempirical work of Belyaev and Levin (23) for a thin walled tube is presented in the Figure 5.12 as a function of free stream velocity and particle size. The aspiration efficiency is defined as the concentration of particles which cross the inlet plane of the sampler relative to that which exists in the unsampled aerosol upstream of the inlet. Data are given for particle diameters of 1, 2, 3.5, 5, 7, and 10 μm. These data were obtained for a sampling flow rate of 2 L/min and a tube diameter of 2.15 mm which is equivalent to the hydraulic diameter of the cyclone inlet. The size of the cyclone inlet was determined to be 2.2 mm by 2.15 mm. The resulting inlet mean velocity was determined to be 7.2 m/sec (1420 ft/min).

The data in Figure 5.12 show that the aspiration efficiency decreases with increasing particle size and decreasing wind velocity for free stream velocities less than the inlet velocity of the sampler. For velocities greater than inlet velocity, the aspiration efficiency increases with increasing particle size and increasing free stream velocity. As an example, for a 3.5 μm diameter particle the aspiration efficiency varies from 92% to 113% as the free stream velocity increases from 0.25 to 10 m/sec.

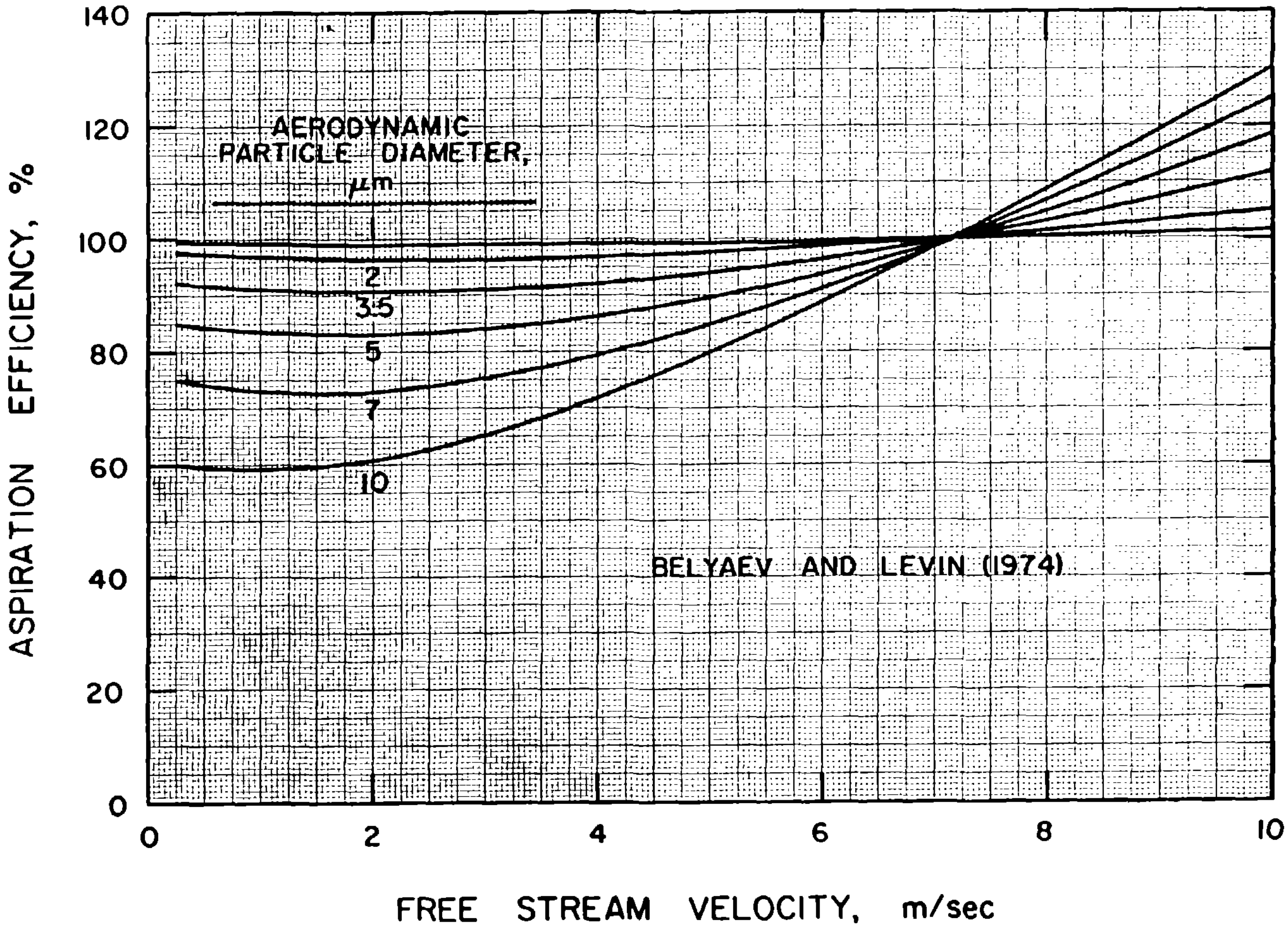

Figure 5.12. Theoretically predicted inlet aspiration efficiency for isoaxial sampling into a thin walled cylindical tube with a diameter of 0.215 cm at a flow rate of 2.0 L/m.

The data presented in Figure 5.12 were obtained for a thin-walled sampling probe which is not the case for the inlet of the cyclone. For this case, the inlet can be more appropriately assumed to be blunt or thick-walled sampling probe. However, there is very little experimental data to determine the aspiration efficiency for this case. Work by Belayev and Levin (23) and Marple and Rader (24) have shown for a few limited cases that the sampling efficiency is similar to that obtained for the sharp-edged probe.

As a first approximation, the data presented in Figure 5.12 can be used to adjust the normalized sampling efficiency data, presented in Figures 5.3 to 5.10, for the effect of sampling bias in the particle concentration measured at the 0° orientation.

The data presented in Figure 5.12 can be used to explain the effect of normalized sampling efficiencies being greater than 100% which were observed for the low free stream velocities. The data presented in Figure 5.12 show that the cyclone should under sample particles at low free stream velocities by 5 to 17% for particles in the 2 to 5 μm diameter size range. This degree of undersampling is comparable to the normalized oversampling reported at the low free stream velocities. At the higher velocities, the aspiration efficiencies presented in Figure 5.12 are greater than 100%. For free stream velocities in this range, the reported normalized cyclone data would be lower by the degree of oversampling which occurred in the 0° orientation data. As an example, the effect of adjusting the particle concentration measured at 0° orientation for the sampling bias, on the sampling efficiency obtained for the 90° orientation, is illustrated in Figure 5.13. The data are presented for two particle size ranges, namely 0.8 to 1.1 and 3.3 to 6.0 μm. Three sets of data are presented, the first is the sampling efficiencies found for the 90° orientation relative to those obtained at 0° orientation, the second set shows the inlet aspiration coefficients for a thin-walled sampling tube, and the third is the sampling efficiencies at 90° adjusted by the aspiration coefficient. By adjusting the sampling efficiency data for the sampling bias associated with the 0° orientation data, the effects of particle size and free stream velocity on sampling efficiency as a function of cyclone orientation are more clearly seen.

5.4 Summary

The test results obtained with the Dorr-Oliver 10 mm cyclone show that the particle sampling characteristics can be significantly affected when sampling in high free stream velocity conditions. These effects are a function of free stream velocity, orientation of the cyclone inlet relative to the free stream direction and particle size. The effect of velocity can cause variations of 10% or greater in the sampling efficiency when sampling from free streams with velocities over 3 m/sec. Changes in cyclone orientation can cause variations as high as 70% in the particle sampling efficiency of the cyclone. The most pronounced effects were observed for inlet orientations in the vicinity of 90 and 270 degrees with the sampling efficiency decreasing as the free stream velocity and particle size increase.

The placement of a cylindical shield around the cyclone in the region of the inlet has found to reduce the effect of free stream velocity, inlet oreintation and particle size. Variations in the sampling efficiencies due to these effects were generally 10% or less which is equivalent to the uncertainty in the measurement. No attempt was made to optimize the shielding.

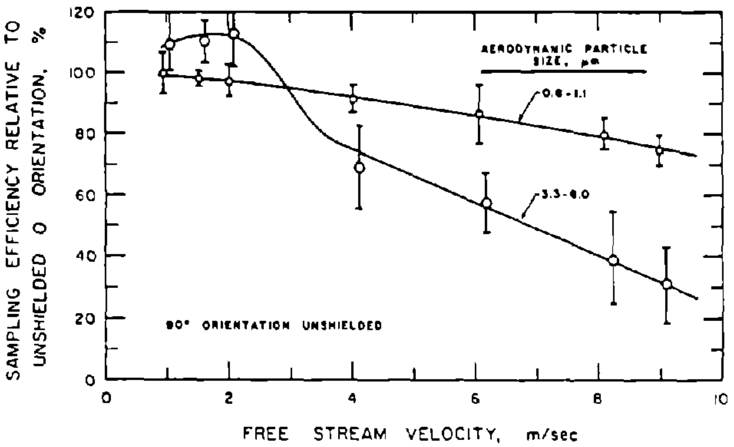

(a) Sampling efficiency relative to 0^0 orientation.

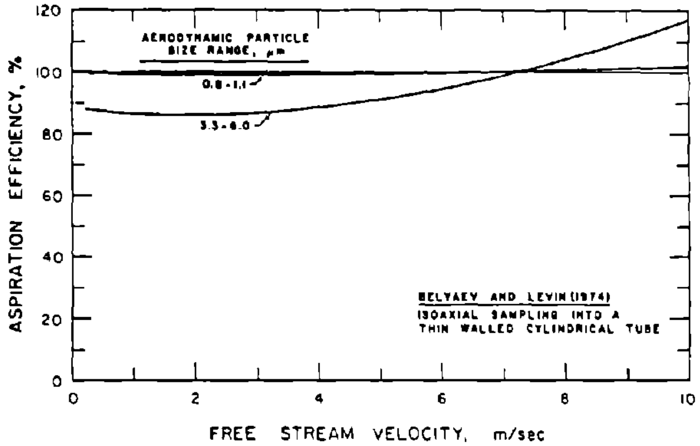

(b) Estimated bias in sampling efficiency at 0^0orientation based on isoaxial sampling into a thin walled cylindical tube.

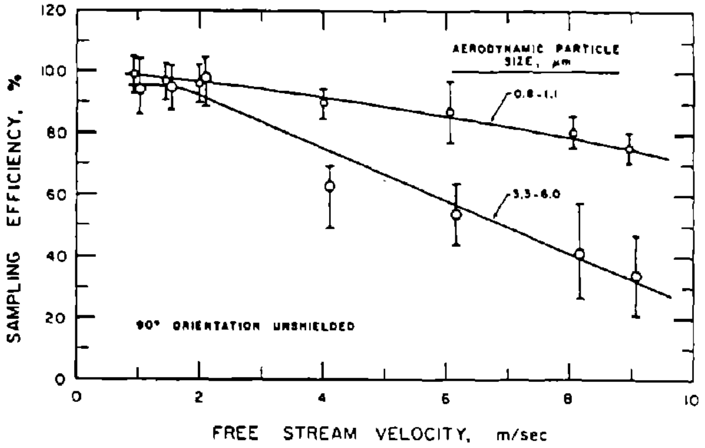

(c) Sampling efficiency adjusted for sampling bias at 0^0 orientation.

Figure 5.13. Procedure of correcting sampling efficiency data for sampling bais in sampling efficiency of the unshielded cyclone at 0^0 orientation.

The results of this study are in good agreement with those obtained by Cecala et al.(19). Both studies show quantitatively the same effect of free stream velocity, cyclone orientation relative to the free stream and inlet shielding on sampling efficiency.

Free stream velocities in excess of 2 m/sec can be encountered when sampling in both underground and surface mining environments. The results of this study show that proper care must be given to the orientation of the cyclone inlet when sampling in these high velocity conditions. Further, a properly designed inlet shield will minimize the effect of high free stream velocities on the sampling efficiency.

CHAPTER 6

LARGE PARTICLE/IMPACTOR STUDY

6.1 Introduction

When working with impactors, often the theoretically predicted and expermentally determined efficiency curves do not agree for particles larger than approximately 4 or 5 μm. The reason for this discrepancy was not known but assumed to be a problem with the theoretical formulation.

To study this phenomenon, the theory was modified to include refinements which were expected to have secondary effects on the particle collection. These included making provisions for the physical size of the particles within the impactor in the form of an interception distance and the inclusion of non-Stokesian drag coefficients which are associated with the larger particles. In addition a study was made of the gravitational effects on the particles, which also may have been important for the large diameter particles. Under certain conditions, it was found that these secondary effects are quite large and could easily account for the discrepancy between the experimental and theoretical curves.

6.2 Effect of Interception Distance and Non-Stokesian Drag

A paper describing the effects of including the particle interception distance and the correct particle drag coefficient (ultraStokesian) on the theoretical impactor collection efficiency curves is included in Appendix B. Also included in this work is the effect of using a finer calculation grid, which is employed in finite difference type of solutions, than was used in the previous theory.

Appendix B contains the details of the study. The revision of impactor theory, including grid refinement, ultraStokesian equations for the drag of the particles and interception of the particles at the impaction plate resulted in shifts of 5-10% in efficiency curves for inertial impactors.

The most significant change in efficiency curves was found from calculation grid refinement which is now practical with higher speed computers. The influence of increasing the number of node points has been to predict an efficiency curve which is shifted toward larger particle diameters than predicted with the original theory and grid spacing. The new theory predicts slightly sharper cuts for round impactors while producing rectangular impactor efficiency curves which demonstrate a more pronounced S-shape than the original theory.

The inclusion of particle interception at the plate results in the appearance of a small tail at the low-efficiency range of the characteristic curves. This tail becomes less pronounced with grid spacing refinement and is not significant enough to explain the difference between experiment and theory. For very large particles, however, the effect of particle interception may become more pronounced.

The use of ultraStokesian drag coefficients shifts the collection efficiency curves toward larger particle diameters. This shift is generally small, 5 to

10%, for typical impactor systems. Noticeable deviations due to ultraStokesian effects will be observed for higher Reynolds numbers at the higher efficiencies.

6.3 Effect of Gravity

The impactor theory to date has not included the gravitational forces on the particles. Gravitational forces could be important for large particles. Therefore, a set of efficiency curves were calculated for round impactors of several nozzle Reynolds numbers and nozzle-to-plate distances with gravitational forces included.

Table 6.1 summarizes the cases studied and indicate the corresponding figure number where the efficiency curves are presented. In these figures, $\sqrt{St}$ is a dimensionless particle diameter defined as:

$$\sqrt{St} = \sqrt{\frac{\rho_p \, V_o \, C \, D_p{}^2}{9 \, \mu \, W}} \qquad (1)$$

where ρ_p is the particle density, V_o is the average air velocity in the nozzle throat, C is the slip correction, D_p is the particle diameter, μ is the fluid viscosity, and W is the nozzle diameter.

In Figures 6.1 to 6.13 the parameter $\hat{G}$ is defined as

$$\hat{G} = 1/Fr = gw/V_o{}^2 \qquad (2)$$

where Fr is the Froude number, W is the nozzle diameter, V_o is the average fluid velocity at the nozzle throat and g is the gravitational acceleration. The Froude number is a dimensionless term derived from the dimensionless particle motion equation when gravitational forces on the particle are considered (25).

As shown in equation 2, $\hat{G}$ is a function of the gravitational acceleration and the impactor parameters W and V_o. Although the particle size is not in the definition of $\hat{G}$ as may be expected, the cut off size of an impactor stage is dependent upon W and V_o. Larger particle cut sizes in general are obtained with large W and small V_o. Therefore, impaction stages designed for large particle cut sizes will correspond to the large $\hat{G}$ values in Figure 6.1 to 6.13. Since the efficiency curves in these figures shift to smaller values of St as $\hat{G}$ increases, the cut size of an impactor will be shifted to smaller sizes if gravity is considered as compared to a theory which ignores gravitational forces.

6.4 Summary

The theory developed to predict particle collection characteristics of inertial impactors has been revised. The revisions include refinements of the grid used in the numerical calculations, inclusion of ultraStokesian equations for the drag of the particle, use of the physical size of the particle and the inclusion of the gravitational force on the particle. Each of these refine-

Table 6.1
Summary of Impactor Cases for Which Theoretical Analyses were Performed

Reynolds Number (Re)	Figure Numbers of Corresponding Efficiency Curves for S/W of 0.5	1	2	5
10	-	6.1	-	-
100	6.2	6.3	6.4	-
500	-	6.5	-	-
1,500	-	6.6	-	-
3,000	6.7	6.8	6.9	6.10
10,000	6.11	6.12	6.13	-

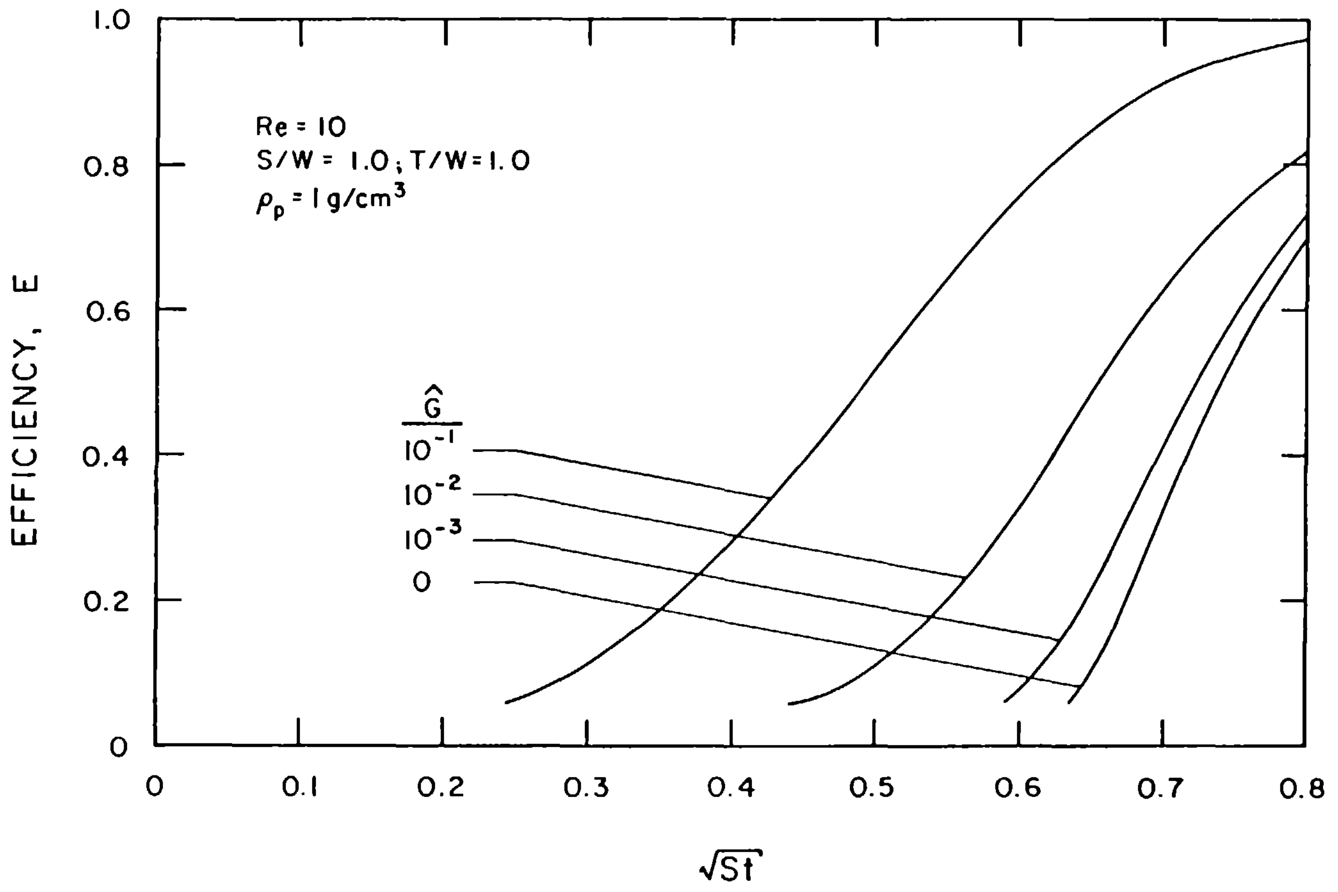

Figure 6.1. Effect of gravity on round impactor efficiency curves for Re=10 and S/W=1.0.

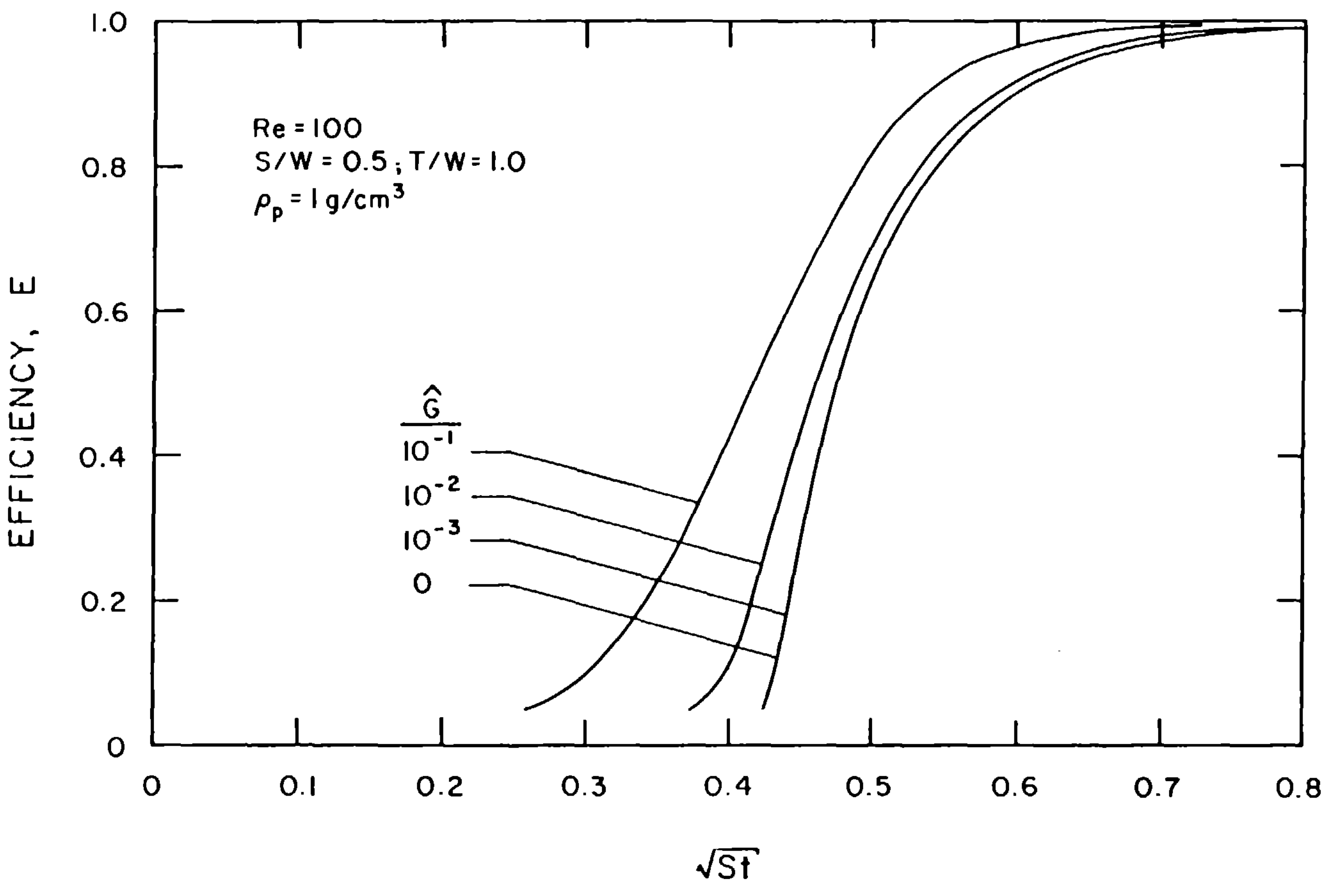

Figure 6.2. Effect of gravity on round impactor efficiency curves for Re=100 and S/W=0.5.

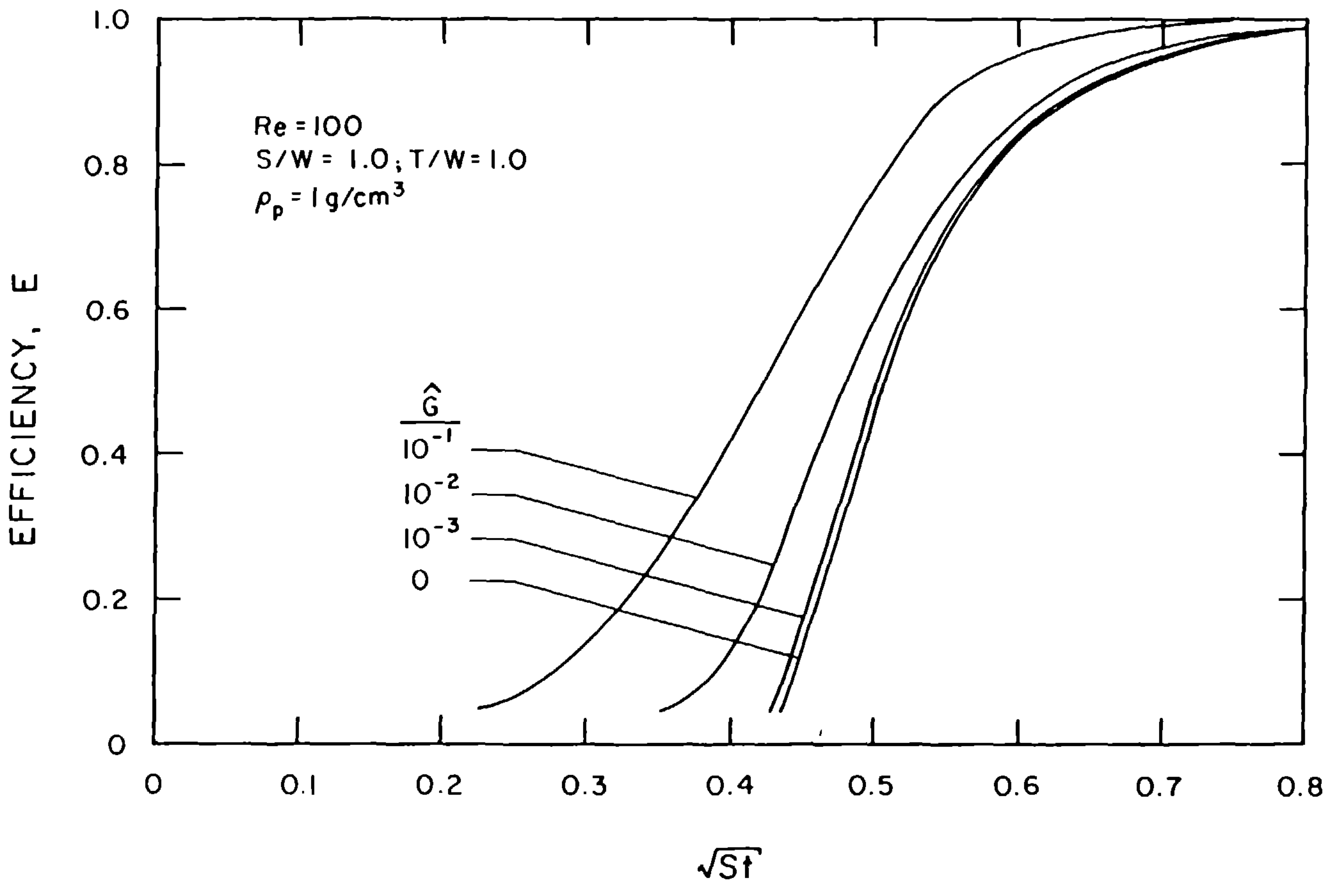

Figure 6.3. Effect of gravity on round impactor efficiency curves for Re=100 and S/W=1.0.

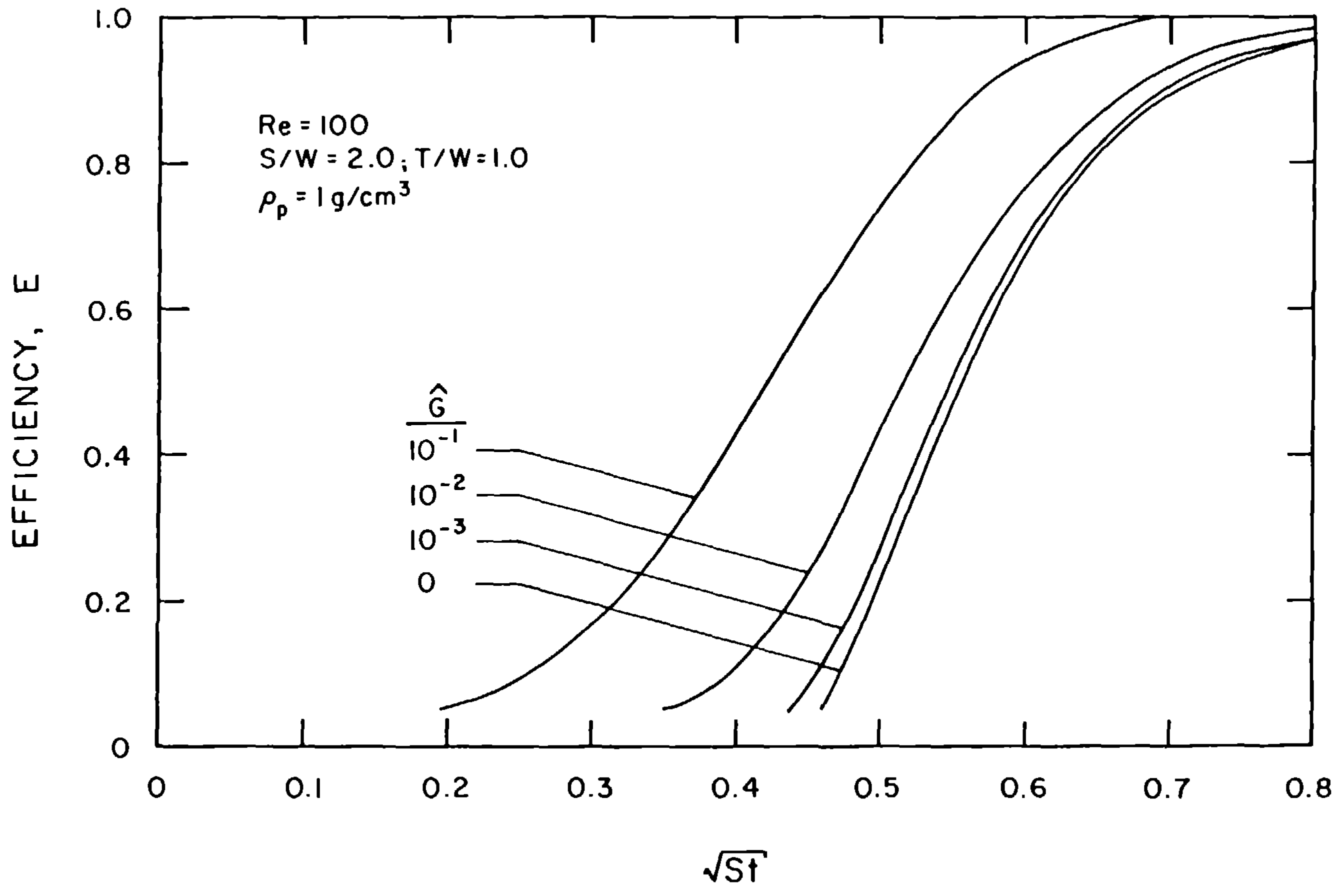

Figure 6.4. Effect of gravity on round impactor efficiency curves for Re=100 and S/W=2.0.

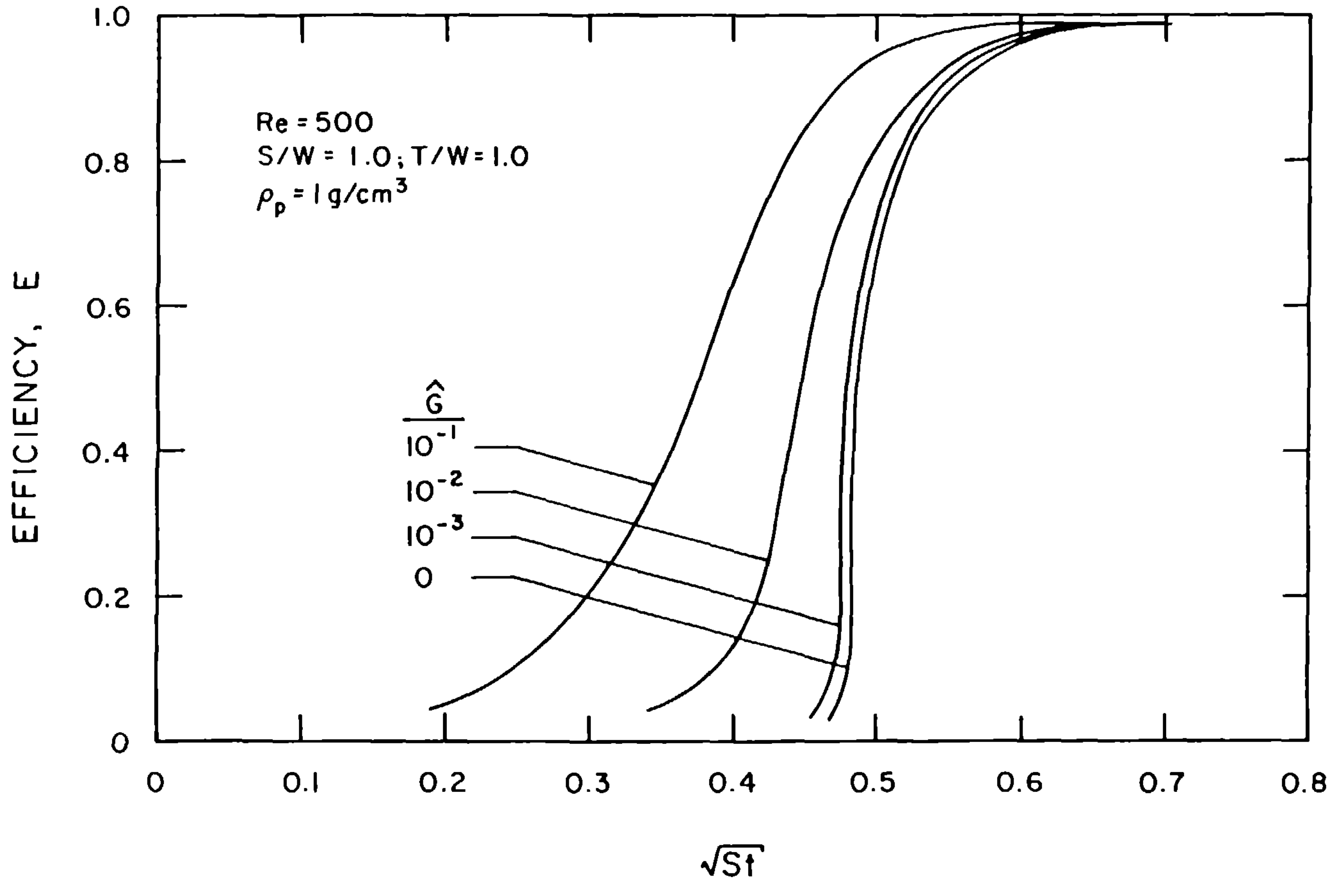

Figure 6.5. Effect of gravity on round impactor efficiency curves for Re=500 and S/W=1.0.

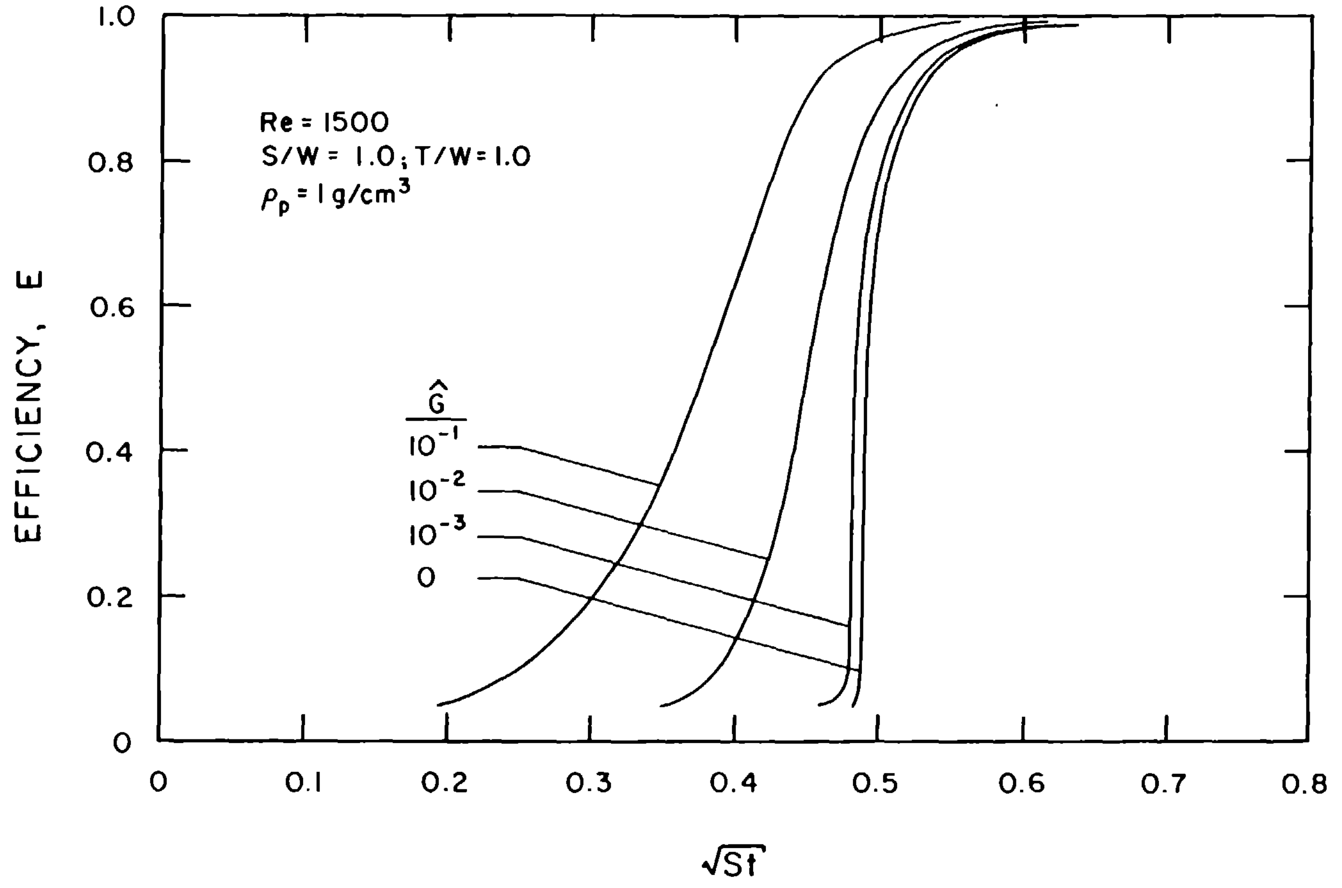

Figure 6.6. Effect of gravity on round impactor efficiency curves for Re=1500 and S/W=1.0.

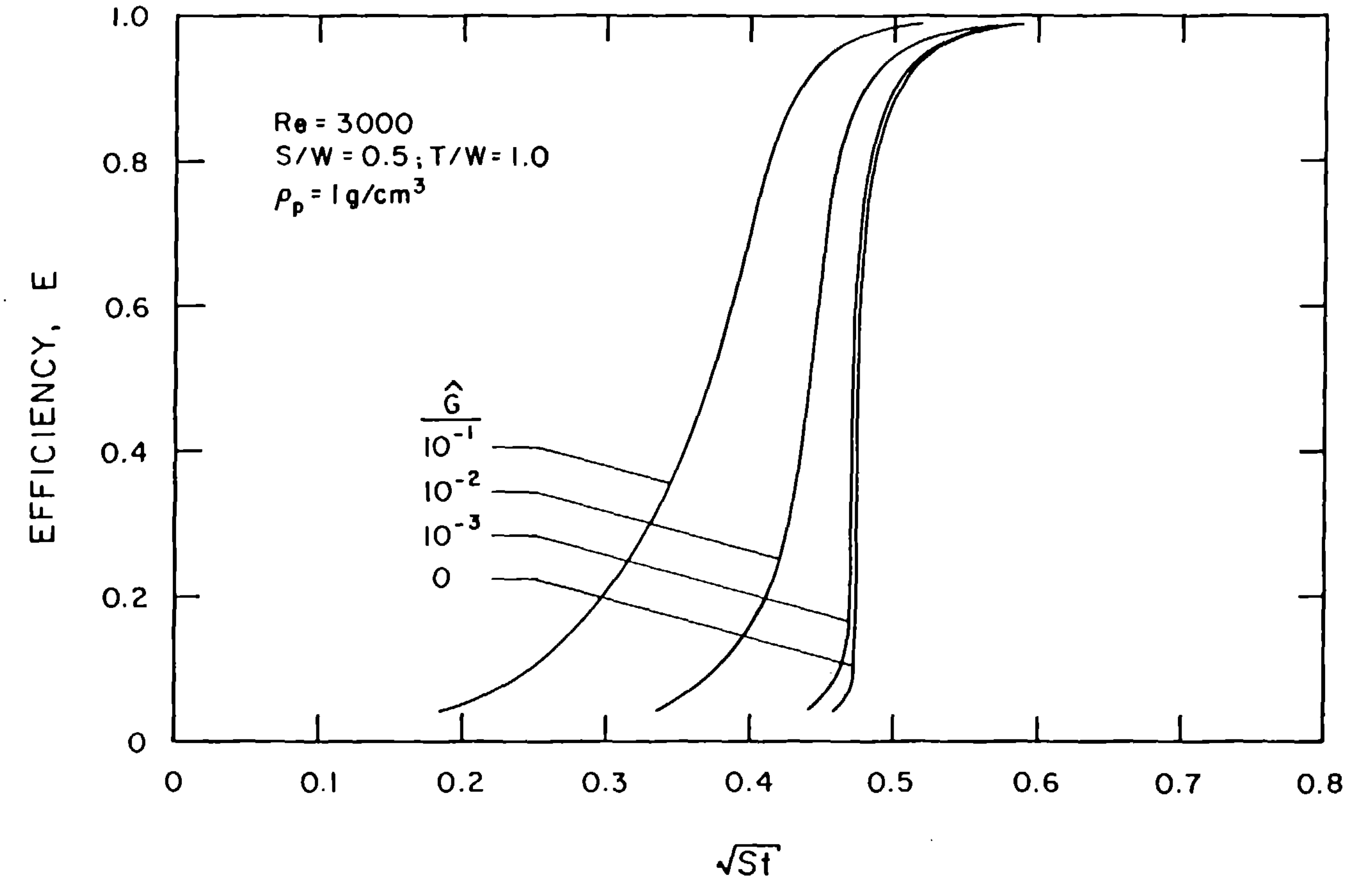

Figure 6.7. Effect of gravity on round impactor efficiency curves for Re=3000 and S/W=0.5.

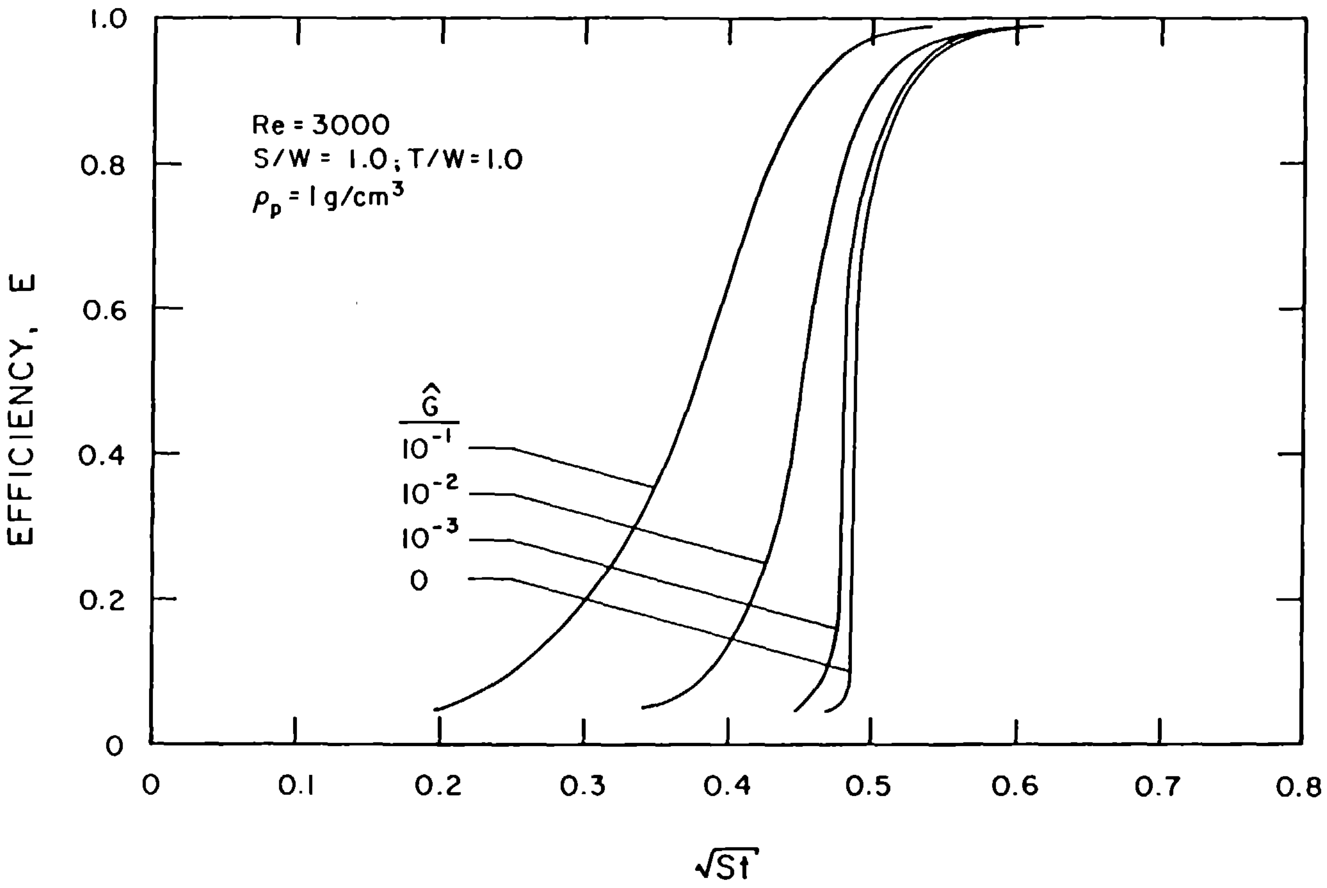

Figure 6.8. Effect of gravity on round impactor efficiency curves for Re=3000 and S/W=1.0.

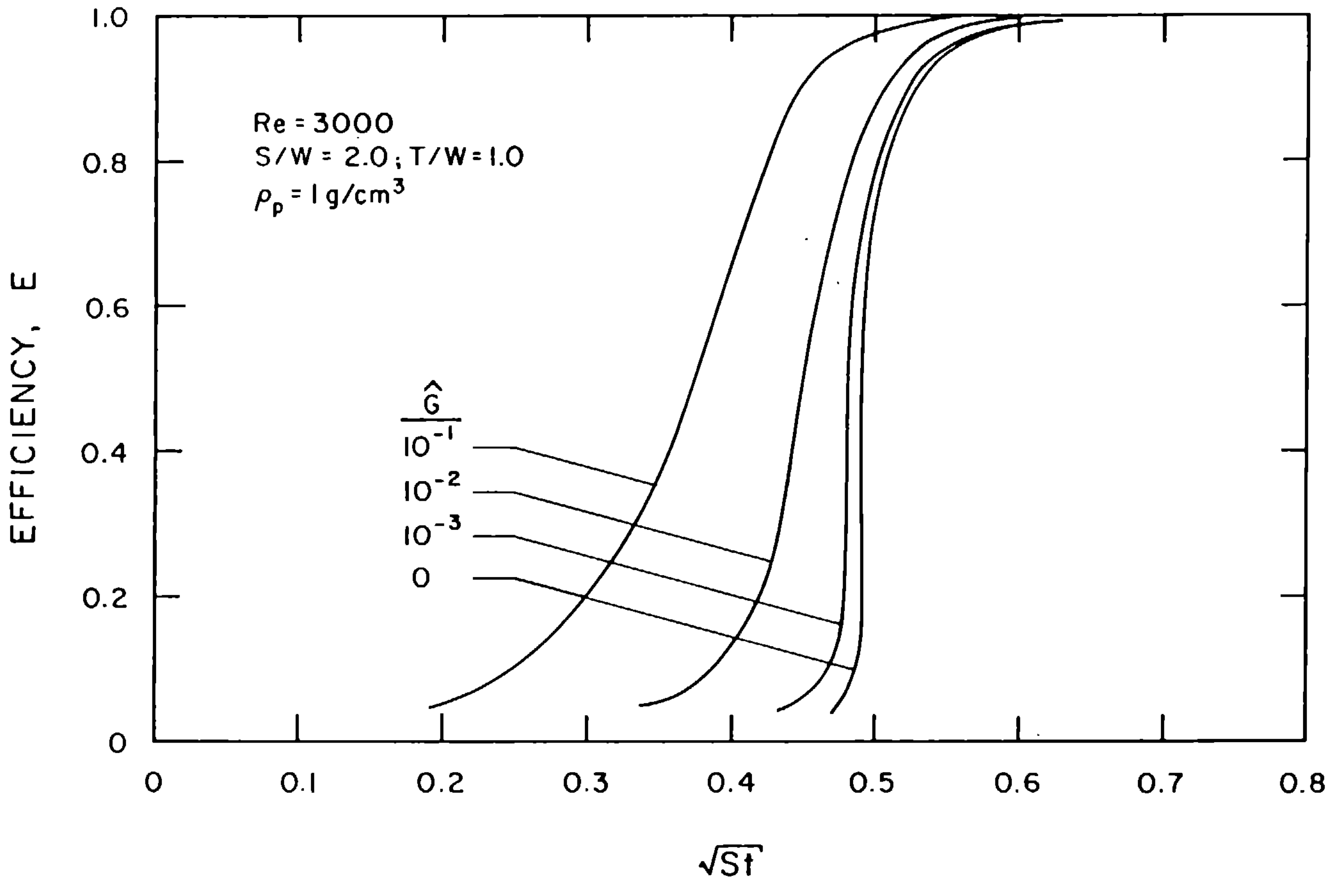

Figure 6.9. Effect of gravity on round impactor efficiency curves for Re=3000 and S/W=2.0.

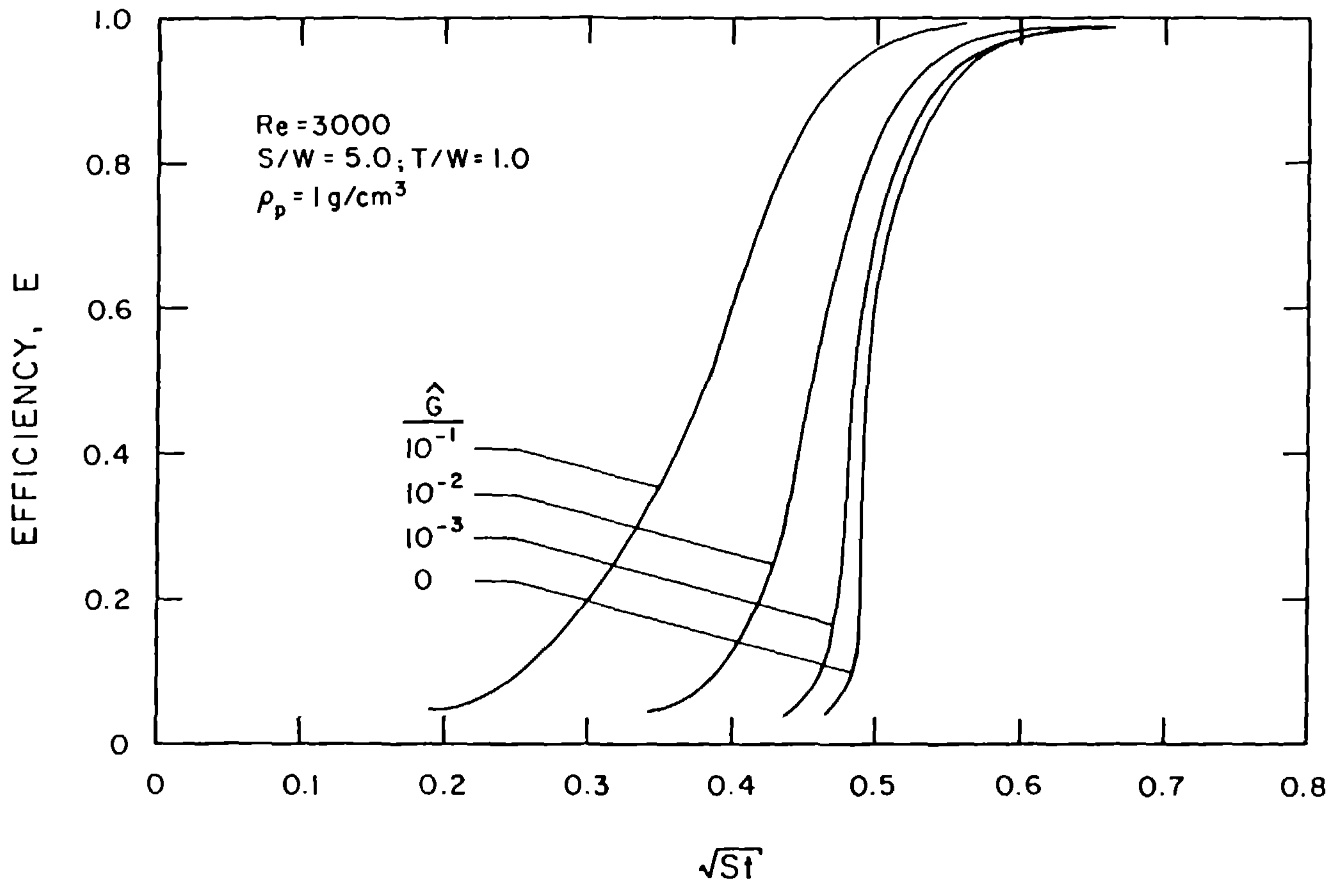

Figure 6.10. Effect of gravity on round impactor efficiency curves for Re=3000 and S/W=5.0.

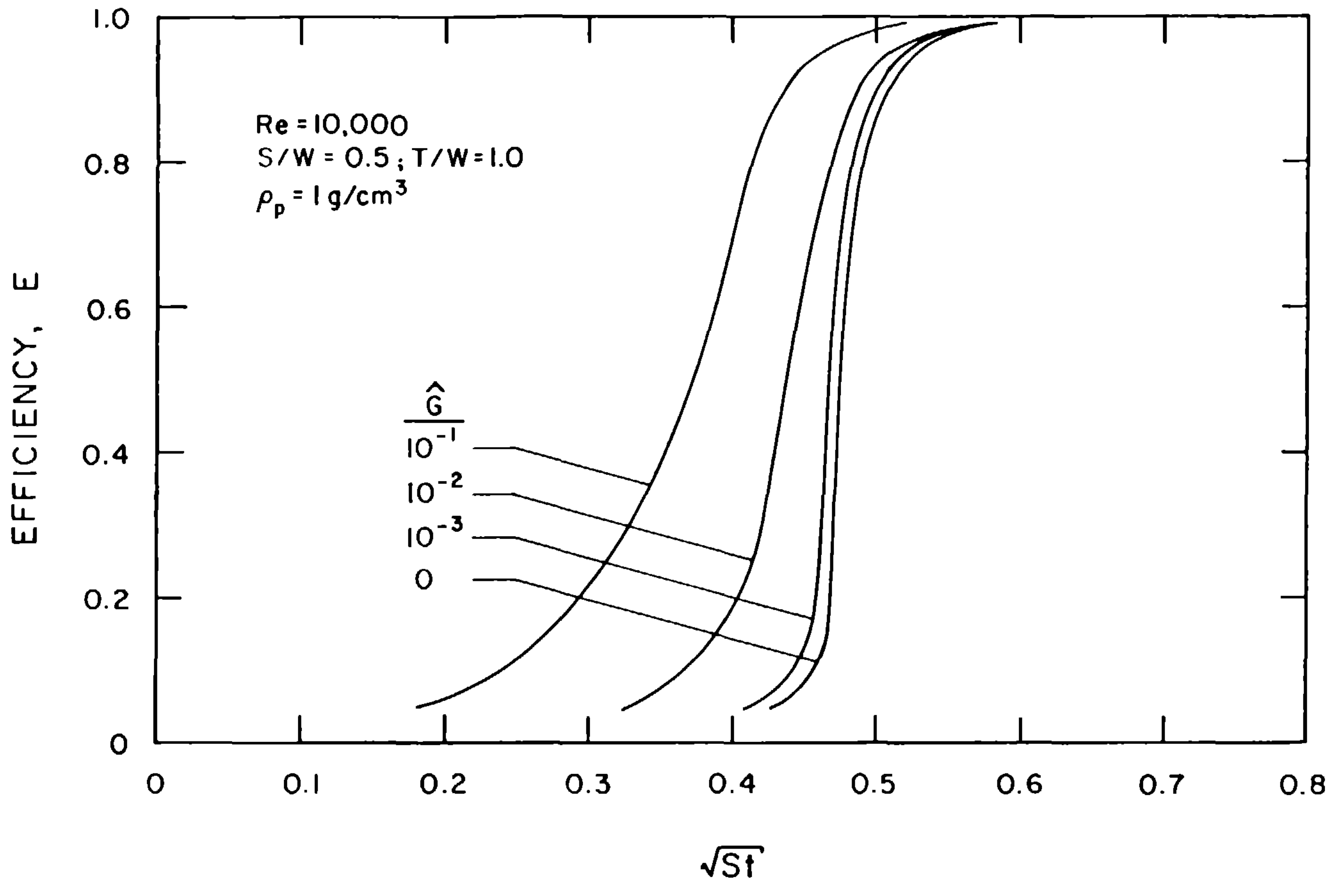

Figure 6.11. Effect of gravity on round impactor efficiency curves for Re=10,000 and S/W=0.5.

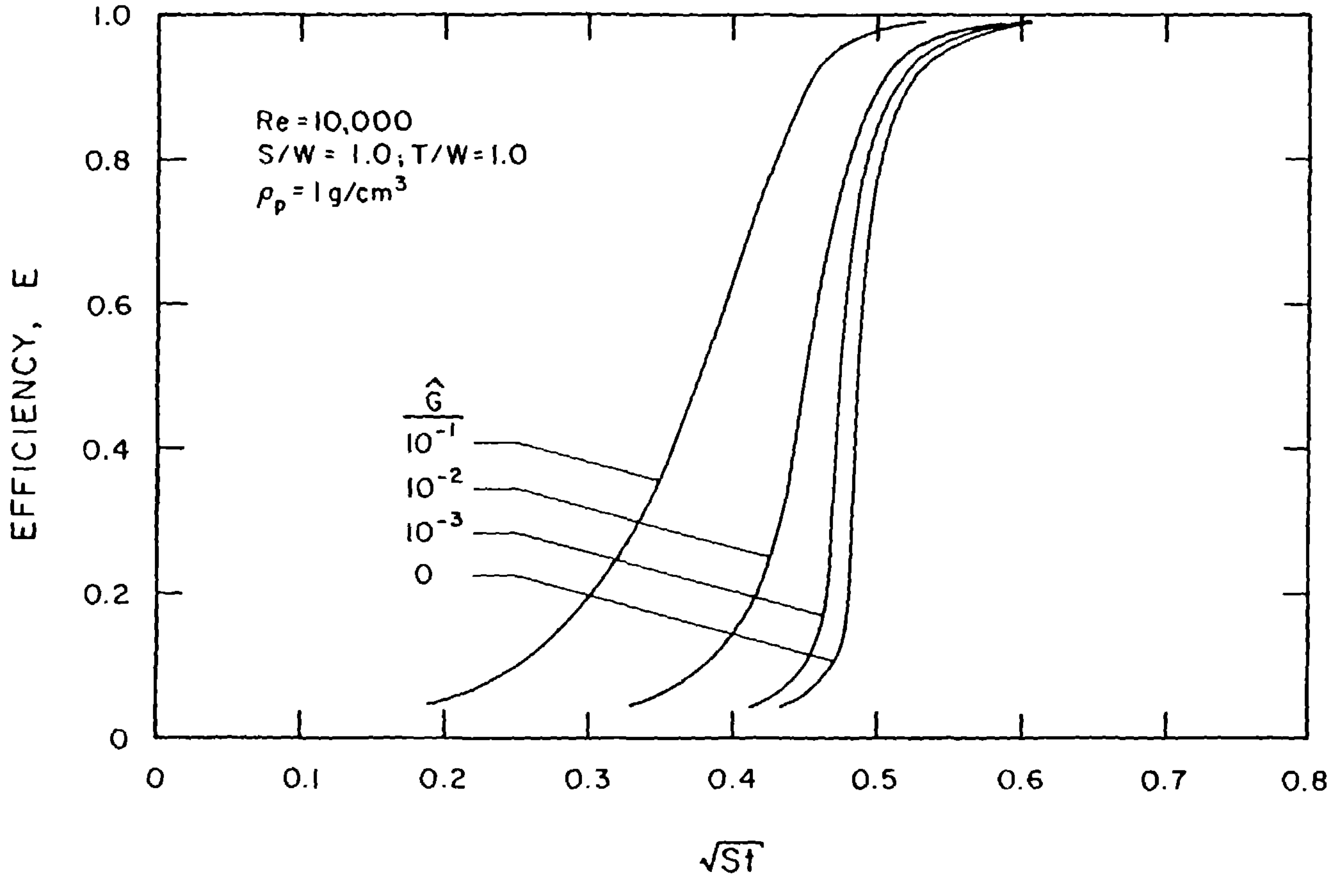

Figure 6.12. Effect of gravity on round impactor efficiency curves for Re=10,000 and S/W=1.0.

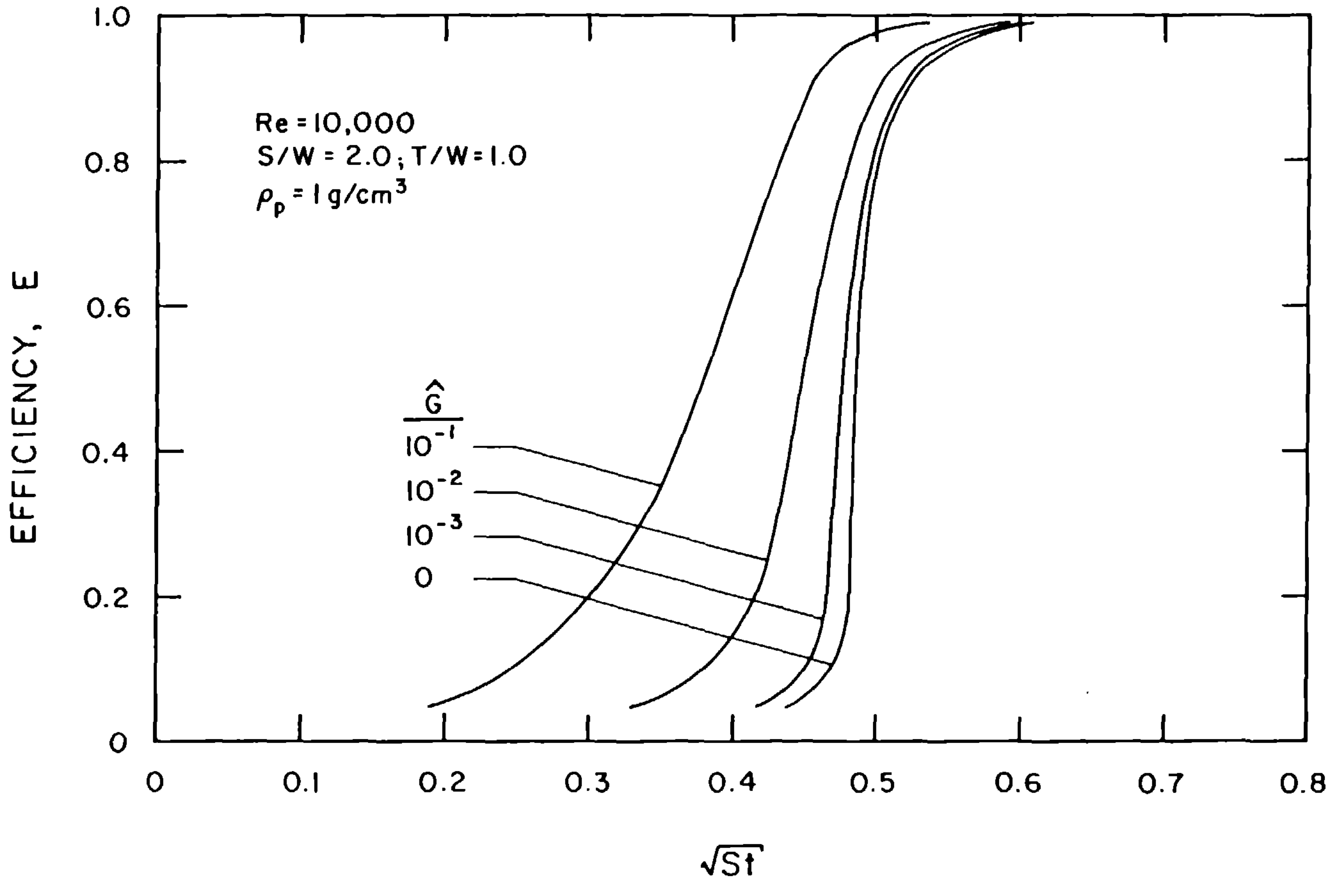

Figure 6.13. Effect of gravity on round impactor efficiency curves for Re=10,000 and S/W=2.0.

ments, while initially thought to be of secondary importance, resulted in modifications to the particle collection curves which now more closely resemble experimentally determined results. In particular, the modified theory now predicts a tail in the efficiency curve at the low efficiency range and a shift in the collection efficiency curves to smaller particle sizes for the case of large $\hat{G}$. The latter shift becomes more pronounced with increasing particle cutoff size of an impactor. While no experimental data were obtained during this contract, these changes in theory were successful in qualitatively explaining the discrepancy between the original theory and experiment results previously reported by the authors and other researchers.

CHAPTER 7

PREPARATION OF DIESEL/COAL DUST SAMPLES

7.1 Introduction

Under the category of technical assistance, filter samples were prepared with known amounts of deposited diesel and coal dust particulate matter. These samples were subsequently used by another Bureau of Mines contractor who was evaluating a Raman scattering analysis technique for quantitatively determining the amount of diesel particle matter in a sample containing both respirable coal dust and diesel particulate matter.

7.2 Sample Preparation

A schematic diagram of the experimental test set-up is shown in Figure 7.1 The source of the diesel particles was a 1980 Volkswagen Rabbit diesel engine which was operated at 2,000 rpm and 23 ft/lbs torque. The fuel used was Texaco No. 2 diesel. The respirable coal dust was obtained by aerosolizing Illinois No. 6 coal dust with a TSI Model 3400 fluidized bed dust generator. The aerosol was passed through a 0.5 inch HASL cyclone which was placed at the exit of the fluidized bed to remove the large nonrespirable particles. The aerosol samples were collected on Pallflex TX40HI20WW filters.

The diesel/coal dust samples were obtained using the following test procedure. The diesel exhaust and the coal dust aerosol flows, as shown in Figure 7.1, were divided with one stream from each combined so as to obtain a mixed aerosol. Filter samplers collected the particulate matter flowing in each of the three streams. Two of the filters were used to determine the mass concentration in the coal dust and diesel exhaust streams, respectively. The third filter was used to collect the mixture of coal and diesel exhaust particles. For each test, all three samplers concurrently collected particulate matter for the same sampling time. The fraction of diesel particulate matter in the mixed flow was controlled by varying the relative flow rates of the diesel and coal dust aerosol in the mixed flow. Both the diesel and coal dust aerosol concentrations from their respective generators were kept constant. The fraction of diesel aerosol in the mixed sample was calculated as follows:

$$\text{diesel fraction} = \frac{M_d}{M_m} \, \frac{Q_m - Q_{fb} + Q_c}{Q_d}$$

where M_d and M_m are amount of particulate matter collected by the diesel and mixed aerosol samplers respectively and Q_m, Q_d and Q_c are the flow rates of the mixed, diesel and coal dust samplers, respectively, and Q_{fb} the flow rate through the fluidized bed dust generator. The uncertainty in the quantity of techniques based on the uncertainties in the flow and mass measurements.

Five sets of filter samples with approximately three runs in each set were obtained. The fraction of diesel exhaust in each set was approximately 0, 5, 20, 40, and 100%. The data for these five sets of filter samples are shown in Table 7.1 The calculated fraction of diesel aerosol together with the estimated relative error is listed for each sample. The error in all cases is equal to or less than 5.2%. The absolute amounts of deposited diesel aerosol and total particulate matter are also given for each sample.

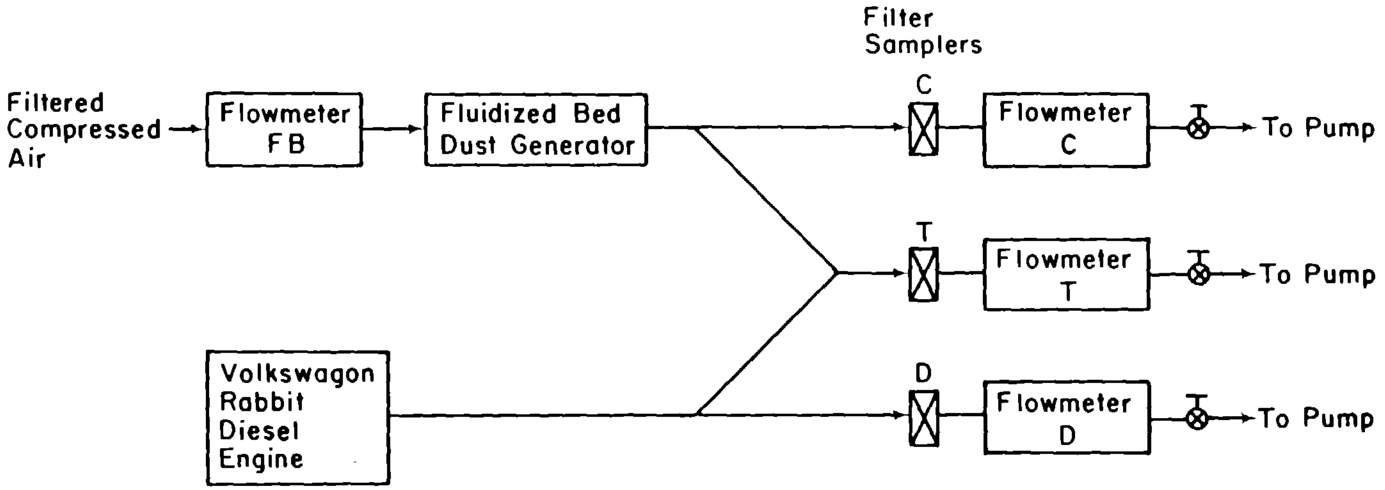

Figure 7.1. Schematic diagram of the test setup used to obtain the diesel/coal dust samples.

Table 7.1

Summary of Diesel/Coal Filter Samples

Sample Identification Number	Diesel Fraction, % % Diesel	RELATIVE ERROR %	Deposited Mass: Diesel, mg	Deposited Mass: Total, mg
A-1	36.4	2.8	1.157	3.179
A-2	38.7	2.9	1.075	2.777
A-3	39.8	2.7	1.197	3.010
A-4	44.9	2.4	2.036	4.537
B-1	6.96	3.0	0.621	8.916
B-2	5.35	5.2	0.187	3.495
B-3	5.56	4.1	0.264	4.747
C-1	19.9	3.1	0.941	4.734
C-2	22.9	3.6	0.7	3.103
C-3	22.2	3.4	0.783	3.521
D-1	100	---	4.928	-----
D-2	100	---	4.250	-----
D-3	100	---	3.469	-----
E-1	0.0	---	-----	5.265
E-2	0.0	---	-----	8.892
E-3	0.0	---	-----	7.235

REFERENCES

1. Marple, V. A. and K. L. Rubow, "An Aerosol Chamber for Instrument Evaluation and Calibration," Am. Ind. Hyg. Assoc. J. 44:361-367 (1983).

2. Rubow, K. L. and V. A. Marple, "An Instrument Evaluation Chamber: Calibration of Commercial Photometers," Aerosols in the Mining and Industrial Work Environment, V. A. Marple and B. Y. H. Liu, eds., pp. 777-798 (1983).

3. Marple, V. A., "Simulation of Respirable Penetration Characteristics by Inertial Impaction," J. Aerosol Sci. 9:125-134 (1978).

4. Lippmann, M., "Size-Selective Health Hazard Sampling," Air Sampling Instruments Sixth Edition, P. S. Lioy, ed., American Conference of Governmental Industrial Hygienists, Cincinnati, Ohio (1983).

5. Lippmann, M., "Size-Selective Sampling for Inhalation Hazard Evaluations," in Fine Paricles: Aerosol Generation, Measurement, Sampling, and Analysis (B. Y. H. Liu, ed.), pp. 287-310, Academic Press, New York (1976).

6. Marple, V. A. and K. L. Rubow, "Laboratory Calibration of Large Impactor Nozzles," final report to the University of Florida/CR808606, subcontract to EPA Contract No. CR808606, (January, 1983).

7. Rubow, K. L., V. A. Marple, J. Olin and M. A. McCawley, "A Personal Cascade Impactor: Design, Evaluation and Calibration" to be submitted to Am. Ind. Hyg. Assoc. J.

8. Marple, V. A. and J. E. McCormack, "Personal Sampling Impactors with Respirable Aerosol Penetration Characteristics," Am. Ind. Hyg. Assoc. J. 44:916-922 (1983).

9. Marple, V. A. and K. L. Rubow, "Impactors for Respirable Dust Sampling," Aerosols in the Mining and Industrial Work Environment, V. A. Marple and B. Y. H. Liu, eds., Vol. 3, pp. 847-860 (1983).

10. Marple, V. A. and K. L. Rubow, "Instruments and Techniques for Dynamic Particle Size Measurement of Coal Dust," final report on Contract No. USDI/BOM H0177025 (January, 1981).

11. Thompson, E. M., H. N. Treaftis, T. F. Tomb, A. I. Beckert and A. I. Gero, "Laboratory Evaluation of Instantaneous Reading Dust Monitors," Am. Ind. Hyg. Assoc. J. 42:191-197 (1981).

12. Kuusisto, P., "Evaluation of the Direct Reading Instruments for the Measurment of Aerosols," Am. Ind. Hyg. Assoc. J. 44:863-874 (1983).

13. Marple, V. A. and K. L. Rubow, "Dynamic Particle Size Measurement of Coal Dust," U. S. Bureau of Mines Contract No. H0133095 Final Report (Feb., 1977).

14. Dave, J. V., "Scattering of Electromagnetic Radiation by a Large, Absorbing Sphere," IBM J. Res. Develop., 302-313 (May, 1969).

15. Dave, J. V., "Subroutines for Computing the Parameters of the Electromagnetic Radiation Scattered by a Sphere," Rept. No. 320-3237, IBM Scientific Center, Palo Alto, CA (May, 1968).

16. Irvine, W. M. and J. B. Pollack, "Infrared Optical Properties of Water and Ice Spheres," Icarus 8:324-360 (1968).

17. Liu, B. Y. H., D. Y. H. Pui and K. L. Rubow, "Characteristics of Air Sampling Filter Media," Aerosols in the Mining and Industrial Work Environment, V. A. Marple and B. Y. H. Liu, eds., pp. 983-1038 (1983).

18. Agarwal, J. K. and B. Y. H. Liu, "A Criterion for Accurate Aerosol Sampling in Calm Air," Am. Ind. Hyg. Assoc. J. 41:191-197 (1980).

19. Cecala, A. B., J. C. Volkwein. R. J. Timko and K. L. Williams, "Velocity and Orientation Effects on the 10 mm Dorr-Oliver Cyclone," U. S. Bureau of Mines RI 8764 (1983).

20. Caplan, K. J., L. J. Doemeny and S. D. Sorenson, "Performance Characteristics of the 10 mm Respirable Mass Sampler: Part II - Coal Dust Studies," Am. Ind. Hyg. Assoc. J. 38:162-173 (1977).

21. Marple, V. A. and K. L. Rubow, "A Portable Optical Particle Counter System For Measuring Dust Aerosols," Am. Ind. Hyg. Assoc. J. 39:210-218 (1978).

22. Marple, V. A. and K. L. Rubow, "Aerodynamic Particle Size Calibration of Optical Particle Counters," J. Aerosol Sci. 7:425-433 (1976).

23. Belyaev, S. P. and L. M. Levin, "Techniques for Collection of Representative Aerosol Samples," J. Aerosol Sci. 5:325-338 (1974).

24. Marple, V. A. and D. Rader, "A Study of the Effects of Anisokinetic Sampling," EPA Final Report CR 808319-01-02 (September, 1983).

25. Fuchs, N. A. The Mechanics of Aerosols, p. 139, Pergamon Press, Oxford (1964).

APPENDIX A

IMPACTORS FOR RESPIRABLE DUST SAMPLING

V. A. Marple and K. L. Rubow
Particle Technology Laboratory
Mechanical Engineering Department
University of Minnesota
Minneapolis, MN 55455

Published in:

Aerosols in the Mining and Industrial Environment
Volume 3: Instrumentation
V. A. Marple and B. Y. H. Liu, eds.

Ann Arbor Science Publishers
Ann Arbor, Michigan
1983

ABSTRACT

The technique of using impactors with penetration characteristics that approximate respirable penetration criteria have been employed in several newly developed devices. One device is a personal sampler operating at a flow rate of 2 l/min. The sampler can be designed with penetration characteristics approximating either the ACGIH or BMRC respirable criteria. Another device, a dust generator/respirable particle separator, determines the quantity of respirable size particles in a bulk powder sample. This device incorporates an impactor operating at a flow rate of 40 l/min with respirable characteritics approximating the ACGIH respirable criteria. A third device is an impactor used for determining the concentration of respirable dust in an aerosol test chamber. The impactor, operating at 28 l/min, is designed so the nozzle plate can be easily changed to provide for sampling respirable dust by either the ACGIH or BMRC criteria depending upon the instruments under evaluation in the chamber.

INTRODUCTION

In determining hazards from inhaled aerosol particles, the quantity of particles penetrating into the alveolated regions of the lung, defined as the respirable dust, is of primary importance. Due to removal mechanisms of particles in the nasal passages and the airways of the lungs, the quantity of respirable particles in an aerosol is dependent on the size distribution of the particles. Various relationships between the percent particle penetration to the alveolated regions of the lung and the aerodynamic diameter of a particle have been postulated. Two widely used respirable curves (Lippmann, 1976) are one defined by the British Medical Research Council (BMRC) and one defined by the American Conference of Governmental Industrial Hygienist Association (ACGIH). The ACGIH curve is a slight variation of an earlier curve defined by the United States Atomic Energy Commission (AEC).

To determine the concentration of respirable particles existing in an aerosol, it is common practice to pass the aerosol through a classifier which removes the large non-respirable particles. The penetrating respirable particles are either collected on a filter and the mass concentration determined gravimetrically or the concentration is measured with some type of automatic reading instrument. Although cyclones or horizontal elutriators have been commonly used as classifiers for respirable particles, as defined by the ACGIH and the BMRC curves, respectively, the use of a new technique utilizing inertial impaction principles has recently been developed as a respirable aerosol classifier (Marple, 1978). This technique is very versatile in that a classifier can be designed to provide the respirable characteristics of either the ACGIH or the BMRC curve at nearly any flow rate. Because of this versatility, the respirable impactor technique has been used for several applications in our Laboratory.

The principle of this technique is to approximate a respirable curve by the cut-off characteristics of a single stage impactor with multiple nozzles of various sizes. As shown in Figure 1, a single stage impactor with three sizes of nozzles would possess cut-off characteristics which approximate the ACGIH respirable curve in three steps. The number of nozzles of each size must be sufficient to pass the quantity of flow dictated by the size of each

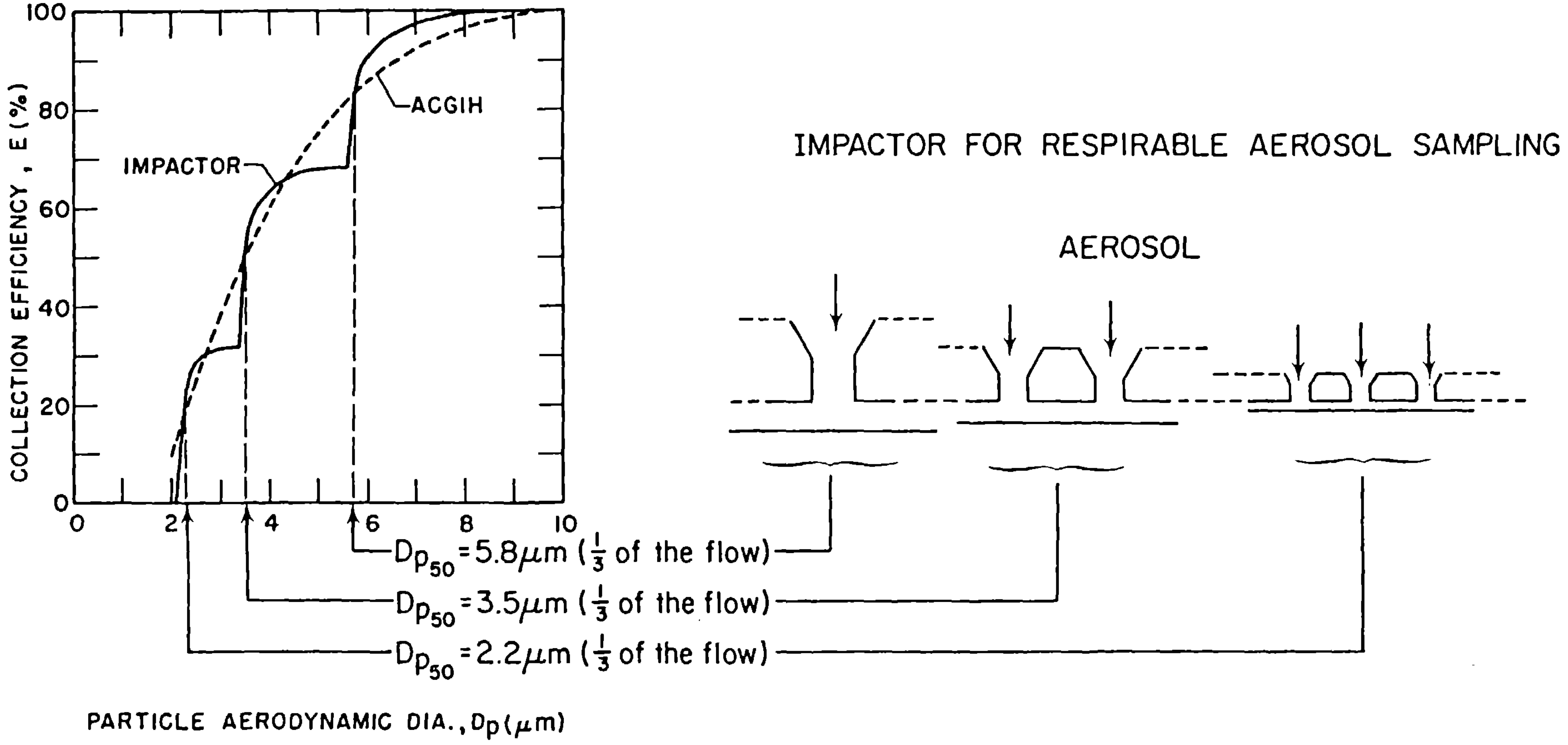

Figure 1. Approximation of the ACGIH respirable curve by a single stage impactor with three nozzle sizes.

step. For example, in Figure 1, there must be enough nozzles of each size to pass one third of the flow.

It has been generally found that two or three cut sizes (steps) are sufficient to approximate the curve. In our laboratory, respirable impactors have been designed and built for flow rates of 2, 28 and 40 l/min for various applications. Table 1 shows the number and sizes of nozzles required for two and three step approximations at these flow rates. For the case of 2 l/min, the design criteria is presented for both the ACGIH and BMRC respirable curves.

Three applications of respirable impactor techniques are described in this paper. These applications include personal samplers, a dust generator/respirable particle separator, and an aerosol test chamber respirable sampler. These impactors are described in the following sections as well as calibration data for several of them.

PERSONAL SAMPLERS

The personal samplers were designed with a flow rate of 2 l/min so as to be compatible with personal sampling pumps. However, personal samplers with larger flow rates could be designed if larger flow rate pumps were used.

Three impactors corresponding to A, B, and D in Table 1 have been built and tested. The impactors were constructed from plastic with nozzle layouts for two and three cut sizes as shown in Figure 2. The impaction plate, also shown in Figure 2, is designed to be attached to the nozzle plate by four pegs. The after-filter and the base plate are those that have been used by Tomb and Treaftis (1975) in a single nozzle impactor. The filter is from a type 457193 MSA filter cassette.

Two types of impaction plates were designed for the impactors. A plastic impaction plate was used in the calibration with liquid droplets. However, where large amounts of solid particles are to be retained upon the impaction plate, an oil impregnated porous impaction plate was used (Reischl and John, 1978). With this impaction plate, oil wicks upward continuously through the deposited particles so as to always present the incoming particles with a fresh oil surface.

Tests of the effectiveness of the oil impregnated impaction plate to reduce particle bounce were conducted with coal dust particles generated in a fluidized bed type of dust generator (Marple, Liu and Rubow, 1978) and sampled by impactor A (Table 1). The generated dust was at a concentration of about 9 mg/m^3 with the respirable fraction being about 2 mg/m^3. This left 7 mg/m^3 to be removed by the impactor. The test was run for a total of 6.5 hours. At 1, 2 and 6.5 hours into the test the impaction plate was removed from the impactor and the deposits inspected. Photographs of the deposits are shown in Figure 3 for the 6.5 hour inspection. The deposits appear to form spikes and in some cases the spikes bend and a new spike grows from the base. This bending of the spikes may have been caused by the removal of the impaction plate from the impactor and may not happen if the impaction plate is not disturbed.

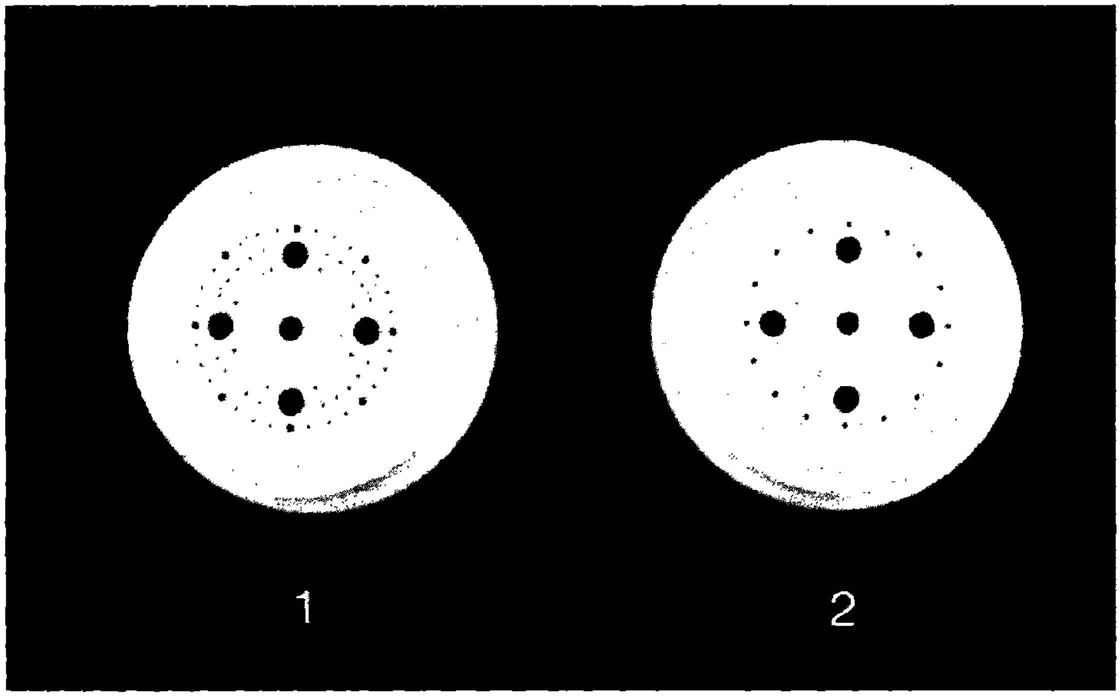

a. Nozzle plates with two (2) and three (1) nozzle sizes. (The four equally spaced large holes are for the impaction plate mounting pegs.)

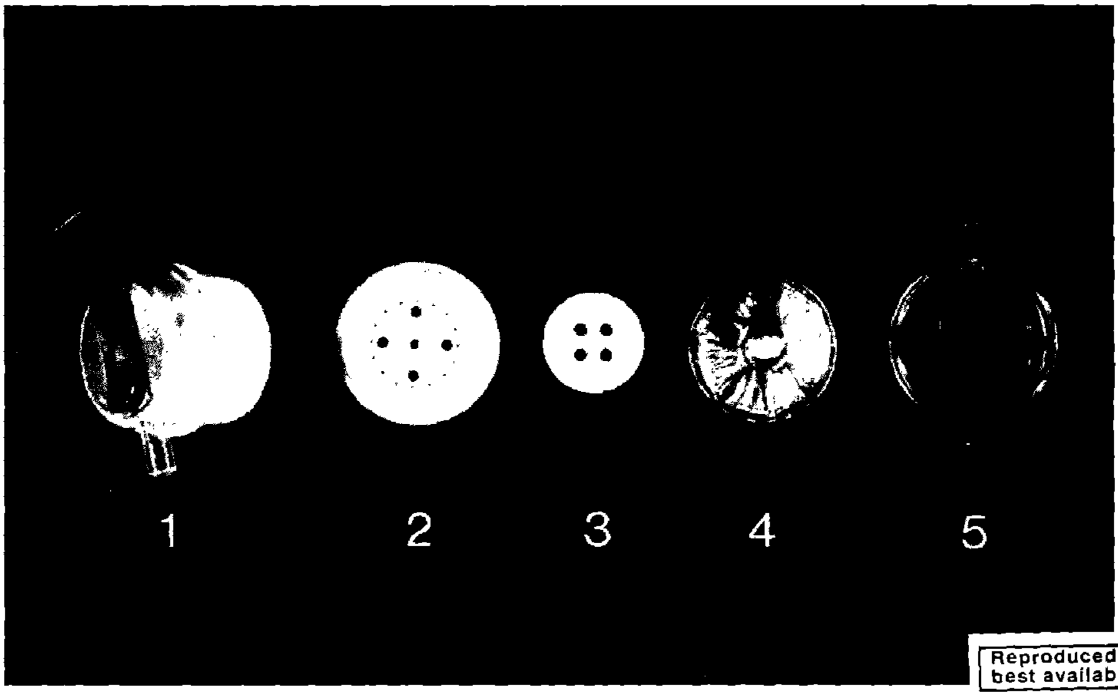

b. Impactor components (1- assembly, 2- nozzle plate, 3- impaction plate, 4- filter, 5- base plate).

Figure 2. Respirable personal sampler.

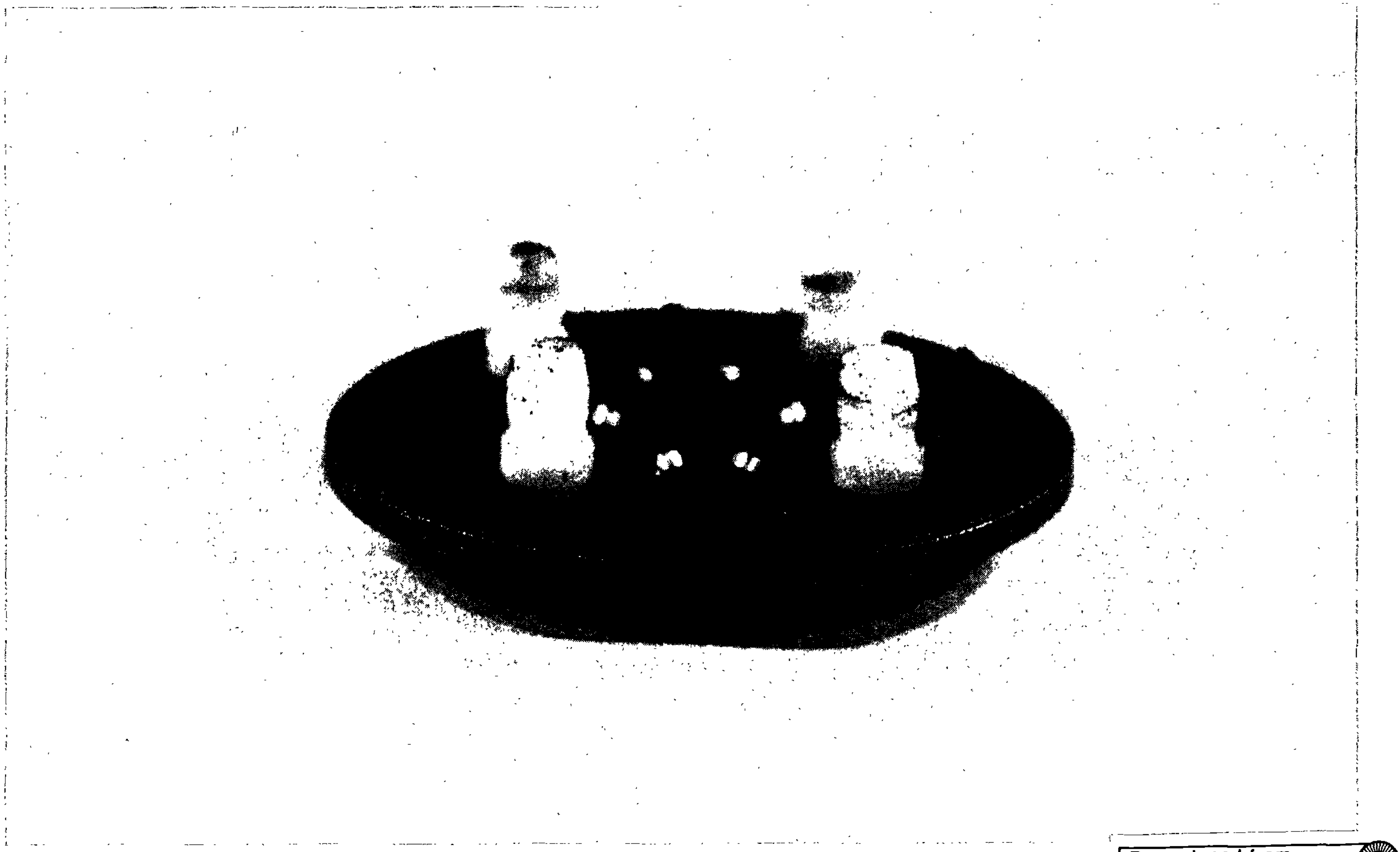

Figure 3. Deposits on the porous impaction plate of impactor A after sampling a coal dust aerosol (9 mg/m^3) for 6.5 hours.

It does not appear that the spikes on the impaction plate had adverse effects on the particle collection efficiency. This was concluded from analysis of the particle size distributions measured upstream and downstream of the impactor with an optical particle counter calibrated specifically to measure the size distribution of coal particles (Marple and Rubow, 1978). Size distributions measured at 0.5, 2.25, 4.0 and 6.5 hours into the test showed no change in the particle collection efficiency curve. This also indicates that the oil soaked porous impaction plate did control particle bounce.

DUST GENERATOR/RESPIRABLE PARTICLE SEPARATOR

The primary objective of the dust generator/respirable particle separator, shown in Figures 4 and 5, is to aerosolize a bulk sample of powder, break-up agglomerates, remove the large, non-respirable particles and collect the respirable particles upon a filter. In operation, the powder is placed in a sample boat, the sample boat is mounted onto a movable boat support plate and the entire assembly placed into the powder pickup chamber. The flow of air up the dust pickup tube picks up the powder from the sample boat and transports it vertically up the tube. The sample boat and support plate can be moved with a rack and pinion so that the entire length of the sample boat will pass beneath the dust pickup tube. At the exit end of the pickup tube, agglomerates are broken up by a high velocity jet flowing across the top of the tube. The deagglomerated particles next pass through a respirable impactor where the large non-respirable particles are removed by impaction and the respirable particles penetrate into a chamber and are collected on a filter. The flow rate through the impactor is 40 l/min.

The respirable impactor in this device is shown in Figure 6 and described as impactor G in Table 1. To ensure that there are no problems with particle bounce and re-entrainment, the impaction plate, also shown in Figure 6, is made of a porous metal which has been saturated with a light oil in the same manner as the personal impactor previously described. However, to eliminate the problem of spiked deposits building up on the impaction plate, the impaction plate is made to rotate at a rate of 0.9 rpm by use of an electric gear motor. Since the nozzles of each size are located at the same radial distances, the deposits appear as rings on the impaction plate.

AEROSOL TEST CHAMBER RESPIRABLE SAMPLER

The aerosol test chamber respirable sampler is designed to provide a means for measuring the quantity of respirable aerosol in an instrument evaluation chamber. The sampler, shown in Figure 7, is similar to the respirable aerosol classifier of the dust generator/respirable particle separator described previously. As was the case for the previous sampler, the nozzles are in concentric circles about the central nozzle and the impaction plate, which is a porous metal surface saturated with a light oil, is rotated by an electric motor.

The operation of this sampler is slightly different than that for the dust generator/respirable particle separator in that the impaction plate is not rotated continously but is moved only periodically. The reason being that when the sampler is in an aerosol test chamber, as shown in Figure 8, operating the electric motor continuously would constitute a heat source which

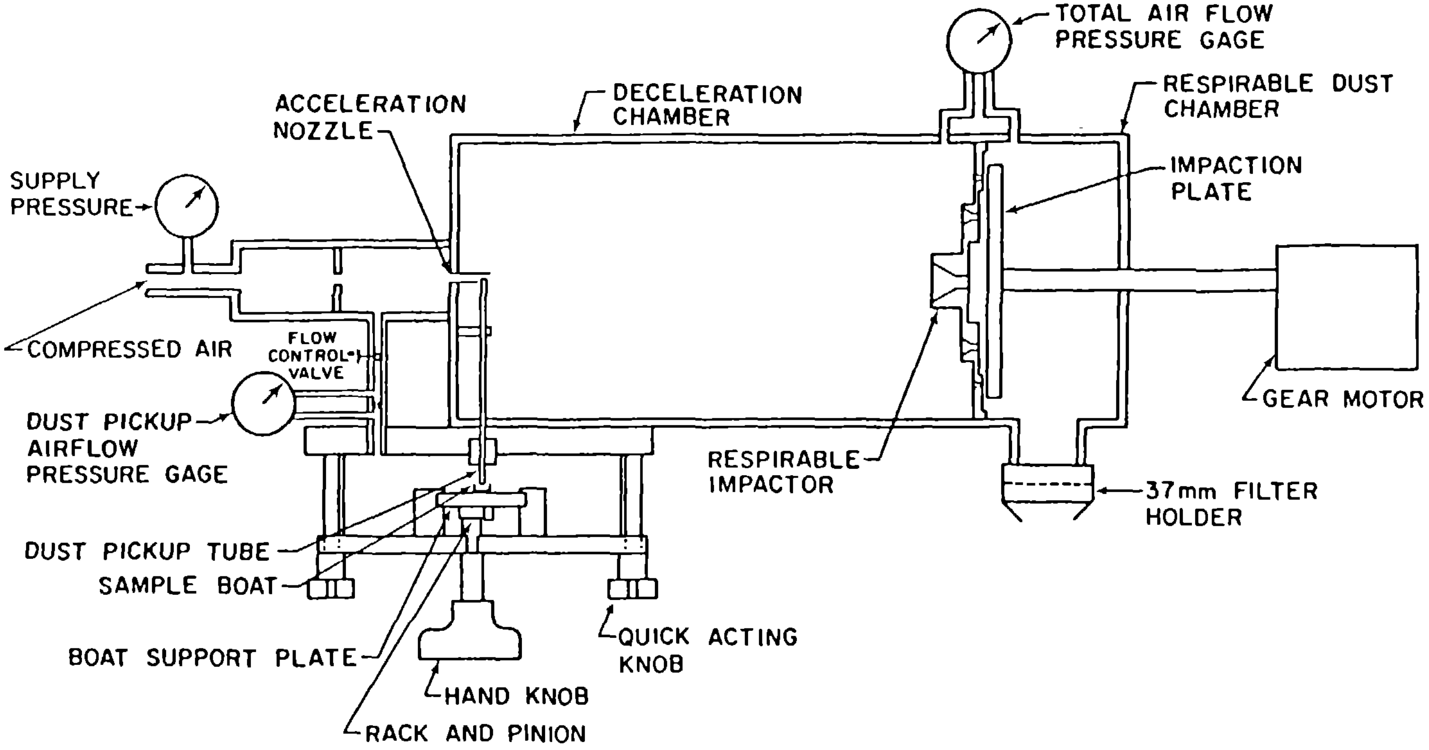

Figure 4. Schematic diagram of dust generator/respirable particle separator.

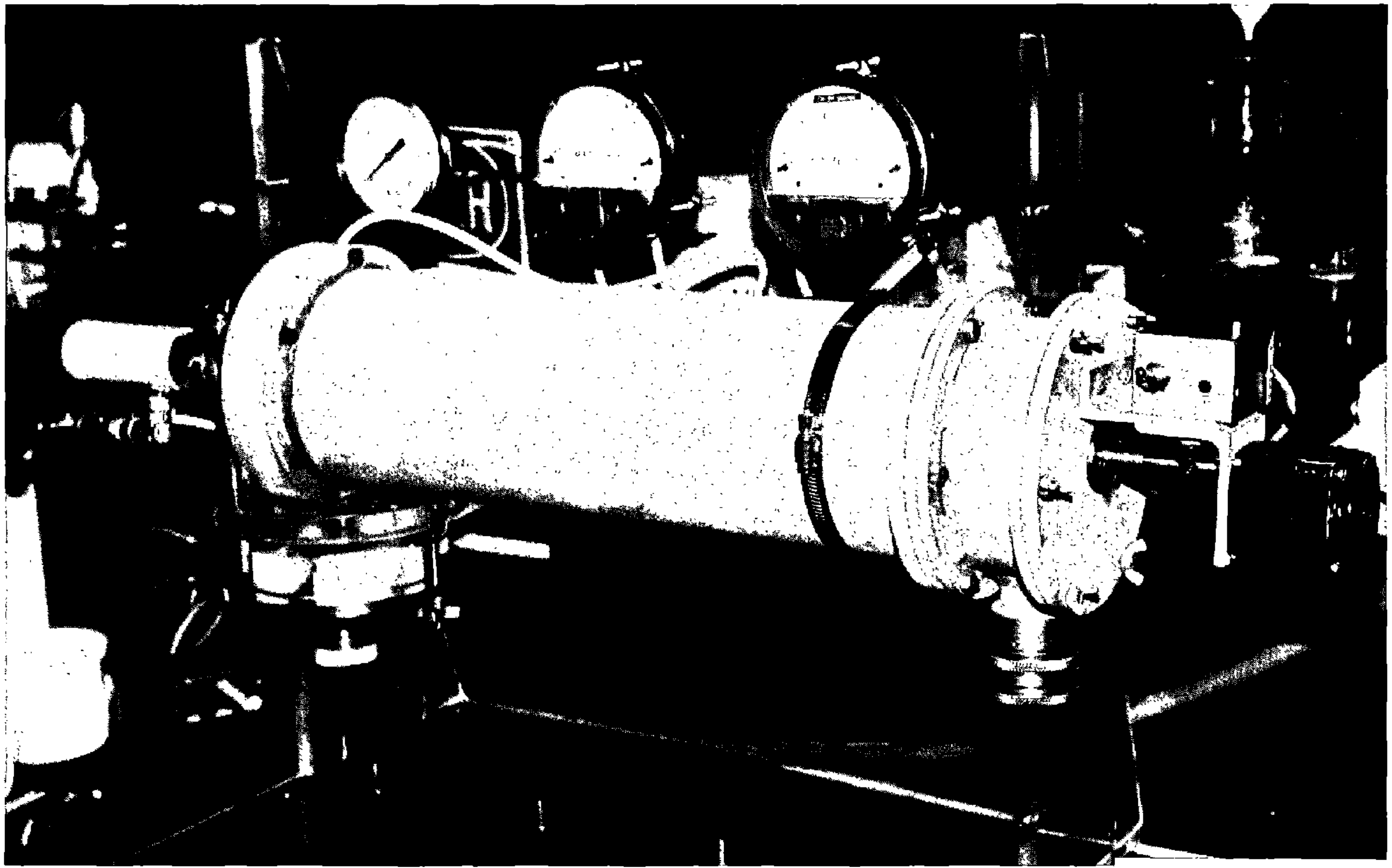

Figure 5. Dust generator/respirable dust separator.

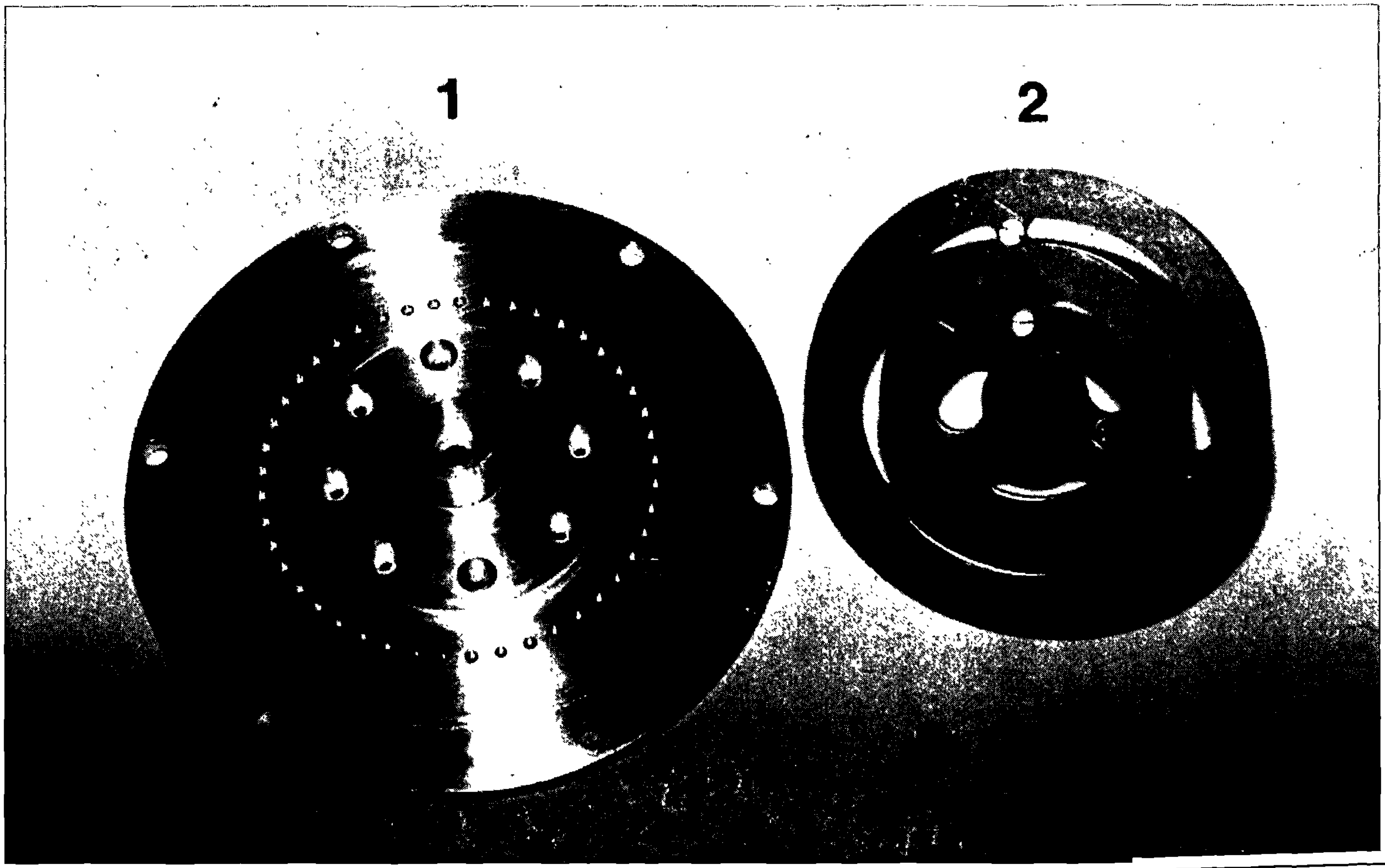

Figure 6. Respirable impactor of the dust generator/respirable particle separator. 1. Nozzle
2. Impaction plate

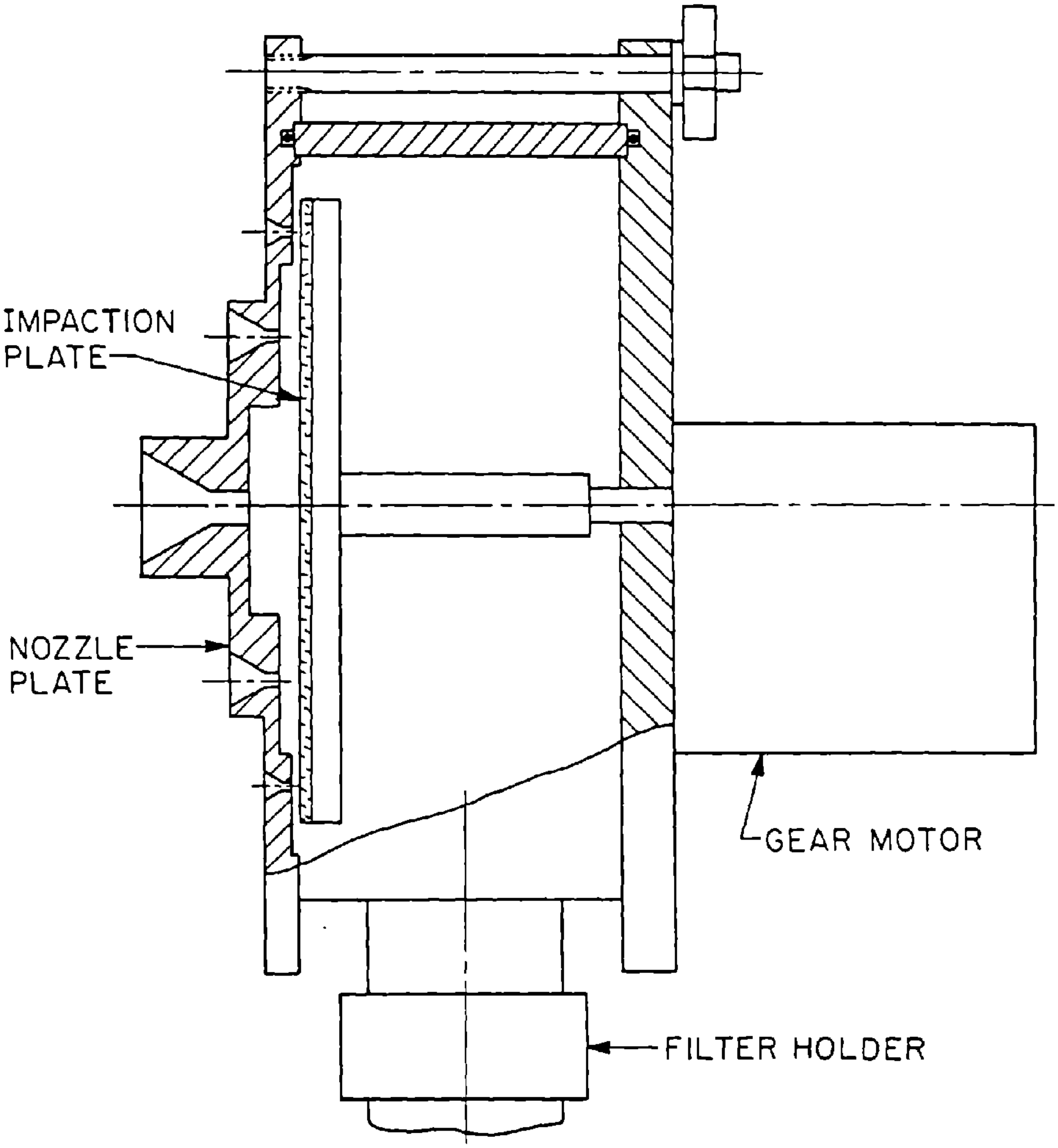

Figure 7. Aerosol test chamber respirable sampler.

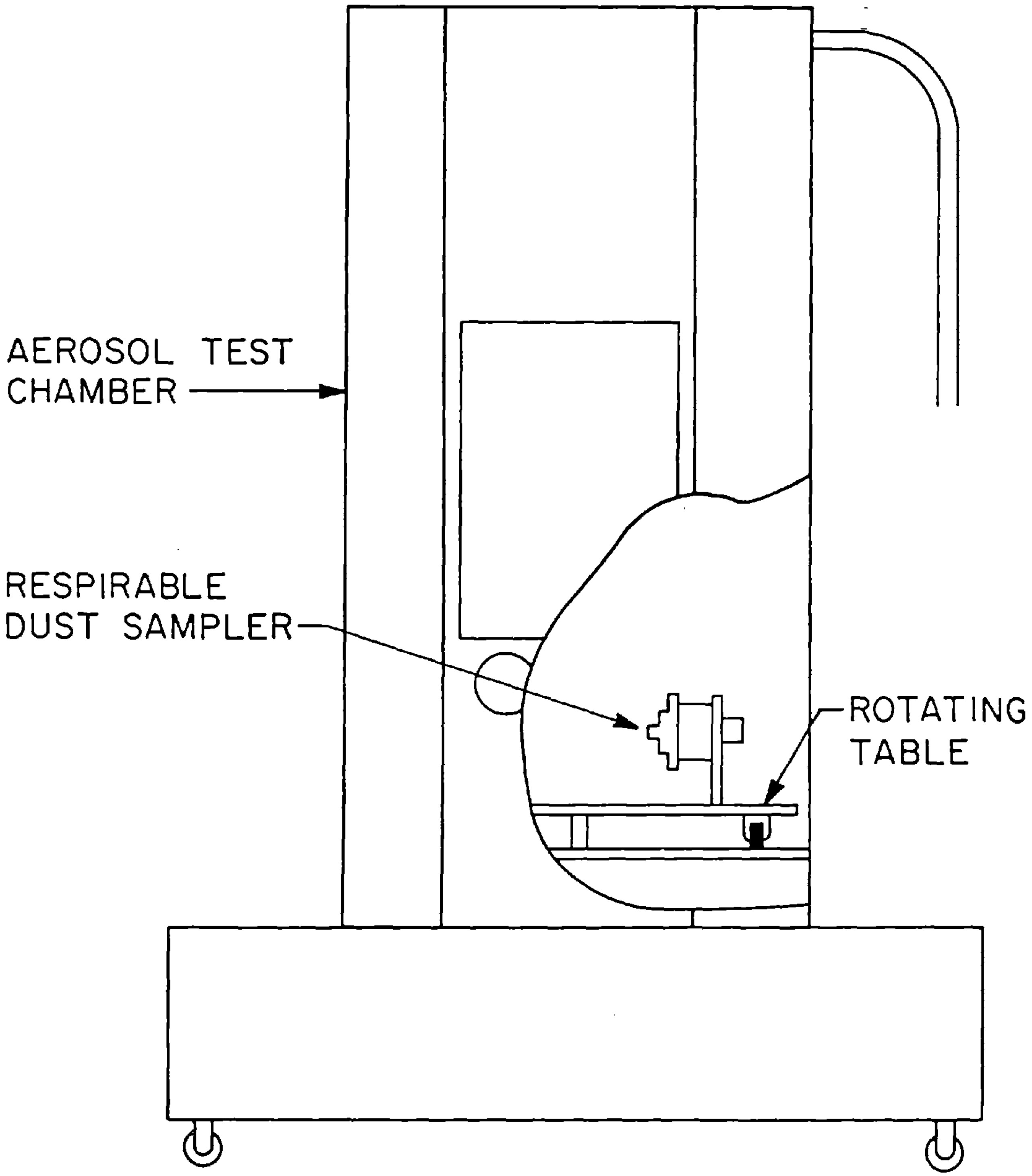

Figure 8. Schematic diagram of the respirable sampler in the aerosol test chamber.

could then create convective currents within the chamber. The periodic movement of the impaction plate, however, will be nearly as effective in spreading out the deposit on the impaction plate as moving it continuously.

The sampling flow rate for this device is dictated by the concentration of the dust within the chamber and the length of time the test is being run. The sampler is designed so the nozzle plate can be easily changed from one nozzle plate to another since different nozzle plates are required for different flow rates. For the sampler described here, the flow rate has been chosen to be 28 l/min (1 CFM), which is impactor F in Table 1.

In use, the sampler is placed into the chamber as shown in Figure 8. For an instrument evaluation test the sampler is operated for the duration of the test. In our current programs, the instruments within the chamber are compared to the concentration of respirable dust determined by the sampler. In some cases, the classifiers of the instruments may have penetration characteristics that are different from the ACGIH curve. For these instances, a second sampler will be placed in the chamber with a nozzle plate possessing the correct respirable cutoff characteristic (for example, the BMRC respirable curve).

IMPACTOR CALIBRATIONS

Several respirable impactors in Table 1 were calibrated with monodisperse oleic acid particles with a uranine dye tracer generated by the vibrating orifice monodisperse aerosol generator (Berglund and Liu, 1973). The quantity of particles penetrating through the impactors were determined by fluorometric analysis of the deposited particles on the impaction plates and the after-filters. The experimental results are shown as experimental data points in Figure 9 for impactors B, F, and G and in Figure 10 for impactor D. The efficiency curves represented by the solid lines are those predicted by theory (Marple, 1970). It can be seen from these figures that there is good agreement between the experimental and theoretical curves.

The personal samplers have also been calibrated by Baron (1981) using an aerodynamic particle sizer. In this work the penetration was also found to agree with the ACGIH respirable criteria.

CONCLUSIONS

It can be concluded from this work that respirable impactors can be employed in a variety of devices to obtain the quantity of respirable particles in an aerosol. These devices range from low flow rate personal samplers to large flow rate samplers. Furthermore, the impactors can be designed to approximate either the ACGIH or BMRC respirable curves. Comparisons between experimentally determined efficiency curves and those calculated from theory show good agreement, indicating that the impactors can be designed a priori with assurance that the resulting penetration curve will be a close approximation to that determined theoretically.

Table 1
Impactor Designs With Penetration Characteristics
Which Simulate Respirable Penetration Curves

Impactor	Total Flow Rate (l/min)	Respirable Curve	No. of Nozzle Sizes	Nozzle cut dia. (μm)	Nozzle Dia. (cm)	No. of Nozzles
A	2	ACGIH	2	5.0	0.25	1
				2.5	0.063	16
B	2	ACGIH	3	5.8	0.24	1
				3.5	0.087	8
				2.2	0.033	53
C	2	BMRC	2	6.1	0.28	1
				3.5	0.093	9
D	2	BMRC	3	6.4	0.26	1
				5.0	0.15	3
				2.9	0.048	28
E	28	ACGIH	2	5.0	0.60	1
				2.5	0.16	14
F	28	ACGIH	3	5.8	0.58	1
				3.5	0.21	8
				2.2	0.086	45
G	40	ACGIH	3	5.8	0.65	1
				3.5	0.24	8
				2.2	0.097	45

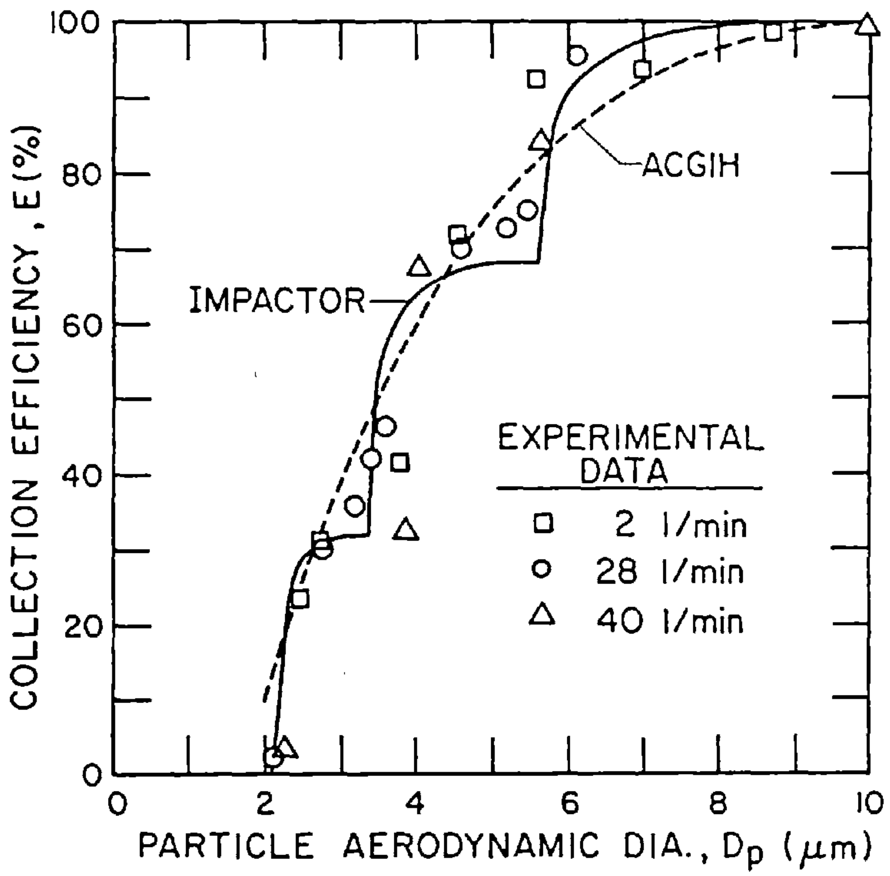

Figure 9. Comparison of experimental data and the theoretical collection efficiency curve for impactors B, F, and G to the ACGIH respirable curve.

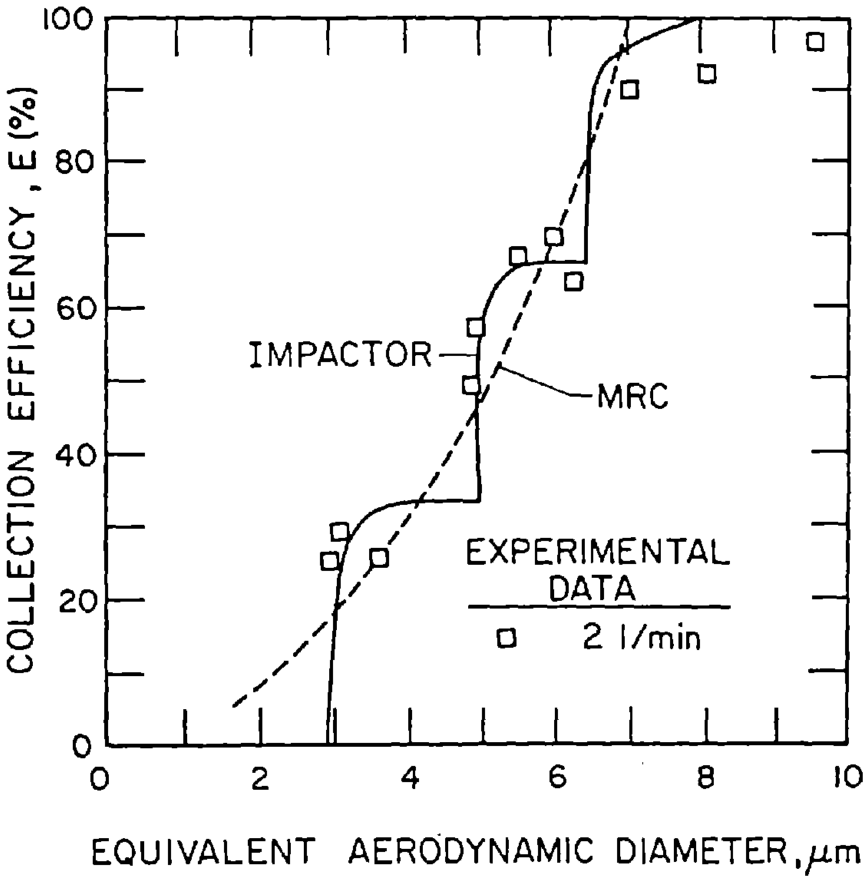

Figure 10. Comparison of experimental data and the theoretical collection efficiency curve for impactor D to the BMRC respirable curve.

REFERENCES

Baron, P. A. (1981) "Sampler Evaluation With an Aerodynamic Particle Sizer", presented at the International Symposium on Aerosols in the Mining and Work Environment, Nov. 1-6, 1981, Minneapolis, Minnesota.

Berglund, R. N. and B. Y. H. Liu, (1973) "Generation of Monodisperse Aerosol Standards", Environ. Sci. Technol. 7:147-153.

Lippmann, M., (1976) "Size-Selective Sampling for Inhalation Hazard Evaluations", in Fine Particles: Aerosol Generation, Measurement, Sampling, and Analysis (B. Y. H. Liu, ed.), pp. 287-310, Academic Press, New York.

Marple, V. A., (1970) "A Fundamental Study of Inertial Impactors", Ph.D. Thesis, Particle Technology Laboratory, Mechanical Engineering Department, University of Minneapolis, Minneapolis, MN.

Marple, V. A., (1978) "Simulation of Respirable Penetration Characteristics by Inertial Impaction", J. Aerosol Sci. 9:124-134.

Marple, V. A., B. Y. H. Liu and K. L. Rubow, (1978) "A Dust Generator for Laboratory Use", Am. Ind. Hyg. Assoc. J. 39:26-32.

Marple, V. A. and K. L. Rubow, (1978) "A Portable Optical Counter System for Measuring Dust Aerosols," Am. Ind. Hyg. Assoc. J. 39:210-218.

Reischl, G. P. and W. John, (1978) "The Collection Efficiency of Impaction Surfaces: A New Impaction Surface", Staub-Reinhalt.derLuft 38:55.

Tomb, T. F. and H. N. Treaftis, (1975)"A New Two-Stage Respirable Dust Sampler", Am. Ind. Hyg. Assoc. J. 36:1.

APPENDIX B

EFFECT OF ULTRASTOKESIAN DRAG AND PARTICLE INTERCEPTION ON IMPACTION CHARACTERISTICS

by

Daniel J. Rader and Virgil A. Marple
Particle Technology Laboratory
130 Mechanical Engineering Department
University of Minnesota
111 Church Street Southeast
Minneapolis, MN 55455-0111

To be published in:

Aerosol Science and Technology

Abstract

The characteristics of impactors with round or rectangular nozzles have been determined by the numerical solution of the Navier-Stokes equations and of the equation of motion of the particles. The sensitivity of this solution to the system of grid lines was investigated by decreasing the spacing between them; these studies yielded sharper curves and higher $\sqrt{St_{50}}$ for finer grids. The particle trajectory calculation program included an empirical ultraStokesian drag coefficient and a facility for handling particle interception. Studies comparing the results of runs made using the ultraStokesian drag law with those assuming Stokes law indicated that the latter underpredicts the $\sqrt{St_{50}}$ by 5-10%. The influence of particle interception was found to be small except at very low Reynolds numbers, the characteristics for which demonstrated low-efficiency tails. Dimensional analysis of the impactor system required the introduction of a second dimensionless quantity (in addition to the St) to characterize the particle-fluid interaction for a given flow field. This dimensionless number, taken as $1/C\ \rho/\rho_p$, was found to influence results only at the high and low extremes of the Reynolds number. For moderate values of the Reynolds number, a single curve relating collection efficiency to $\sqrt{St}$ was found to adequately characterize impactor systems.

Introduction

Inertial impactors are devices which classify aerosol particles by their aerodynamic diameter. This is accomplished, as shown in Figure 1, by directing a jet of particle-laden air at an impaction or collection plate. Particles with sufficient inertia will impact on the plate while smaller, lower inertia particles will not impact but remain suspended in the airstream.

The collection efficiency, E, is defined as the fraction of particles of a given size passing through the nozzle which impact on the plate. The determination of the collection efficiency as a function of particle size is essential to the characterization of inertial impactors. Ideally, this relationship, or characteristic, should be a step function for which no particles smaller than the desired "cut-off" size are collected but all larger particles are, as shown in Figure 2 (ideal case).

In actual practice, many investigators (e.g. Ranz and Wong, 1952; Mercer and Chow, 1968; Mercer and Stafford, 1969; Anderson, 1966; and Lundgren, 1967) have found experimentally that the collection efficiency curve is "S" shaped similar to the "actual" case in Figure 2. However, a parametric theoretical study (Marple, 1970), which numerically solved for impactor flow fields and particle trajectories to obtain the particle collection efficiency curves, predicted curves of the type labeled "theoretical" in Figure 2. Although it has been shown (Jaenicke and Blifford, 1974) that "S" shaped experimental curves have become steeper as the quality of test aerosols has increased (i.e. "monodisperse" aerosols with less spread in the particle size) the experimental collection efficiency curves have still retained the "S" shape.

Another difference between theoretical and experimental efficiency curves has been discussed by Fuchs in a review paper on aerosol impactors (Fuchs, 1978).

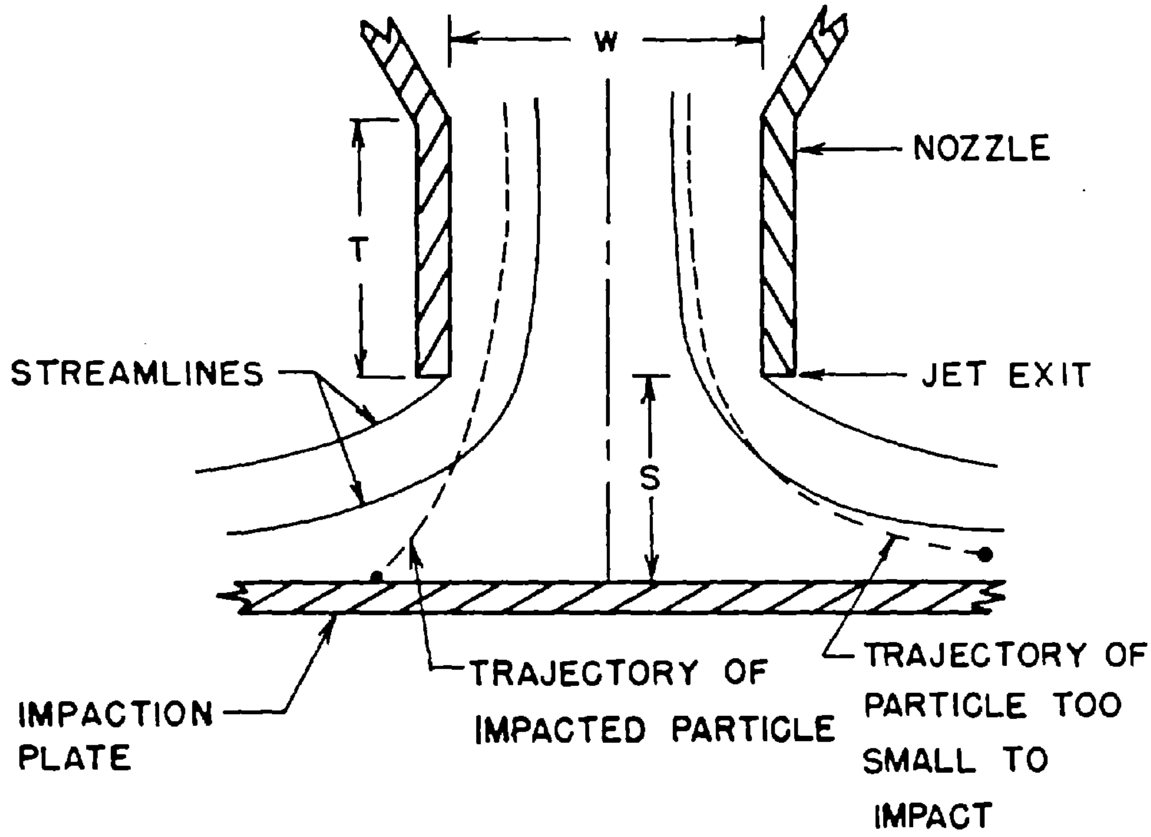

Figure 1. Streamlines and particle trajectories for a typical impactor.

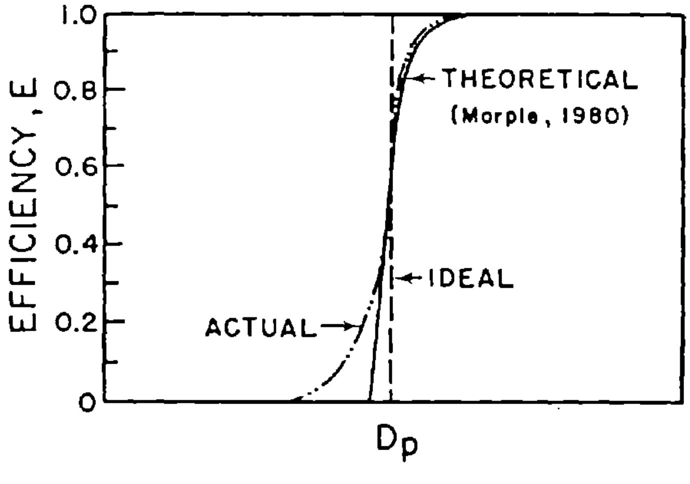

Figure 2. Ideal, theoretical and actual particle collection efficiency curves for inertial impactors.

Fuchs noted that several authors had observed a systematic shift to the right of the characteristic efficiency curve in cascade impactors. Fuchs postulated that this shift may be the result of deviations from the Stokes formula used by the theoretical method, which he suspected as the main source of error in that technique. For particles moving with high velocities relative to the fluid, the use of Stokes formula would underpredict the drag force acting upon a particle. Employing a more accurate drag law results in increasing the force acting to maintain the particles on trajectories coincident with flow streamlines. This increased tendency to follow the flow would be observed as a shift to the right in the collection efficiency curve.

In spite of the differences described above, it should be noted that theoretical and experimental efficiency curves have typically been in agreement. In particular, the theoretical and experimental values of the particle size at 50% collection efficiency, D_{p50}, have agreed quite well (e.g. Jaenicke and Blifford, 1974; Rao, 1975; Willeke and McFeters, 1975; and Marple and Rubow, 1976).

In this paper, a study is described which has refined the original theoretical technique. Improvements in the computational method have been included after consideration of observations such as those discussed above. In particular, the influence of particle interception at the plate, ultraStokesian drag and flow field refinement were investigated.

Previous Work

In the theoretical technique constituting the starting point of this work, the impactor collection efficiency curves were determined theoretically by utilizing numerical analysis techniques (Marple, 1970). The technique included the finite difference solution of the Navier-Stokes equations to determine the flow field (Marple, et al. 1974 a, b) and the subsequent calculation of particle trajectories in the flow field by numerically integrating the particles' equations of motion (Marple and Liu, 1974). This method was applied to the two- dimensional geometries of the round (circular jet) and rectangular (rectangular slit of length L much greater than the nozzle width:L57W) impactors. The study determined the collection efficiency curves for both nozzle configurations as the dimensionless parameters of jet Reynolds number, Re, jet-to-plate distance, S/W, and nozzle throat length, T/W, were varied. Results of that parametric study are reproduced in Figure 3 where the values of Re, S/W and T/W are indicated.

In Figure 3 the particle size on the abscissa is expressed in dimensionless form as the square root of the Stokes number, $\sqrt{St}$, defined as:

$$\sqrt{St} = \sqrt{\frac{\rho_p V_o C D_p^2}{9 \mu W}} \tag{1}$$

where ρ_p is the particle density, V_0 is the average air velocity in the nozzle throat, C is the slip correction, D_p is the particle diameter, μ is the fluid viscosity, and W is the nozzle diameter (round) or nozzle width (rectangular).

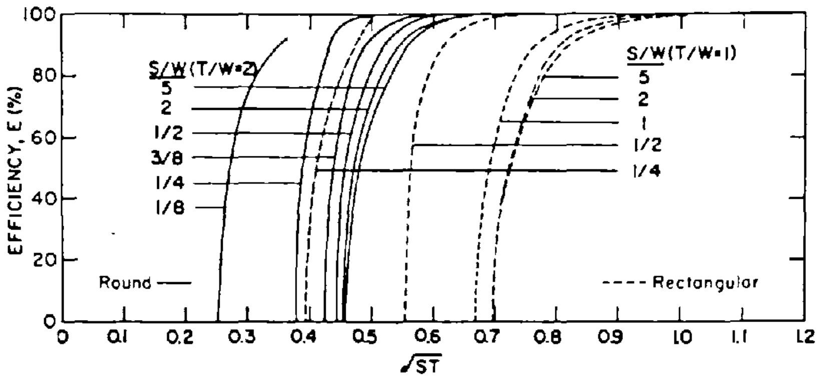

(a) EFFECT OF JET TO PLATE DISTANCE (Re=3,000)

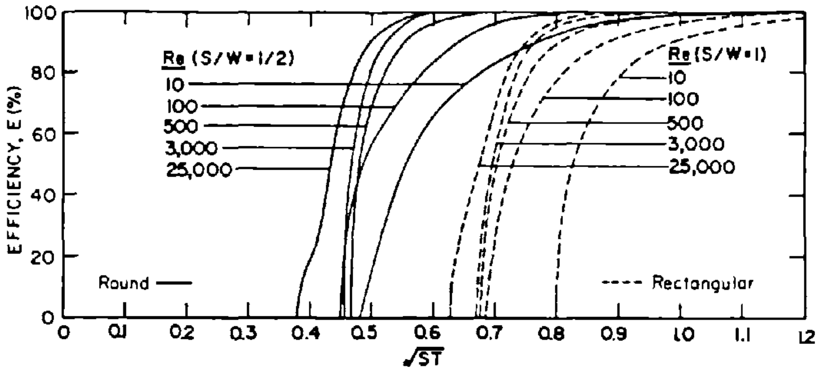

(b) EFFECT OF JET REYNOLDS NUMBER (T/W=1)

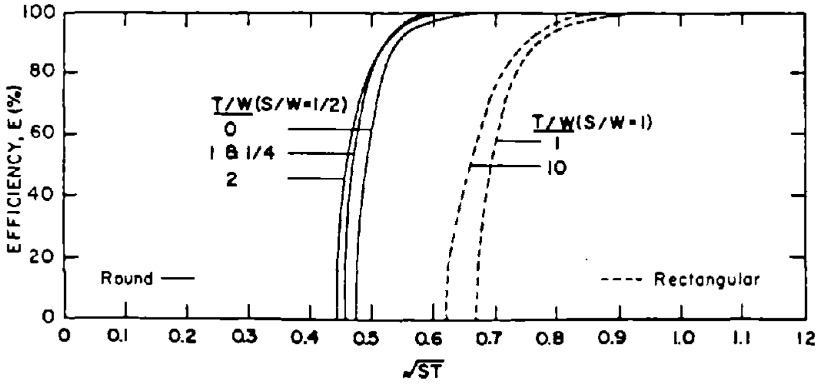

(c) EFFECT OF THROAT LENGTH (Re=3,000)

Figure 3. Original impactor efficiency curves for rectangular and round impactors showing the effect of jet-to-plate distance S, jet Reynolds number Re, and throat length T as determined by Marple (1970).

The Reynolds number, Re, is expressed as:

$$\mathrm{Re} = \frac{\rho W V_o}{\mu} \quad \text{(round)}$$

and

$$\mathrm{Re} = \frac{\rho 2 W V_o}{\mu} \quad \text{(rectangular)} \tag{2}$$

where ρ is the air density. The symbols W, S and T indicate the jet width or diameter, jet-to-plate distance, and nozzle throat length, respectively, as indicated in Figure 1.

It can be seen from the calculated efficiency curves in Figure 3 that they are fairly ideal for efficiencies less than about 0.80 but are nonideal for larger efficiencies. The reason for the nonideal behavior is that the air and particles move at a lower velocity in the fluid boundary layer near the nozzle wall than in the central portion of the jet. Since the particle velocities are lower in this region, the particles must be larger to be collected, causing the nonideal collection characteristics in the upper portion of the curves. A more detailed discussion of this phenomenon has been presented elsewhere (Marple and Liu, 1975).

Comparisons of the theoretical efficiency curves in Figure 3 to experimentally determined efficiency curves have indicated good agreement in most cases, if the nozzle configuration is similar to that shown in Figure 1. The most consistent difference has been found in the portion of the curve represented by efficiencies less than about 0.20. In this region the experimental curves extend to small values of $\sqrt{St}$ as shown by the "actual" case in Figure 1, while theoretical curves in Figure 3 tend to show sharp cut-off characteristics in this region. Thus, the actual experimental curve is "S" shaped while the theoretical curves have predicted only the upper portion of the "S" curve.

Revised Theoretical Technique

In the present work the theoretical technique is revised in three areas. First, the grid over which the Navier-Stokes equations are numerically solved is made finer to more accurately describe the flow field. Second, the particle differential equation of motion is improved by employing a more accurate particle drag coefficient. Third, the condition defining when the particle has impacted upon the impaction plate is refined to include interception effects.

GRID

The present method for calculating the fluid flow field requires that the continuous variables of the Navier-Stokes equation be approximated by a discrete set of unknowns, which are then solved for by the numerical technique. The error associated with attempting to describe a continuous system in this way, often called the discretization error, can be a major limitation to the overall accuracy of the numerical solution. By systematically decreasing the grid spacing the magnitude of this error may be estimated. A good numerical method should provide better resolution of the flow field as the grid is refined. It is expected that discretization errors will be greatest in regions where velocity gradients are large, such as in the boundary layers which form near solid surfaces, where the length scales characterizing flow field details are small, and near flow singularities such as at the stagnation point. The determination of any features of the velocity field which are smaller than the local grid spacing is not possible. Ravenhall and Forney (1980) have demonstrated the sensitive nature of particle trajectory calculations made near the stagnation point in an ideal fluid, rectangular-slit impactor. To improve previous work, their method matched an analytical expression for the flow field near the stagnation point with calculations performed over the remainder of the domain. In the present case, a single calculation scheme is applied throughout the interior of the impactor, and the accuracy of the solution near the stagnation point improved through grid refinement.

The limitation for grid refinement is a practical one. As the number of grid lines increases, the number of calculations which must be performed also increases. Thus, the level of grid refinement is chosen by balancing increased computer costs and improved flow field resolution. In the previous work, such considerations resulted in the use of a 25 x 42 grid for a rectangular impactor of T/W = 1 and S/W = 1 (Marple, 1970). Since computer time has become less expensive, the flow field resolution in the present study is improved by increasing the number of grid lines. Flow field and collection efficiency curves resulting from grid spacings twice as fine (four times as many node points) and four times as fine (sixteen times as many node points) as in the previous work are investigated. The effect of grid refinement on the accuracy of the flow field is implied from subsequent calculation of collection efficiency curves. Thus, the relative improvement between grids is actually evaluated by indirect methods.

DRAG COEFFICIENT

In the previous work, the motion of the particles was assumed to obey Stokes drag law. The use of this assumption required that the particles be moving through a still fluid at a constant velocity and at a low local particle Reynolds number(1) (Re_p <<1).

For the case of particles undergoing accelerations in a non-uniform flow field, such as in an impactor, the equation of motion should include additional terms which modify the resistance of the fluid to these inertial particles (Basset, 1910; Landau and Lifshitz, 1959, p. 97; Fuchs, 1964, p. 75). Fuchs (1964, p. 77) has suggested that, for aerosol systems in which the local particle Reynolds number does not exceed a few hundred and $\rho_p >> \rho$, these additional resistances may be neglected without appreciable error. This is consistent with the more recent work of Sartor and Abbott (1975), who found experimentally that the motion of small water droplets ($Re_p \leq 5$) accelerating from rest agreed well with analytic calculations which assumed steady-state drag coefficients. Thus, in this paper, as in the previous work, the additional drag due to particle and fluid accelerations is neglected, and the resistance at any location will be calculated using the steady-state drag law with the local instantaneous relative velocity.

---

(1) Both the local particle Reynolds number based on the relative velocity between the fluid and the particle, Re_p, and the particle Reynolds number based on the average velocity at the throat, $Re_{p,\,V_0}$, are used in this paper. The former varies with particle location and the latter is a constant, characteristic of the impactor. These are defined in Eqs. (6) and (7).

The assumption that the particles are moving with a low enough local particle Reynolds number ($Re_p \ll 1$) such that their drag can be described by Stokes law at all points in the impactor, however, was felt to be inappropriate (Fuchs, 1978). In practice, the criteria $Re_p \ll 1$ is satisfied for $Re_p \leq 0.1$. Previous trajectory calculations suggested that, under certain impactor operating conditions, the local particle Reynolds number might be as high as ten in regions where velocity gradients are steep. The application of Stokes law would be in error in such regions, and a correct calculation of particle trajectories would require the determination of ultraStokesian fluid resistance for $Re_p \geq 0.1$. This is accomplished by including an empirical drag coefficient, C_D, in the particle equations of motion. Friedlander (1977, p. 106) gives the following set of dimensionless, differential equations for particle motion in two dimensions:

$$\frac{St}{2}\frac{d^2x}{dt^2} = \frac{C_D Re_p}{24}\left(V_x - \frac{dx}{dt}\right) \tag{3}$$

$$\frac{St}{2}\frac{d^2y}{dt^2} = \frac{C_D Re_p}{24}\left(V_y - \frac{dy}{dt}\right) \tag{4}$$

where:

$$St = \frac{\rho_p C V_o D_p^2}{9 \mu W} \tag{5}$$

$$Re_p = Re_{p,Vo}\left[\left(V_x - \frac{dx}{dt}\right)^2 + \left(V_y - \frac{dy}{dt}\right)^2\right]^{1/2} \tag{6}$$

$$Re_{p,Vo} = \frac{\rho D_p V_o}{\mu} \tag{7}$$

$$C_D = C_D(Re_p). \tag{8}$$

The drag coefficient, C_D, can be shown by dimensional analysis to be only a function of particle shape and the local particle Reynolds number. Steady-state drag coefficients can be obtained from C_D vs Re_p data reported in the literature. Note that Stokes law corresponds to the special case for which $C_D = 24/Re_p$. For the present work, a correlation of C_D vs Re_p for spherical particles proposed by Sartor and Abbott (1975) is used for $Re_p \leq 5$ and one proposed by Serafini (Friedlander, 1977, p.105) for $Re_p \geq 5$.

$$\begin{aligned} C_D &= \frac{24}{Re_p}(1 + 0.0916\, Re_p) && Re_p < 5 \\ &= \frac{24}{Re_p}(1 + 0.158\, Re_p^{2/3}) && 5 < Re_p < 1000. \end{aligned} \tag{9}$$

CONDITIONS AT IMPACTION PLATE

In the theoretical procedure used to determine the efficiency curves presented in Figure 3, a particle for which a trajectory was being calculated was assumed to be a point mass. That is, a particle of a specific Stokes number was considered to have impacted on the impaction plate if the trajectory of the center intersected the plate surface as shown in Figure 4a. In practice, the original method did not calculate the particle trajectories all the way to the impaction plate but terminated the calculation at the last grid line above the plate and used an analytical criteria for determining whether the particle would impact (Marple and Liu, 1974).

A more accurate technique would consider the physical size of the particle and assume the particle has impacted if its center comes to within an interception distance of one particle radius of the impaction plate (Marple and Chien, 1980; Rudin, 1981) as shown in Figure 4b. This approach would require that the trajectory calculation be continued to the time of impaction. Limited tests during the previous theoretical work indicated that the same results were obtained for both techniques (Marple, 1970). However, it has been found by Rudin (1981) and in the present work that the results of the two techniques may differ under certain conditions. Thus, in the present work, the interception distance technique is employed.

Dimensionless Parameters of Revised Technique

A solution of the non-dimensional form of the Navier-Stokes equations for the impactor system under consideration is characterized by the fluid Reynolds number and quantities required to describe the specific geometry. Once a flow field has been calculated, the particular form of the particle equation of motion will specify the number of additional dimensionless parameters required to characterize the particle-fluid interaction. In the previous work (Marple, 1970), for which Stokes drag law and point-mass particles were assumed, it was found that only one additional dimensionless parameter, taken as the Stokes number, was needed to fully describe the system. Thus, for a given solution of the flow field (a particular choice of Re, S/W and T/W) a plot of impaction efficiency versus Stokes number yields a single efficiency curve which applies for all similar combinations of physical variables. Recent work by Israel and Rosner (1983) has demonstrated that the use of a generalized Stokes number may permit correlation of these results with those obtained in ultraStokesian and compressible flow regimes. Although of practical importance the use of the generalized Stokes number is not exact, and will not be used here.

In the present work, the use of finite-sized particles and the drag law included in Eqs. (3) and (4) requires additional consideration. For example, it is possible for two particles with the same St value to have different diameters. Thus, their interception by the plate is not identical and different efficiency curves result. In this case, an additional dimensionless quantity, the interception parameter, (r_p/W), would be required in order to fully describe the system; and a family of efficiency curves would replace Marple's original one (which corresponds to $r_p/W = 0$).

The use of an ultraStokesian drag law, as in Eqs. (3) and (4), introduces yet another dimensionless quantity: the particle Reynolds number $Re_{p,Vo}$. As can be seen, integration of Eqs. (3) and (4) requires that both St and $Re_{p,Vo}$ values

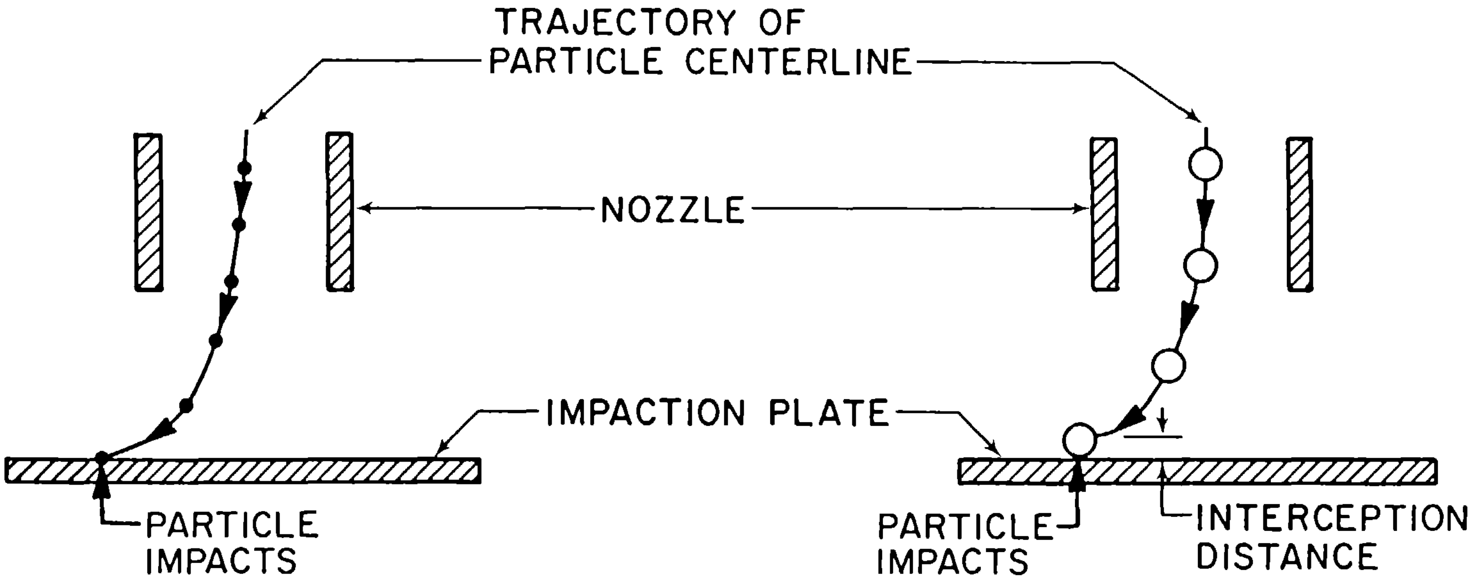

(a) Point Mass Method

(b) Interception Method

Figure 4. Criteria for determining particle impaction.

be specified. The particle Reynolds number, however, is not independent of the interception parameter, the two being related as follows:

$$Re_{p,Vo} = 2\ Re\ \frac{r_p}{W} \quad \text{(round)}$$
$$Re_{p,Vo} = Re\ \frac{r_p}{W} \quad \text{(rectangular).} \qquad (10)$$

Dimensionless analysis confirms that, under the present assumptions and for a particular velocity field, only two dimensionless quantities are necessary to parameterize the impactor system. As before, one of these quantities will be taken as the Stokes number. The choice for the second parameter (either r_p/W or $Re_{p,Vo}$) is not as clear, since they both may be viewed as dimensionless particle diameters (the former by definition, the latter as seen in Eq. (10)) and the use of either might confuse the common interpretation of the $\sqrt{St}$ as the appropriate dimensionless diameter for inertial systems. An alternate dimensionless grouping is suggested by combining St and Re in such a way as to arrive at the following expression for the interception parameter:

$$\frac{r_p}{W} = \sqrt{\frac{9}{4}\,\frac{1}{C}\,\frac{\rho}{\rho_p}\,\frac{St}{Re}} \quad \text{(round)}$$

and

$$\frac{r_p}{W} = \sqrt{\frac{9}{2}\,\frac{1}{C}\,\frac{\rho}{\rho_p}\,\frac{St}{Re}} \quad \text{(rectangular).} \qquad (11)$$

The new dimensionless group $\frac{1}{C}\frac{\rho}{\rho_p}$ is actually the product of two non-dimensional numbers: the inverse of the slip correction factor and the ratio of the density of air to that of the particle. The selection of $\frac{1}{C}\frac{\rho}{\rho_p}$ as the second dimensionless parameter is made on practical grounds. For most impactor systems, the slip correction factor is close to and generally assumed to be equal to unity, in which case the new parameter simply reduces to a density ratio. As the particle and air densities are frequently taken as constant, it is felt that presenting the results of collection efficiency versus Stokes number at a fixed value of $\frac{1}{C}\frac{\rho}{\rho_p}$ could be of practicle use in typical impactor applications. Thus, St and $\frac{1}{C}\frac{\rho}{\rho_p}$ will be taken as the two dimensionless quantities required to characterize a particle introduced into a given flow field. For calculation purposes, the interception parameter and particle Reynolds number may be obtained through Eqs. (11) and (10), respectively.

Results

Several changes have been made to the theoretical technique in calculating the efficiency curves of impactors. Although the ultimate goal is to obtain a better set of theoretical efficiency curves, it is also of interest to investigate how these various changes influence the theoretically determined efficiency curve. Therefore, in this section the effects of the various changes on the efficiency curves will be discussed and then the revised efficiency curves presented.

EFFECT OF GRID SPACING

The magnitude of the flow-field discretization error is investigated by systematically reducing the grid spacing. In Figure 5 the theoretical efficiency curves are shown for both round and rectangular impactors at Reynolds numbers of 500 and 3000 for single-, double- and quadruple-fine grid spacings. As the resolution of the flow field is improved (by using a finer grid), the "S" shape of the efficiency curve for the single-fine grid becomes less pronounced. Thus, the effect of grid refinement is to sharpen the efficiency curve, generally resulting in an increase in the theoretically predicted value for $\sqrt{St_{50}}$ (the square root of the Stokes number at 50% collection efficiency). These results indicate that the courser-grid solutions over-predict the influence of the boundary layers and the stagnation point so that the theoretical efficiency curves predicted by finer grids better approximate the "ideal" curve of Figure 2. This is consistent with the results of Ravenhall and Forney (1980), who obtained sharper efficiency curves by improving the quality of their flow-field solution in the vicinity of the stagnation point.

The influence of grid refinement is most noticeable at the high and low efficiency extremes of the characteristic curves. The upper range of the curves represent particles whose trajectories originate near the nozzle wall and are influenced by the developing boundary layer. As the resolution of the flow in this region improves through grid refinement, the curve steepens, an indication that the coarser solution overpredicts the extent of the boundary layer. At low efficiencies, particle trajectories originate near the centerline, pass near the stagnation point and are entrained in the boundary layer which forms along the impaction plate. As grid refinement improves the quality of the solution in these critical regions, the efficiency curves again become sharper. The effect of grid refinement becomes more pronounced at higher Reynolds numbers, as can be seen by comparing Figures 5a and 5b. At high Reynolds numbers, boundary layers become quite thin, and discretization effors would be expected to increase.

For both round and rectangular impactors, the largest shift in the efficiency curves is between the single- and double-grid results, while the double- and quadruple-grid curves are in fairly good agreement. In consideration of the additional computational costs incurred by each grid refinement (approximately a factor of four), the double grid was selected as the best compromise between cost and accuracy for the present work. For Reynolds number less than 3000, typical discretization errors of 5% or less would then be expected. Unless otherwise stated, the work presented in this paper was performed with the double-fine grid spacing.

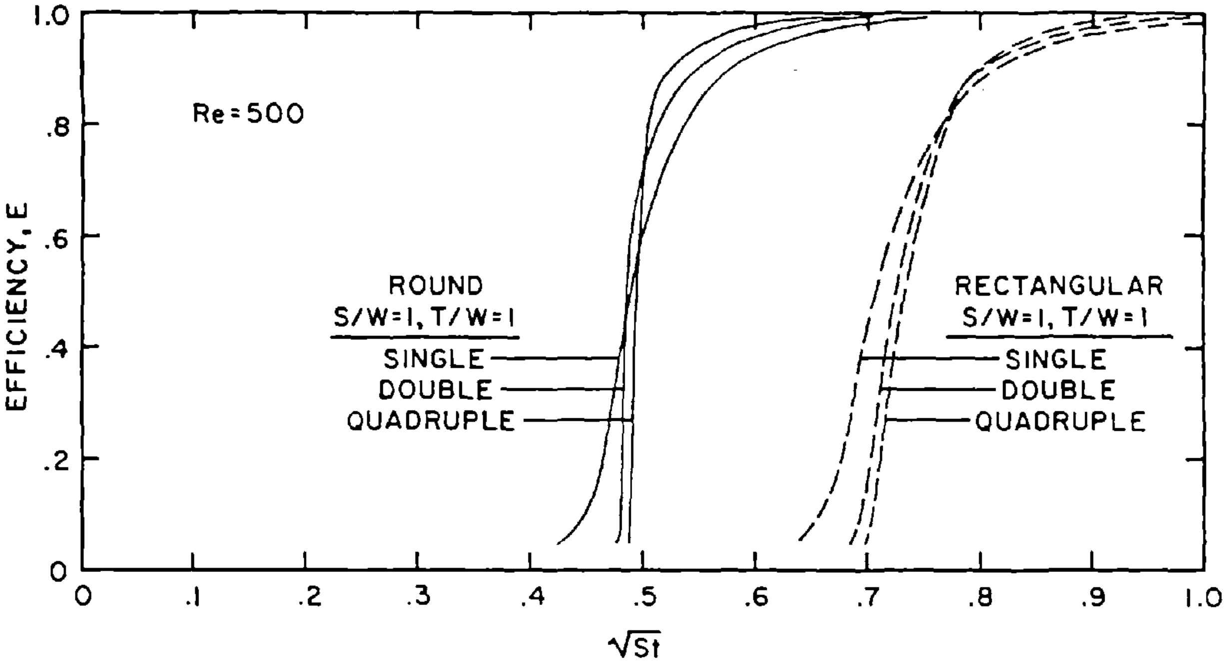

(a) Re = 500

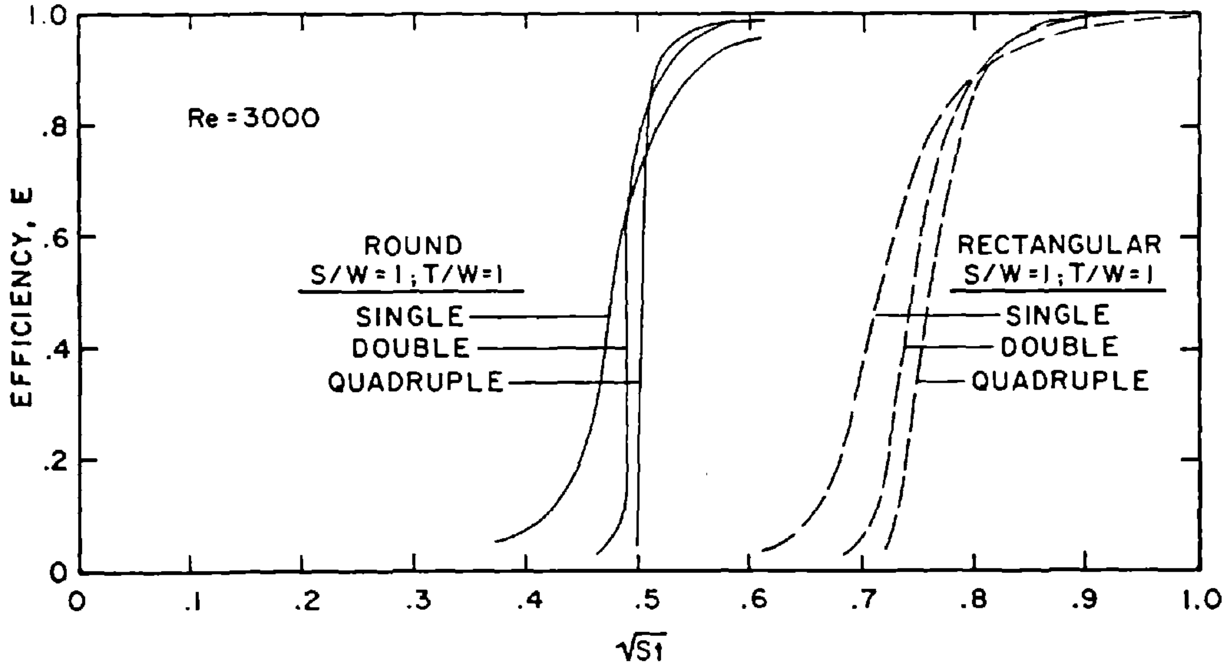

(b) Re=3000

Figure 5. Effect of grid spacing on impactor efficiency curves.

EFFECT OF INTERCEPTION DISTANCE AND ULTRASTOKESIAN DRAG

In the original work, efficiency curves were normally calculated for a particular impactor operating at a specific Reynolds number, with the efficiency presented as a function of the Stokes number. Thus, for a given impactor geometry, the Reynolds number and the Stokes number would uniquely specify a flow condition and collection efficiency for that impactor. As discussed earlier, however, the inclusion of either ultraStokesian drag or interception effects requires that an additional dimensionless parameter be introduced to completely characterize the system. For reasons described in previous sections, this additional parameter was chosen as $\frac{1}{C}\frac{\rho}{\rho_p}$. To demonstrate the effect of this parameter in practical terms, it has been assumed that, 1) the particles are large enough so that C = 1, and 2) the fluid is air at standard conditions. Thus, the only remaining variable in this new dimensionless group is the particle density.

The effect of particle density on the efficiency curves is shown in Figure 6 for round and rectangular impactors at particle densities of 0.5, 1.0 and 10 g/cc. These values for particle density span the range commonly encountered in aerosol work. The efficiency curves of Figure 6 include both the particle interception and the ultraStokesian drag refinements previously described. To help visualize the individual effects of these two refinements, Reynolds numbers were chosen from limits in which the variation of the characteristic with particle density is primarily due to only one of the two.

For a very low Reynolds number (Re = 10), the efficiency curves of Figure 6a shift to the left as particle density decreases. This is primarily due to the effect of interception, since deviations from Stokes drag are small at low nozzle Reynolds numbers. Particles with larger interception distances are more easily collected, and, as shown in Eq. (11), the interception distance increases with decreasing particle density when St and Re are held constant. Thus, the shift to the left of the efficiency curve for decreasing particle densities is actually due to increased collection efficiencies for given values of $\sqrt{St}$. The low-efficiency end of the curves exhibit the greatest sensitivity to variation in the density parameter and demonstrate the characteristic S-shape.

The effect of using ultraStokesian drag coefficients is most easily seen at high nozzle Reynolds numbers for which the interception distance becomes small (Eq. (11)). For example, in Figure 6b at Re = 3,000, the shifts in the efficiency curves at the higher collection efficiencies are due to ultraStokesian effects. Unlike the effect of interception, the efficiency curves shift to higher St values (to the right) for decreasing particle densities. As particle density decreases at constant Re and St, Eqs. (10) and (11) indicate that Re_{p,V_0} increases. A low density particle experiences a greater drag force (Eq. 9) than a particle of the same Stokes number but higher density (lower Re_p,V_0) would. Thus, low density particles are less efficiently collected, resulting in a shift of the collection efficiency curve to the right.

The two sets of curves presented in Figure 6 represent relative extremes in the range of Reynolds number values used in impactors. In the intermediate range of practical concern, $100 \leq Re \leq 1500$, the effects of interception and

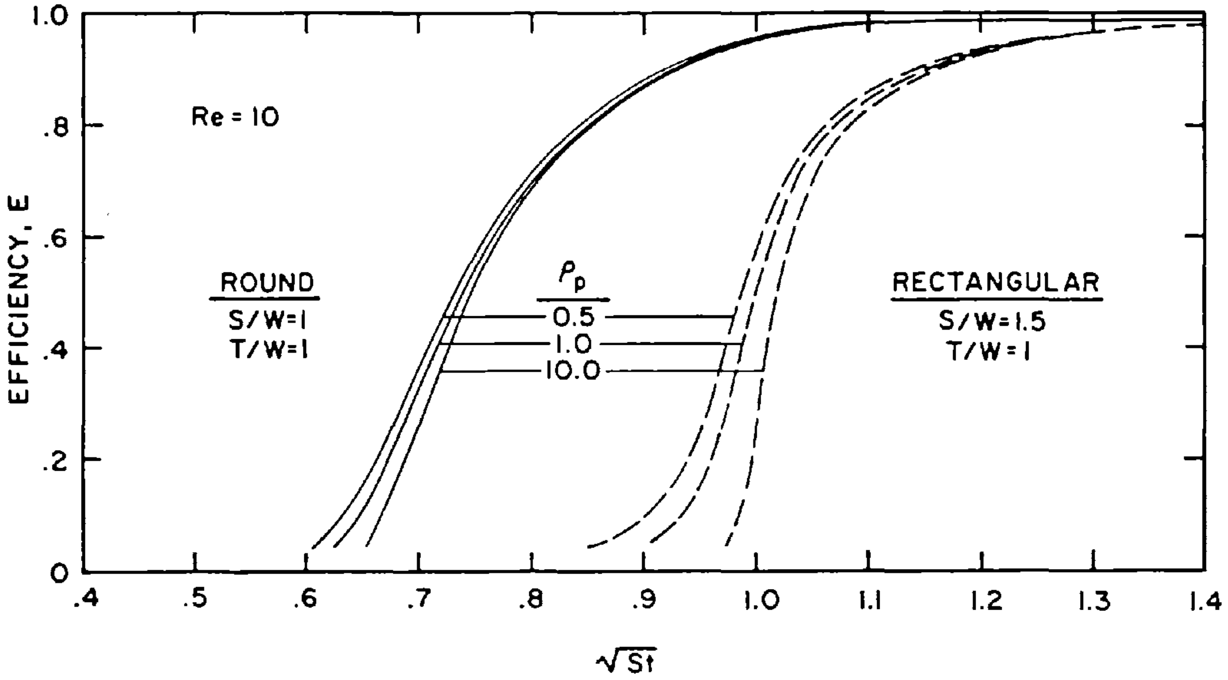

(a) Re = 10

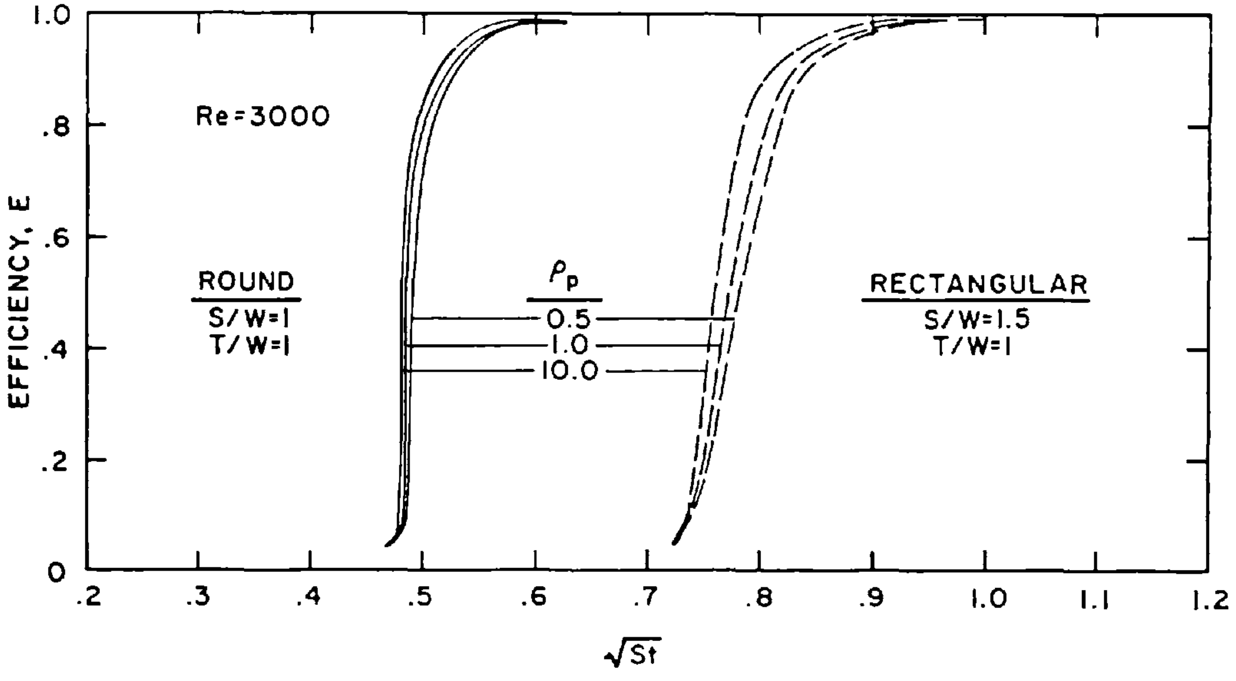

(b) Re = 3000

Figure 6. Effect of particle density on impactor efficiency curves.

ultraStokesian drag essentially cancel out, so that the efficiency curve for a particle density of one may be used with good accuracy for other densities. Thus, the modeling of impactor systems within these limits again reduces to the one-parameter result of Marple.

Finally, to further study the effect of using ultraStokesian drag coefficients a special study was made in which two efficiency curves were calculated for round and rectangular impactors at Re = 3,000. One curve was calculated using Stokesian drag for the particles and the other using ultraStokesian drag. The results, shown in Figure 7, indicate about a 5% shift to higher $\sqrt{St}$ values for ultraStokesian drag. The application of Stokes Law underpredicts the drag acting on the particle; thus, the particle will not follow the flow as closely and will be collected more easily than a particle experiencing ultraStokesian drag. Thus the curves which assume Stokes drag will be to the left of the curves which assume ultraStokesian drag. For lower Reynolds numbers, the shift will be less due to the lower values of $Re_{p,Vo}$.

REVISED THEORETICAL EFFICIENCY CURVES

Figure 8 shows the effect of the jet-to-plate distance and Reynolds number on the efficiency curves for round and rectangular impactors using the revised theory. The calculations assumed air at standard conditions, particles of density 1 g/cc with C = 1, and a double-fine grid spacing. These efficiency curves are quite similar to the original theory shown in Figure 3 which they now replace. The same general conclusions still apply to these figures in the design of impactors (i.e. the Reynolds number should be between 500 and 3,000, $S/W \geq 1.0$ for round impactors and $S/W \geq 1.5$ for rectangular impactors.)

COMPARISON OF ORIGINAL AND REVISED EFFICIENCY CURVES

Although the most direct method of comparing the original and revised efficiency curves would be to compare the curves in Figures 3 and 8, there are some differences in the parameters and assumptions which must be considered. For example, S/W = 1/2 in the original curves and 1.0 in the revised curves for the round-impactor study in which Re is varied as a parameter. In addition, present day lower computer time costs have allowed the revised work to be done with finer grids.

To provide for a direct comparison of the two techniques, runs were made for the condition S/W=1, T/W = 1 and Re = 3000. The results, shown in Figure 9, compare the curves for two grid spacings of the revised technique to a curve for the original technique.

Since the single-grid spacing used for the current method is identical to that used by Marple, any difference between these curves is due only to refinements included in the trajectory calculations. First, the use of an ultraStokesian drag law should shift the new efficiency curves to the right of the original curves which assumed Stokes law. This is seen for both round and rectangular impactors for efficiencies greater than about 25%. The shift, however, is less than would be predicted by the study shown in Figure 7. In fact, the new curves lay to the left of the original ones for low efficiencies.

This shift to lower Stokes numbers is due to the second refinement in the trajectory-calculation method: the inclusion of particle interception. This

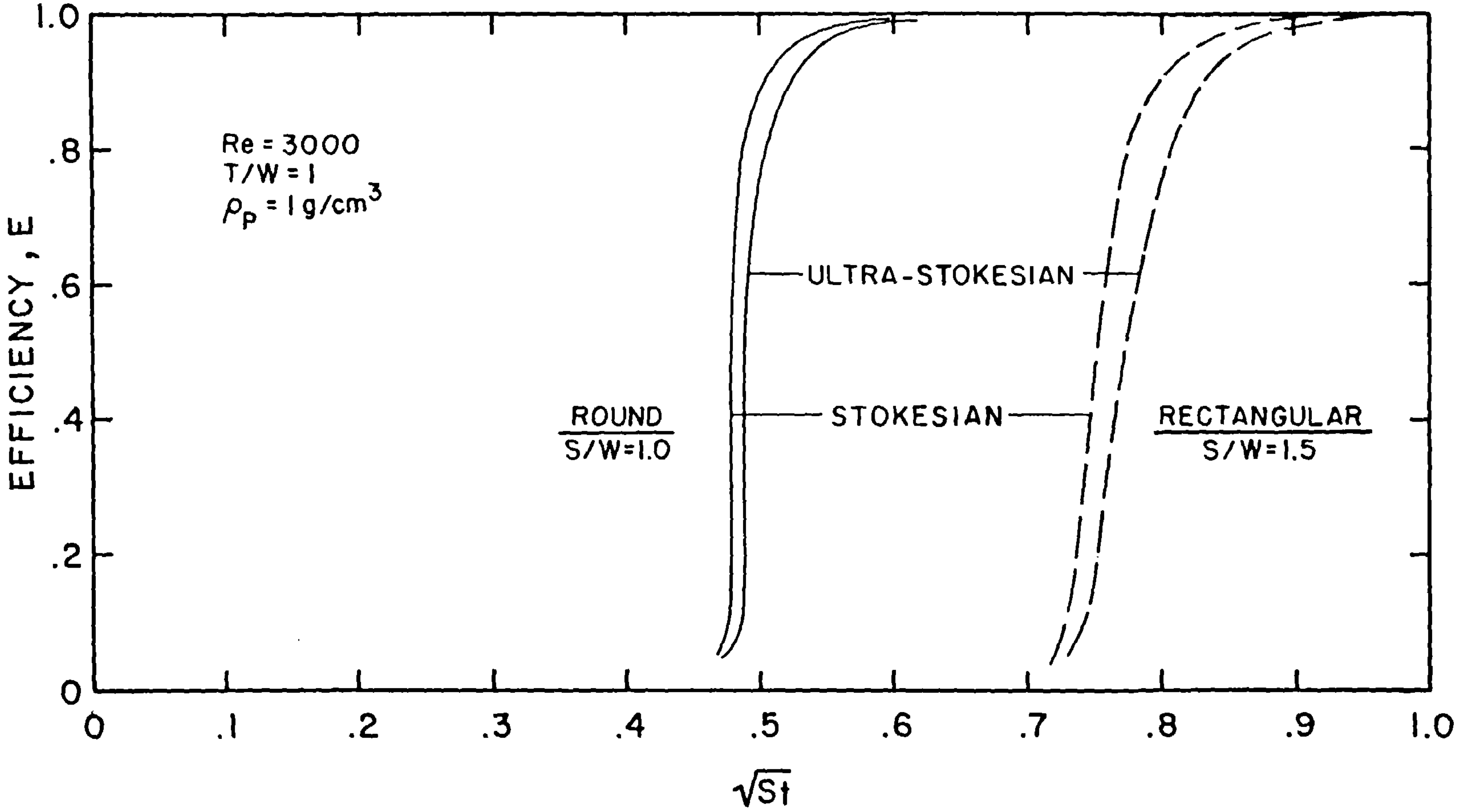

Figure 7. Effect of particle drag law on impactor efficiency curves.

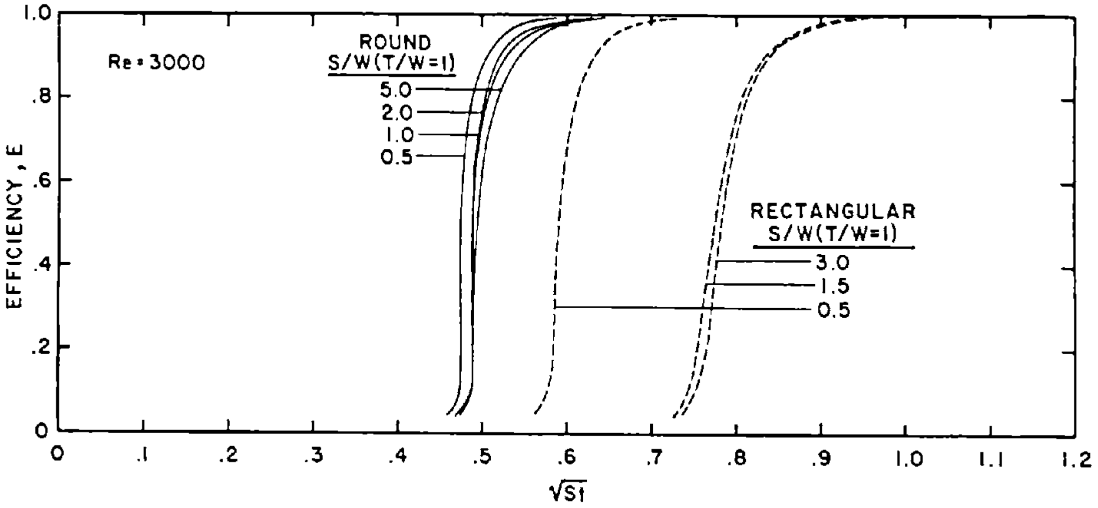

(a) EFFECT OF JET TO PLATE DISTANCE (Re = 3000)

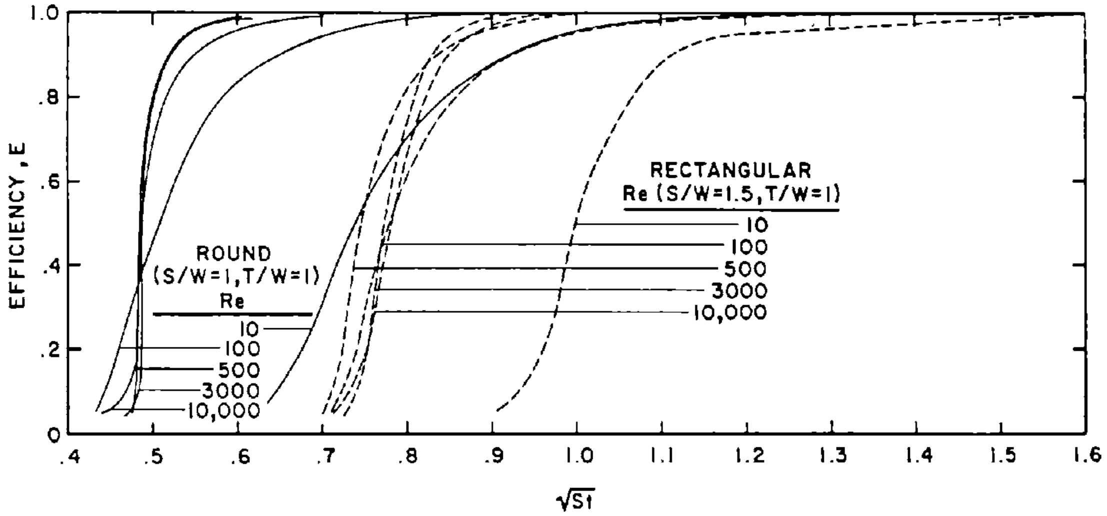

(b) EFFECT OF JET REYNOLDS NUMBER

Figure 8. Revised impactor efficiency curves for rectangular and round impactors showing effects of jet-to-plate distance, S, and jet Reynolds number, Re.

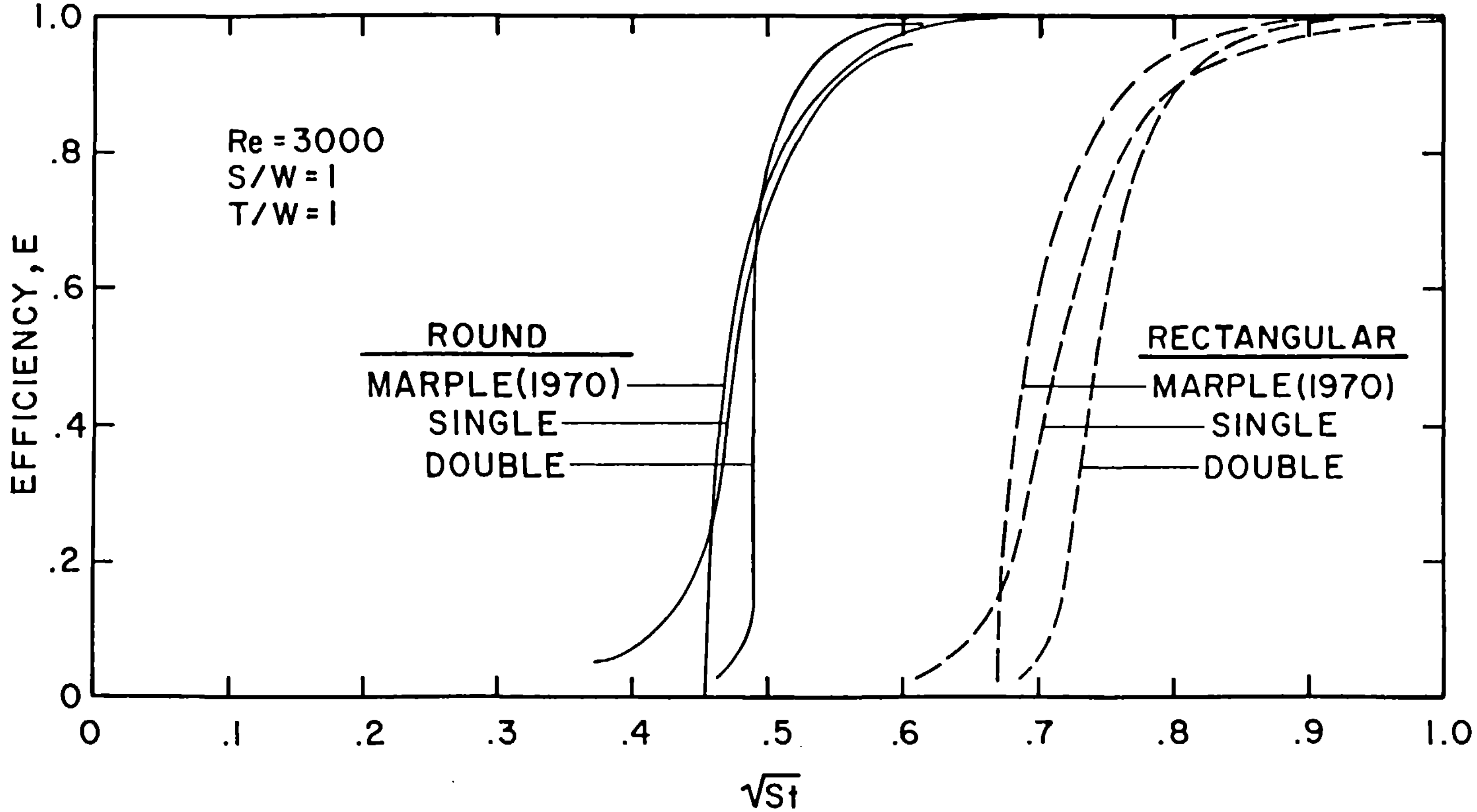

Figure 9. Comparison of impactor efficiency curves calculated from original and revised theoretical techniques.

improvement required that the analytic criteria for determining if impaction occurs be discarded, and that the integration process be followed through until the particle's center comes within an interception of the plate. As discussed earlier, the effect of including the finite size of the particle should be to shift the efficiency curves to the left, while that of continuing the integration to the plate is not known a priori. The combined effect, however, is to enhance the low-efficiency tail of the characteristics, so that the revised single-grid curves show a characteristic S-shape not found in the original work.

With grid refinement, however, the new theory predicts sharper cuts which are shifted to higher $\sqrt{St}$ values. Thus, a comparison of a revised double-grid curve with Marple's original work shows a 5-10% increase in $\sqrt{St_{50}}$ for this choice of operating conditions and Reynolds number. Although the low efficiency tail becomes less prominent with finer grid spacings, it does not entirely disappear, particularly for the rectangular geometry.

The difference between the curves in Figures 3 and 8, for other S/W values, can probably best be seen by plotting $\sqrt{St_{50}}$ vs S/W for both techniques (Figure 10). This shows that the revised technique predicts $\sqrt{St_{50}}$ values about 5-10% higher than the original technique.

Conclusions

The revision of impactor theory, including grid refinement, ultraStokesian equations for the drag of the particles and interception of the particles at the impaction plate has resulted in shifts of 5-10% in efficiency curves for inertial impactors. This revised set of curves is shown in Figure 8. The most significant change in efficiency curves was found from grid refinement which is now practical with higher speed computers. The influence of increasing the number of node points has been to predict an efficiency curve which is shifted to the right of that predicted with the original theory and grid spacing. The new theory predicts slightly sharper cuts for round impactors while producing rectangular impactor efficiency curves which demonstrate a more pronounced S-shape than the original theory.

The inclusion of particle interception at the plate results in the appearance of a small tail at the low-efficiency range of the characteristic curves. This tail becomes less pronounced with grid spacing refinement and is not significant enough to explain the difference between experiment and theory. For very large particles, however, the effect of particle interception may become more pronounced.

The use of ultraStokesian drag coefficients shifts the collection efficiency curves to the right. This shift is generally small, 5 to 10%, for typical impactor systems. Noticeable deviations due to ultraStokesian effects will be observed for higher Reynolds numbers at the higher efficiencies.

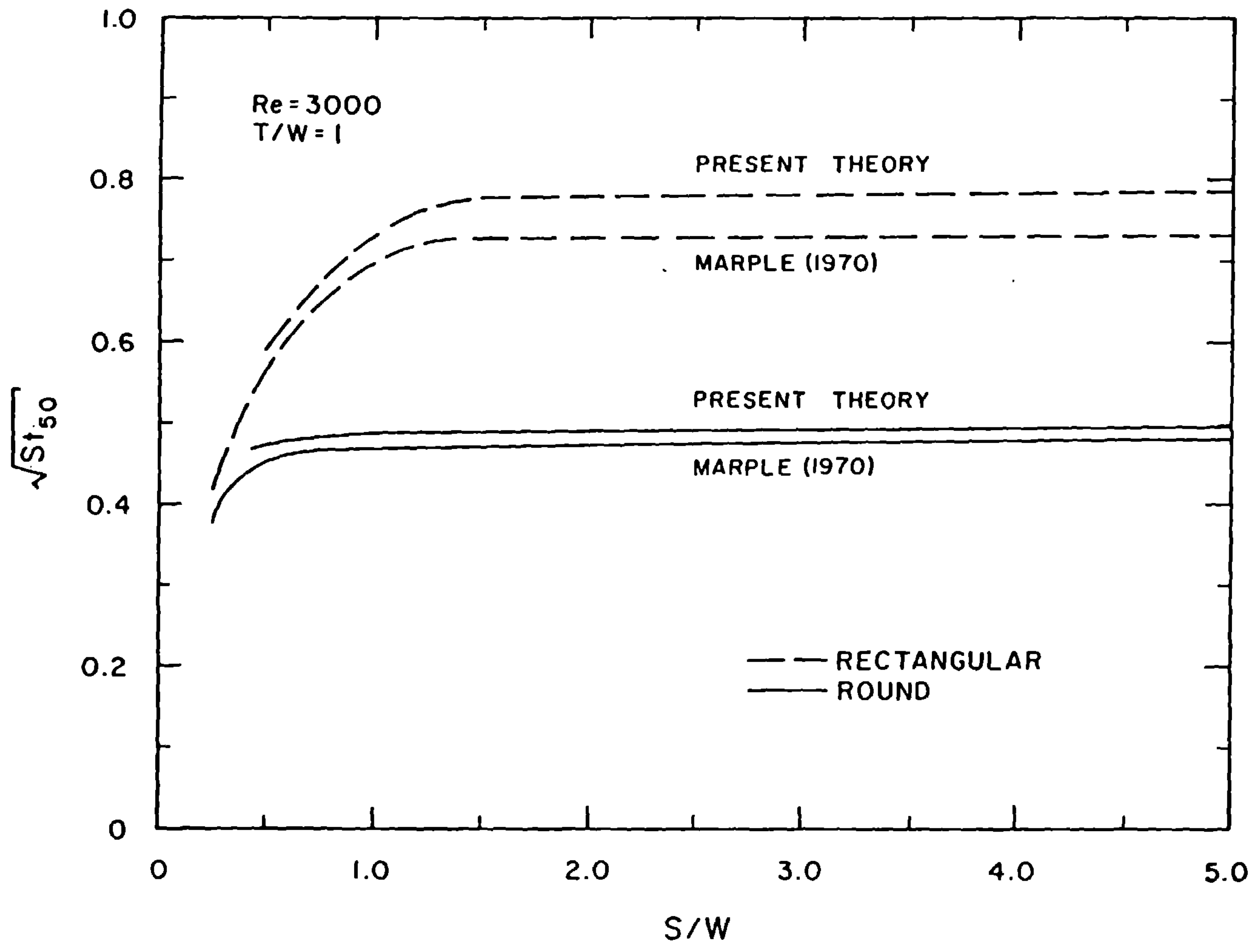

Figure 10. Comparison of $\sqrt{St_{50}}$ as a function of S/W for original and revised theoretical techniques.

Nomenclature

C = slip correction

C_D = drag coefficient

D_p = particle diameter (cm)

D_{p50} = value of D_p at 50% efficiency (cm)

E = collection efficiency

Re = jet Reynolds number, $\rho W V_0/\mu$ (round), $\rho 2 W V_0/\mu$ (rectangular)

Re_p = local particle Reynolds number

Re_{p,V_0} = particle Reynolds number based on average velocity in nozzle throat, $\rho D_p V_0/\mu$

r_p = particle radius (cm)

S = dimensional jet-to-plate distance (cm)

St = Stokes number, $\rho_p V_0 C D_p^2/9\mu W$

St_{50} = value of St at 50% efficiency

T = dimensional nozzle throat length (cm)

t', t = time (s) and dimensionless time, $t' V_0/W$

W = throat diameter (round) or width (rectangular)(cm)

V_0 = average air velocity in the nozzle throat (cm/s)

V_x', V_y' = x and y components of fluid velocity

V_x, V_y = dimensionless components of fluid velocity, V_x'/V_0, V_y'/V_0

x', y' = coordinates measured from centerline and entrance, respectively (cm)

x, y = dimensionless coordinate, x'/W, y'/W

μ = fluid viscosity (g/cm/s)

ρ = air density (g/cm^3)

ρ_p = particle density (g/cm^3)

References

Andersen, A. A. (1966), A Sampler for Respiratory Health Hazard Assessment", J. Amer. Industrial Hygiene Assoc. 27:160.

Bassett, A. B. (1910). Quart. J. Math. 41, p. 369.

Friedlander, S. K. (1977). Smoke, Dust and Haze, Wiley-Interscience, New York.

Fuchs, N. A. (1964). The Mechanics of Aerosols, Pergamon Press, Oxford.

Fuchs, N. A. (1978). "Aerosol Impactors," in Fundamentals of Aerosol Science, D. T. Shaw (ed.), Chapter 1, pp. 1-85.

Israel, R. and D. E. Rosner (1983) "Use of a Generalized Stokes Number to Determine the Aerodynamic Capture Efficiency of Non-Stokesian Particles from a Compressible Flow", Aerosol Science and Techn. 2:45-51.

Jaenicke, R. and I. H. Blifford (1974) "The Influence of Aerosol Characteristics on the Calibration of Impactors", J. Aerosol Sci. 5:457.

Landau, L. D. and Lifshitz, E. M. (1959). Fluid Mechanics, Addison-Wesley, Reading, Mass.

Lundgren, D. A. (1967) "An Aerosol Sampler for Determination of Particle Concentration of Size and Time", J. Air Pollution Control Assoc., 17:225.

Marple, V. A. (1970) "A Fundamental Study of Inertial Impactors", Ph.D. Dissertation, University of Minnesota, Particle Technology Laboratory Publ. No. 144.

Marple, V. A. and B. Y. H. Liu (1974) "Characteristics of Laminar Jet Impactors", Environ. Sci. Technol, 8:648-654.

Marple, V. A. and B. Y. H. Liu (1975) "On Fluid Flow and Aerosol Impaction in Inertial Impactors", J. Colloid and Interface Sci., 53:31-34.

Marple, V. A. and C. M. Chien (1980). "Virtual Impactors: A Theoretical Study," Environ. Sci. Technol. 14:976-985.

Marple, V. A. and K. Rubow (1976) "Aerodynamic Particle Size Calibration of Optical Particle Counters" J. Aerosol Sci., 7:425-433.

Marple, V. A., B. Y. H. Liu and K. T. Whitby (1974a) "On the Flow Fields of Inertial Impactors", ASME J. Fluid Eng. 96:394-403.

Marple, V. A., B. Y. H. Liu and K. T. Whitby (1974b) "Fluid Mechanics of the Laminar Flow Aerosol Impactor", J. Aerosol Sci., 5:1-16.

Mercer, T. T. and H. Y. Chow (1968) "Impaction From Rectangular Jets", J. Colloid and Interface Sci., 27:75.

Mercer, T. T. and R. G. Stafford (1969) "Impaction From Round Jets", Ann. Occup. Hyg., 12:41.

Ranz, W. E. and J. B. Wong (1952) "Impaction of Dust and Smoke Particles", Ind. Eng. Chem., 44:1371.

Rao, A. K. (1975) "An Experimental Study of Inertial Impactors", Ph.D. Dissertation, University of Minnesota, Particle Technology Laboratory, Publ. No. 269.

Ravenahll, D. G. and L. J. Forney (1980) "Aerosol Impactors: Calculation of Optimum Geometrics", J. Phys. E: Sci. Instrum. 13:87-91.

Rudin, E. (1981). "Interception Effects in the Collection Characteristics of Inertial Impactors" M.S. Thesis, University of Minnesota, Particle Technology Laboratory Publication No. 458.

Sartor, J. D. and C. E. Abbott (1975). "Prediction and Measurement of the Accelerated Motion of Water Drops in Air," J. Appl. Meteorol., 14:232-239.

Serafini, J. S. (1954). NACA Report 1159.

Willeke, K. and J. J. McFeters, (1975) "The Influence of Flow Entry and Collecting Surface on the Impaction Efficiency of Inertial Impactors", J. Colloid Interface Sci. 53:121-127.